



Application of X-ray scattering techniques for the analysis of pharmaceutically relevant materials

A thesis presented in fulfilment of the requirements for the
degree of Doctor of Philosophy in the Faculty of Science of
the University of Strathclyde

by

John Mahon

Strathclyde Institute of Pharmacy and Biomedical Sciences

November 2022

Declaration of Author's Rights

This thesis is the result of the author's original research. It has been composed by the author and has not been previously submitted for examination which has led to the award of a degree.

The copyright of this thesis belongs to the author under the terms of the United Kingdom Copyright Acts as qualified by the University of Strathclyde Regulation 3.50. Due acknowledgement must always be made of the use of any material contained in, or derived from, this thesis.

Acknowledgements

Firstly, I would like to thank my supervisors Professor Alastair Florence and Dr John Robertson. Alastair for allowing me the opportunity to undertake my PhD in his research group and for his support and guidance throughout the project. John for his knowledge and input to my research.

Special thanks go to Dr Alan Martin for his constant support and assistance throughout my PhD, particularly all the time spent in the lab at the SAXS system. I would also like to thank Dr Chantal Mustoe for all of the time spent reviewing the multiple versions of this thesis.

I also would like to thank Dr Cheryl Doherty from GSK for her extensive contribution to Chapter 5 through the supply of material and fruitful discussions around the data. Thanks also to Dr Lyke Onyemelukwe for his facilitating the project, and Dr Vijay Srirambhatla for support through data analysis for the chapter.

I would like to thank the CMAC National Facility, in particular, Dr Thomas McGlone and Dr Deborah Bowering for assisting with sample analysis and facilitating instrument and laboratory access.

Thanks are also due to Dr Vitor Magueijo and Dr Hui Mao for supplying materials for Chapter 6 and for considerable input around data analysis.

Finally, I would like to thank my family and friends for their support and encouragement throughout my studies. Particularly Linda without who I'm not sure I would have finished this research.

Abstract

Due to increasing numbers of new chemical entities (NCE) being produced with poor aqueous solubility, there has been an increase in the use of amorphous pharmaceuticals. The research presented within this thesis reports the use of wide angle X-ray scattering (WAXS) as an analysis tool for the characterisation of amorphous solid dispersions (ASDs) to predict the stability of the amorphous form during dissolution. The processing of the ASD was investigated to understand the importance of the processing temperature and the drug loading for paracetamol and affinisol dispersions. Creation of a bespoke sample stage allowed for real-time data of the crystallisation event occurring due to the presence of dissolution media.

Investigations of GSK2838232M samples, using small angle X-ray scattering (SAXS), containing various levels of amorphous content showed that with increased milling time, the intensity of the SAXS profile differed which gave insight into the heterogeneity of the samples. SAXS was found to be sensitive to small changes in amorphous content within the milled samples.

Cellulose-containing fibres and films were analysed using WAXS. This enabled information on the crystallinity and orientation of cellulose nanocrystals (CNC) within the fibres and films to be extracted. The impact of post-processing of fibres was studied regarding CNC orientation, and this work demonstrated a low-cost method of improving the properties of the material.

Table of Contents

Declaration of Author's Rights	i
Acknowledgements	ii
Abstract	iii
Chapter 1: Introduction.....	1
1.1 Thesis Overview.....	2
1.1.1 Background on Solid State Pharmaceutical Ingredients.....	3
1.2 Pharmaceutical Solid Form.....	7
1.2.1 Crystalline Pharmaceuticals.....	8
1.2.2 Amorphous Pharmaceuticals.....	13
1.2.3 Solid Dispersions / Amorphous Solid Dispersion	16
1.3 Dissolution.....	18
1.3.1 Dissolution Theory / History	18
1.3.2 Dissolution of Amorphous Solid Dispersions.....	20
1.3.3 Crystallisation during dissolution.....	21
1.4 Cellulose.....	22
1.4.1 Cellulose Structure	23
1.4.2 Cellulose nanomaterials	25
1.5 Analytical Techniques.....	27
1.5.1 Small Angle X-Ray Scattering.....	27
1.5.1.1 SAXS Pharmaceutical / Amorphous Applications	32
1.5.2 X-Ray Powder Diffraction / Wide Angle X-Ray Scattering.....	33

1.5.3	Thermal Analysis	36
1.5.3.1	Differential Scanning Calorimetry	36
1.5.3.2	Thermogravimetric Analysis.....	37
1.5.4	Spectroscopic Analysis.....	38
1.5.4.1	Fourier Transform Infrared Spectroscopy	38
1.5.4.2	Terahertz Raman Spectroscopy	38
1.6	Manufacturing Techniques	39
1.6.1	Hot Melt Extrusion	39
1.6.2	Ball Milling	40
Chapter 2:	Aims and Objectives.....	42
2.1	Aims	43
2.2	Objectives.....	43
Chapter 3:	Materials and Methods	45
3.1	Materials.....	46
3.2	Methods	47
3.2.1	Manufacturing Methods	47
3.2.1.1	Hot Melt Extrusion	47
3.2.1.2	Ball milling	47
3.2.2	Analytical Techniques.....	48
3.2.2.1	Small Angle X-Ray Scattering (SAXS).....	48
3.2.2.2	Wide Angle X-Ray Scattering (WAXS).....	48
3.2.2.3	X-Ray Powder Diffraction (XRPD)	48

3.2.2.4	Differential Scanning Calorimetry (DSC).....	50
3.2.2.5	Thermogravimetric Analysis (TGA).....	50
3.2.2.6	Fourier Transform InfraRed Spectroscopy (FTIR).....	50
3.2.2.7	Scanning Electron Microscopy (SEM).....	51
3.2.2.8	Terahertz (THz) Raman.....	51
Chapter 4:	Physical Stability of Amorphous Solid Dispersions	52
4.1	Introduction.....	53
4.2	Experimental	55
4.2.1	Hot Melt Extrusion	55
4.2.1.1	X-ray Powder Diffraction.....	56
4.2.1.2	Wide Angle X-ray Scattering.....	56
4.2.1.3	Terahertz Raman.....	57
4.3	Results and Discussion	58
4.3.1	Raw materials and dry extrudate analysis.....	58
4.3.2	Analysis of Formulated Samples	60
4.3.2.1	Reference Terahertz Raman Spectra of Amorphous and Crystalline Paracetamol in the Presence of Affinisol™.....	60
4.3.2.2	Analysis of 10 wt% Paracetamol ASD Formulation	62
4.3.2.1	Analysis of 20 wt% Paracetamol ASD Formulation	66
4.3.2.2	Analysis of 25 wt% Paracetamol ASD Formulation	68
4.3.2.3	Analysis of 27.5 wt% Paracetamol ASD Formulation.....	71
4.4	Summary.....	76

Chapter 5:	Investigation of Crystallinity in an Active Pharmaceutical Ingredient ..	78
5.1	Introduction.....	79
5.2	Experimental	83
5.2.1	Preparation of amorphous GSK2838232M samples	83
5.2.2	Small Angle X-ray Scattering.....	84
5.2.3	X-ray Powder Diffraction.....	85
5.2.4	Fourier Transform Infrared Spectroscopy	86
5.2.5	Differential Scanning Calorimetry	86
5.2.6	Thermogravimetric Analysis.....	86
5.2.7	Scanning Electron Microscopy.....	87
5.3	Results and Discussion	87
5.3.1	Characterisation of GSK2838232M starting material	87
5.3.1.1	X-ray Diffraction Characterisation of Crystalline Material	87
5.3.1.2	DSC Analysis	88
5.3.1.3	Variable Temperature XRPD Analysis for Investigation of Potential Solid-Solid Transition in Starting Material	90
5.3.2	Characterisation of the relative crystallinity of ball-milled samples	93
5.3.2.1	X-ray Powder Diffraction Analysis for Characterisation of Increasing Amorphous Content	93
5.3.2.2	Relative Crystallinity Analysis Using DSC.....	95
5.3.2.3	Thermogravimetric Analysis of Mass Loss.....	98
5.3.2.4	Spectroscopic Structural Analysis using FTIR	99
5.3.2.5	SEM Analysis of Milled Samples	100

5.3.2.6	Characterisation of Amorphous Samples Using SAXS	103
5.4	Summary	111
Chapter 6: Wide Angle X-ray Scattering for the Analysis of Crystallinity and		
Orientation of Biocomposite Fibres and Films of Microfibrillated and Nanofibrillated		
Cellulose Produced from Potato Pulp		
6.1	Introduction.....	115
6.2	Materials and Methods	117
6.2.1	Preparation of Alginate and Cellulose Fibres and Films.....	117
6.2.1.1	Capillary X-Ray Powder Diffraction.....	120
6.2.1.2	Wide Angle X-ray Scattering.....	120
6.3	Results and Discussion	122
6.3.1	Raw materials.....	122
6.4	WAXS Analysis of Cellulose Fibre and Film Samples	123
6.4.1	Pure Alginate Fibres in the Absence of Cellulose	123
6.4.2	Stretched Alginate Fibres	126
6.4.3	Microfibrillated Cellulose Fibres	129
6.4.4	Stretched Microfibrillated Cellulose fibres	132
6.4.5	Nanofibrillated Cellulose Fibres	135
6.5	Alginate and Cellulose Film Samples.....	137
6.5.1	Alginate Film Sample in the Absence of Cellulose	137
6.5.2	Nanofibrillated Cellulose Film	138
6.5.3	Microfibrillated Cellulose Film	140
6.6	Orientation Index and Percent Crystallinity Analysis	141

6.7	Summary	146
Chapter 7:	Conclusions and Future Work.....	148
	References	156

List of Figures

Figure 1.1: Depiction of length scales accessible through X-ray scattering techniques	2
Figure 1.2: Molecular arrangements of organic solids with organised crystal solid forms and disordered amorphous solid ¹	3
Figure 1.3: Biopharmaceutics Classification System (BCS) based on drug solubility and permeability parameters ¹³	5
Figure 1.4: Free energy vs temperature diagram for amorphous and crystalline solids ¹⁹	6
Figure 1.5: Schematic of solids classification of most appropriate pharmaceutical forms ²⁹	8
Figure 1.6: Seven Simple Unit Cells	9
Figure 1.7: Example amorphous (a) vs crystalline (b) XRPD patterns of Sucrose ⁴³	14
Figure 1.8: An example of a free energy - temperature phase diagram. T_m represents the melting temperature above which the liquid is in its stable form, with the crystal phase at the lowest free energy phase below T_m . T_g represents the glass transition temperature ⁵²	15
Figure 1.9: Schematic of Simple Representation of Dissolution Process	18
Figure 1.10: Comparison of amorphous and crystalline indomethacin dissolution profiles ⁶⁵	20
Figure 1.11: Dissolution profile comparison of amorphous and crystalline drug ⁶⁷	21
Figure 1.12: Chemical structure of cellulose monomer	23
Figure 1.13: Depiction of hydrogen bonding between chains of cellulose (left image) and covalently bound glucose units which make up the cellulose chains (right image) ⁶⁹	24
Figure 1.14: Cellulose Ia and Ib unit cell ⁶⁹	25
Figure 1.15: Illustration of acid hydrolysis process to isolate cellulose crystalline domains ⁷¹	26
Figure 1.16: Schematic of basic SAXS experimental setup ⁸²	27
Figure 1.17: Elastic scattering depiction	28
Figure 1.18: Typical SAXS scattering profile and data that can be extracted (where q is the scattering vector and P the form factor) ⁷⁵	29
Figure 1.19: a) Molecular weight from various shaped proteins b) scattering curves demonstrating the intensity as a function of size c) guinier plots showing calculation of radius of gyration in	

<i>aggregated and non-aggregated systems d) pair distribution function for both aggregated and non-aggregated systems</i> ⁸⁶	30
<i>Figure 1.20: Example Kratky plot for determining folding behaviour of proteins in solution</i> ⁸⁶	31
<i>Figure 1.21: Braggs law diagram</i>	34
<i>Figure 1.22: Ewald sphere with 0 as the origin of reciprocal space</i>	35
<i>Figure 1.23: Schematic diagram of hot melt extruder</i> ¹⁰²	40
<i>Figure 3.1: Chemical structure of A) Paracetamol and B) Affinisol™ 15LV where n denotes the structural unit for Affinisol™</i>	46
<i>Figure 4.1: A) the transparent 3D-printed sample holder held in place with metal sample stage B) the transparent 3D-printed sample holder with extruded sample</i>	57
<i>Figure 4.2: XRPD reference patterns for Affinisol™ (black line) and paracetamol form I (red line)</i>	58
<i>Figure 4.3: XRPD patterns for paracetamol Affinisol™ ASDs produced at varying compositions at three different processing temperatures</i>	59
<i>Figure 4.4: THz Raman spectra for amorphous paracetamol (blue), crystalline paracetamol (black) and Affinisol™ (green)</i>	60
<i>Figure 4.5: THz Raman spectral evolution of 50 wt% paracetamol extrudate immersed in deionised water</i>	61
<i>Figure 4.6: 50 wt% extrudate before and after being immersed in water</i>	62
<i>Figure 4.7: X-ray diffraction patterns of 10 wt% paracetamol as a physical mixture and extrudates produced at different temperatures</i>	63
<i>Figure 4.8: WAXS data of dissolution profile of 10 wt% paracetamol extruded at 115, 130, 150 and 170°C. Profiles are at 115°C (Black), 130°C (Red), 150°C (Blue) and 170°C (Green) all at t=6 hours after introduction of 1 mL of deionised water using a syringe</i>	64
<i>Figure 4.9: X-ray diffraction patterns of 20 wt% paracetamol as a physical mixture and extrudates produced at different temperatures</i>	66
<i>Figure 4.10: WAXS data of dissolution profile of 20 wt% paracetamol extruded at 150 and 170°C. Profiles are at 150°C (Red) and 170°C (Blue) all at t=6 hours after introduction of 1 mL of deionised water using a syringe</i>	67

Figure 4.11: X-ray diffraction patterns of 25 wt% paracetamol as a physical mixture and extrudates produced at different temperatures	68
Figure 4.12: WAXS patterns of 25 wt% 150°C paracetamol ASD after wetting with deionised water	69
Figure 4.13: WAXS patterns of 25 wt% 170°C paracetamol ASD after wetting with deionised water	70
Figure 4.14: X-ray diffraction patterns of 27.5 wt% paracetamol as a physical mixture and extrudates produced at different temperatures	71
Figure 4.15: WAXS patterns of 27.5 wt% 150°C paracetamol ASD after wetting with deionised water	72
Figure 4.16: WAXS patterns of 27.5 wt% 170°C paracetamol ASD after wetting with deionised water	73
Figure 4.17: Schematic representation of crystallisation pathways during the dissolution of ASDs a) No residual crystallinity, limited surface crystallisation b) Residual crystallinity, surface crystallisation. Amorphous material = ●, crystalline material = ★	75
Figure 5.1: Demonstration of structural features present in SAXS vs XRPD data ⁹³	81
Figure 5.2: Pawley fit of the XRPD data of the starting material in the range of 3-40° two theta.	88
Figure 5.3: DSC profile of GSK2838232M in the range of 20-280°C	89
Figure 5.4: DSC heating (red line) and cooling (blue line) analysis of GSK2838232M	90
Figure 5.5: VT-XRPD diffractograms of GSK2838232M	91
Figure 5.6: Zoomed in VT-XRPD diffractograms highlighting peak shift between 30°C and 100°C profiles, profiles displayed up to 130°C.	92
Figure 5.7: Crystal lattice volume of GSK2838232M as a function of temperature as measured by VT-XRPD	93
Figure 5.8: XRPD plots of series of amorphous samples produced with a Retsch MM400 ball mill	94
Figure 5.9: DSC profiles of all ball milled GSK2838232M samples (Top plot 5 minutes to 40 minutes milling, bottom 45 minutes to 60 minutes milling)	95
Figure 5.10: Crystallinity values calculated from DSC data using enthalpy of crystallisation and enthalpy of melting	97
Figure 5.11: Mass loss trend analysis based on TGA data	99

Figure 5.12: Fingerprint region from IR analysis. Red = amorphous sample, green = crystalline sample	100
Figure 5.13: SEM image of GSK2838232M parent material. Scale bar indicated 50 μm	101
Figure 5.14: SEM images of milled samples, scale bar indicates 50 μm . a) 5 minute milled sample, b) 10 minute milled sample, c) 20-minute milled sample, d) 30-minute milled sample, e) 40-minute milled sample, f) 45 minute milled sample, g) 50-minute milled sample and h) 60 minute milled sample.	102
Figure 5.15: SEM image of X-ray amorphous material milled for 60 minutes at 30 Hz. Scale bar indicated 50 μm	102
Figure 5.16: Multi-well SAXS powder transmission sample holder	104
Figure 5.17: Powder GSK2838232M sample mounted in metallic washer between sticky Kapton film.	104
Figure 5.18: SAXS profiles of GSK2838232M mounted in three separate washers	105
Figure 5.19: Multiple position glass capillary sample holder	106
Figure 5.20: SAXS profiles of GSK2838232M mounted in three separate 0.7 mm borosilicate glass capillaries	107
Figure 5.21: 1D SAXS data of milled GSK2838232M samples	108
Figure 5.22: SAXS Porod invariant analysis of GSK2838232M and subsequent milled samples	110
Figure 6.1: Transmission Electron Microscopy (TEM) images of MFC (left) and NFC (right) ¹⁸⁹	115
Figure 6.2: Schematic diagram of the fibre production process: 1- Ultra Turrax; 2- mixing beaker; 3- syringe pump; 4- syringe; 5- conical needle; 6- roller; 7- wind-up drum; 8- coagulation bath; 9- rinsing bath; 10- solvent exchange bath; 11- drying rack.	118
Figure 6.3: Mounted Fibre and film cellulose samples. A) Pure alginate fibres B) Post stretched alginate fibres C) Microfibrillated cellulose fibres D) Post stretched microfibrillated cellulose fibres E) Nanofibrillated cellulose fibres F) Pure alginate film G) Microfibrillated cellulose Film H) Nanofibrillated cellulose film. Samples mounted in 10 mm diameter washers	119
Figure 6.4: Capillary XRPD data of sodium alginate powder derived from brown algae, in the range of 5-80° two theta	122

<i>Figure 6.5: 2D detector image of pure alginate fibre in the absence of cellulose. Arrows depict the direction of integration. Arrow in the horizontal direction shows integration perpendicular to the alignment of the fibres. Arrow in the vertical direction shows integration parallel to the alignment of the fibres. Samples mounted as described in section 6.2.1.2 and data integration as described in section 6.2.1.2.</i>	124
<i>Figure 6.6: 1D WAXS data of pure alginate fibres from integrated 2D image</i>	125
<i>Figure 6.7: Integration of WAXS data for pure alginate fibres, perpendicular (left) and parallel (right) to the direction of the mounted fibre</i>	126
<i>Figure 6.8: 2D detector image of pure alginate fibres, which had been subjected to stretching after spinning</i>	127
<i>Figure 6.9: 1D WAXS data from integrated 2D image of pure alginate fibres which have been subject to stretching after spinning</i>	128
<i>Figure 6.10: Integration of WAXS data for pure alginate fibres which have been stretched after spinning, perpendicular (left) and parallel (right) to the direction of the mounted fibre</i>	128
<i>Figure 6.11: 2D detector image of microfibrillated cellulose fibres labelled with reflections of the most intense peaks associated with cellulose</i>	129
<i>Figure 6.12: 1D WAXS data from integrated 2D image of microfibrillated cellulose fibres labelled with reflections of the most intense peaks associated with cellulose</i>	130
<i>Figure 6.13: Integration of WAXS data for microfibrillated cellulose fibres perpendicular (left) and parallel (right) to the direction of the mounted fibre.</i>	131
<i>Figure 6.14: 2D detector image of microfibrillated cellulose fibres which have been subject to stretching after spinning</i>	132
<i>Figure 6.15: 1D WAXS data of microfibrillated cellulose fibres which have been subject to stretching after spinning from integrated 2D image</i>	133
<i>Figure 6.16: Integration of WAXS data for microfibrillated cellulose fibres which have been subject to stretching after spinning, perpendicular (left) and parallel (right) to the direction of the mounted fibre</i>	134
<i>Figure 6.17: 2D detector image of nanofibrillated cellulose fibres</i>	135

<i>Figure 6.18: 1D azimuthal integration plot of nanofibrillated cellulose fibres from integrated 2D image</i>	136
<i>Figure 6.19: Integration of WAXS data for nanofibrillated cellulose fibres perpendicular (left) and parallel (right) to the direction of the mounted fibre</i>	136
<i>Figure 6.20: 2D detector image of alginate film containing no cellulose</i>	137
<i>Figure 6.21: 1D azimuthal integration plot of alginate film from integrated 2D image</i>	138
<i>Figure 6.22: 2D detector image of nanofibrillated cellulose film</i>	139
<i>Figure 6.23: 1D plot of nanofibrillated cellulose film from integrated 2D image</i>	139
<i>Figure 6.24: 2D detector image of microfibrillated cellulose film</i>	140
<i>Figure 6.25: 1D plot of microfibrillated cellulose film from integrated 2D image</i>	141
<i>Figure 6.26: Azimuthal profile of all fibre and film samples based on the 200 reflection</i>	142
<i>Figure 6.27: Azimuthal profile of all fibre and film samples based on the 110 reflection</i>	143
<i>Figure 7.1: SAXS Porod invariant analysis of GSK2838232M and subsequent milled samples</i>	152

List of Tables

<i>Table 1.1: Pharmaceutical Solid Form Summary</i>	3
<i>Table 1.2: Polymorphic organic compounds melting point data</i>	11
<i>Table 1.3: Solubility comparison of co-crystal material versus pure compound</i>	12
<i>Table 1.4: Commercially available products utilising an amorphous form API</i>	17
<i>Table 4.1: Bin blender parameter settings for mixing of physical mixtures prior to hot melt extrusion</i>	56
<i>Table 4.2: Hot melt extrusion parameters for manufacturing of ASDss</i>	56
<i>Table 4.3: WAXS instrument collection parameters used for dissolution studies</i>	57
<i>Table 5.1: Ball milling parameters used to produce amorphous samples</i>	84
<i>Table 5.2: Instrument parameters used for SAXS experiments</i>	85
<i>Table 6.1: Orientation index values for all fibre and film samples calculated from azimuthal integrations of the 200 and 110 reflections</i>	144
<i>Table 6.2: Percent crystallinity values for all fibre and film samples calculated using Segals method and the deconvolution method</i>	145

Chapter 1: Introduction

1.1 Thesis Overview

X-ray scattering techniques allow for a wide range of length scales to be studied (Figure 1.1). These techniques enable a wide range of materials and material properties to be studied.

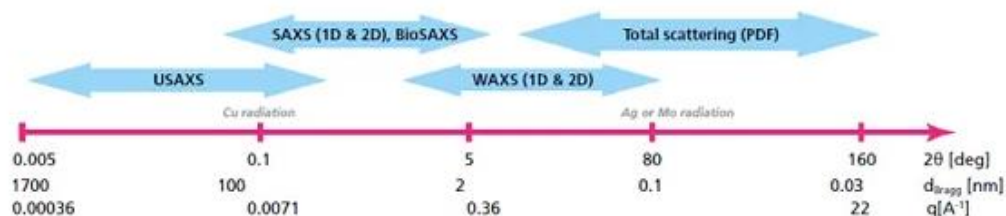


Figure 1.1: Depiction of length scales accessible through X-ray scattering techniques

Wide angle X-ray (WAXS) scattering probes systems at the angstrom and sub angstrom range at a two theta greater than 10° . This technique gives access to information on the molecular arrangement of materials. As such, one of the main applications of WAXS is in the study of crystal structure in drug and polymer systems by measuring interatomic spacings within the lattice. Small angle X-ray scattering (SAXS) provides information on ordered and disordered materials at a greater length scale than can be achieved using WAXS, giving us information on the nano and meso scale. Unlike WAXS, SAXS does not rely on crystalline material to produce a signal making it suitable for a variety of applications.

X-ray scattering is used in the analysis and characterisation of a myriad of materials including polymers, films, crystalline samples, mesoporous materials, liposomes, biomolecules in solution and many more. The work presented in this thesis focuses on the application of X-ray scattering in the areas of amorphous

drugs for quantification and observation of phase transformation, and the study of cellulose materials to determine relative crystallinity and orientation.

1.1.1 Background on Solid State Pharmaceutical Ingredients

An active pharmaceutical ingredient (API) can exist in multiple solid-state forms, including crystalline, amorphous, solvates, co-crystals, salts and polymorphs (see Figure 1.2 and Table 1.1).

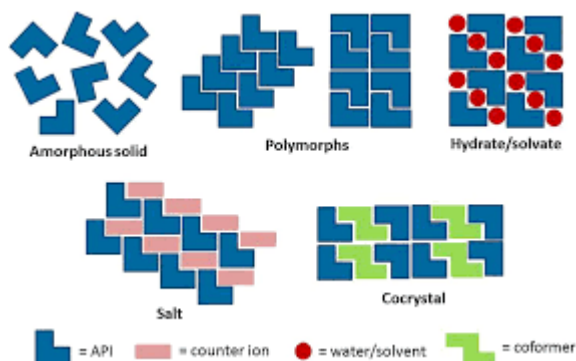


Figure 1.2: Molecular arrangements of organic solids with organised crystal solid forms and disordered amorphous solid¹

Table 1.1: Pharmaceutical Solid Form Summary

Solid Form	Description
Amorphous solid	Contains no long-range ordering
Polymorph	A form of isomerism where a solid material consisting of the same constituents can exist in different crystalline structures
Hydrate/Solvate	A crystalline molecule containing water or solvent within the crystal lattice
Salt	Consists of positive cations and negative anions to give a compound with no electrical charge
Co-crystal	Neutral crystalline material consisting of two or more materials

Oral solid dosage forms account for around 90% of the pharmaceutical formulations intended for human use,^{2,3} and are most commonly manufactured as tablets or capsules due to the low manufacturing cost and ease of administration for patients.^{4,5} The performance of an oral solid dosage form is heavily impacted by the physical form of the API as the physical form plays a role in many of the physical properties such as solubility, stability and manufacturability.⁶ Therefore, it is of critical importance for drug development to identify and control the physical forms of the API.

Characterisation of the solid state of API is an essential step during drug development.⁷ The crystalline state has historically been the most widely used due to the stability offered.^{8,9} A growing concern in the pharmaceutical industry is the poor solubility of many new chemical entities (NCE).^{10,11} To allow for the categorisation of these drugs, a system was suggested in 1995¹² known as the biopharmaceutics classification system (BCS), which allows for drugs to be sorted into one of four categories based on their solubility and permeability properties. This classification system is shown in Figure 1.3. Estimates put the amount of NCE in BCS II and IV at approximately 90%. The poor solubility of NCEs results in many newly developed promising compounds no longer actively being pursued at an early stage due to the bioavailability issues associated with low solubility. As such, it is paramount that formulation scientists utilise all available tools to allow more of these compounds to make it to market.

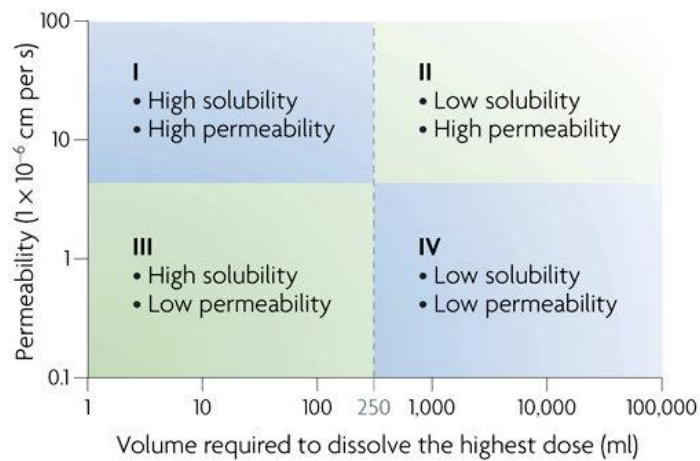


Figure 1.3: Biopharmaceutics Classification System (BCS) based on drug solubility and permeability parameters¹³

There are several strategies currently employed as a means of improving solubility such as lyophilisation,¹⁴ particle size reduction,¹⁵ use of salt form¹⁶ amongst others. Currently one of the most promising strategies is to use the amorphous form of a drug.^{17,18}

Amorphous pharmaceuticals used in combination with polymers to produce an amorphous solid dispersion (ASD) are commonly used due to the inhibition of crystallisation provided by the polymer. The use of a polymer with a high glass transition temperature (T_g) causes the T_g of the dispersion to be higher than that of the purely amorphous drug. The lower T_g , in turn, lowers the mobility of the drug within the system, hampering the interactions between the drug molecules and inhibiting crystallisation (see Figure 1.4). The intermolecular bonds between the drug and polymer also act as a stabiliser by limiting the movement of the drug within the dispersion and, therefore, not allowing interaction between the drug molecules.

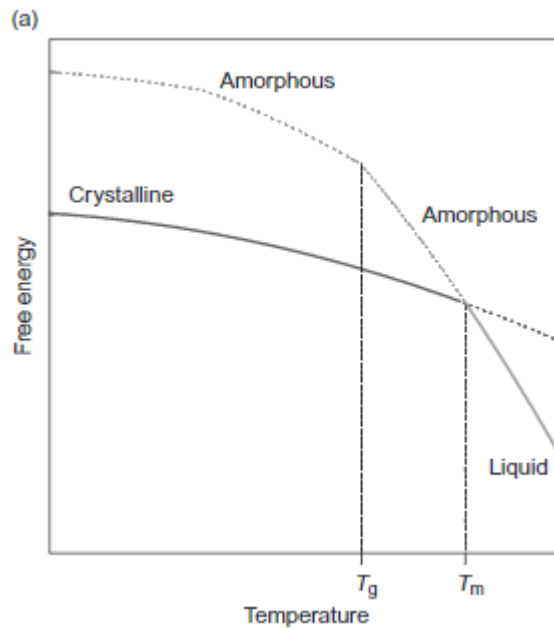


Figure 1.4: Free energy vs temperature diagram for amorphous and crystalline solids¹⁹

Introduction of the ASD to liquid, when swallowed or during routine Quality Control (QC) dissolution testing, often results in recrystallisation of the drug and can also cause phase transformations. This recrystallisation then negates the solubility advantage associated with the amorphous form of the drug. Avoiding recrystallisation is, therefore, a priority when developing such formulations such that the stability of the amorphous phase can be carried over into the dissolution testing.

Small angle X-ray scattering techniques are useful in the analysis of non-crystalline materials and give us insight into colloidal materials such as cellulose. The crystalline structure of cellulose has been subject to extensive research since its discovery. The structure of cellulose was first reported in 1858²⁰ with this being confirmed almost 100 years later by X-ray crystallography.²¹ Since this early work,

X-ray scattering methods have extensively been used for the characterisation of cellulose and cellulose containing materials. Wide angle X-ray scattering is routinely used to determine the structure and orientation of cellulose nanocrystals (CNC) and the overall crystallinity of cellulose based materials.^{22,23} Crystallinity is an important property to consider when dealing with cellulose as it can impact on the mechanical properties. Materials with a higher crystallinity have been shown to possess a greater Young's modulus, hardness and tensile strength.²⁴ Small angle X-ray scattering has more recently become an analytical tool for studying cellulose, providing information on the nanostructure.²⁵ The use of X-ray scattering analysis in cellulose research has played a vital role in the use of fibrillated cellulose as a strengthening reinforcement for a variety of materials.^{25,26,27}

1.2 Pharmaceutical Solid Form

The preferred dosage form remains to be that of a solid oral dosage form, this is due to the ease of administration leading to high patient compliance and potential for large-scale manufacturing. The solid form can be classified into two categories, crystalline and amorphous which can then be further split into more subcategories. The most commonly used form is the crystalline form. This form contains both short- and long-range ordering and can be found in a variety of subcategories shown in Figure 1.5. The difference in packing and conformation of these various crystalline forms leads to differing properties for the same parent drug. By contrast, amorphous solids contain no long-range ordering.

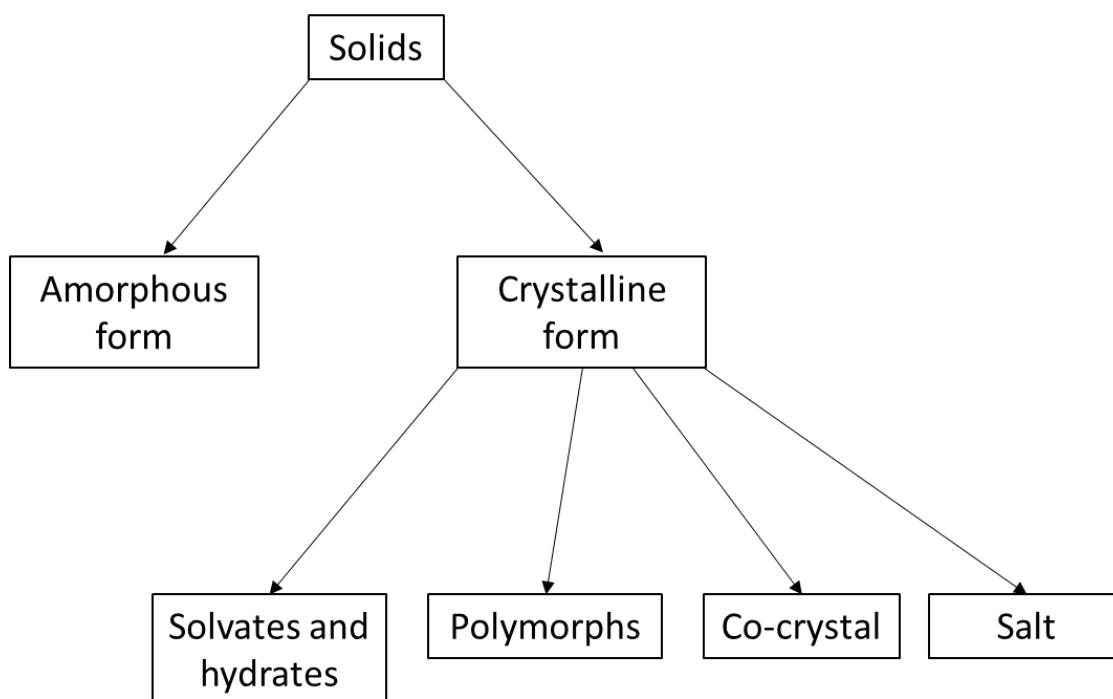


Figure 1.5: Schematic of solids classification of most appropriate pharmaceutical forms²⁹

1.2.1 Crystalline Pharmaceuticals

The majority of pharmaceutical dosage forms contain a crystalline API due to the stability afforded in this form.³⁰ In crystalline systems, atoms are arranged and repeated in three dimensions to form a highly ordered crystal lattice that is held together by non-covalent interactions. A given lattice is comprised of unit cells which are the same size and contain the same number of atoms packed in the same way. The unit cell is described by the three vectors a , b and c and angles of α , β and γ . There are seven possible simple crystal unit cells shown in Figure 1.6.

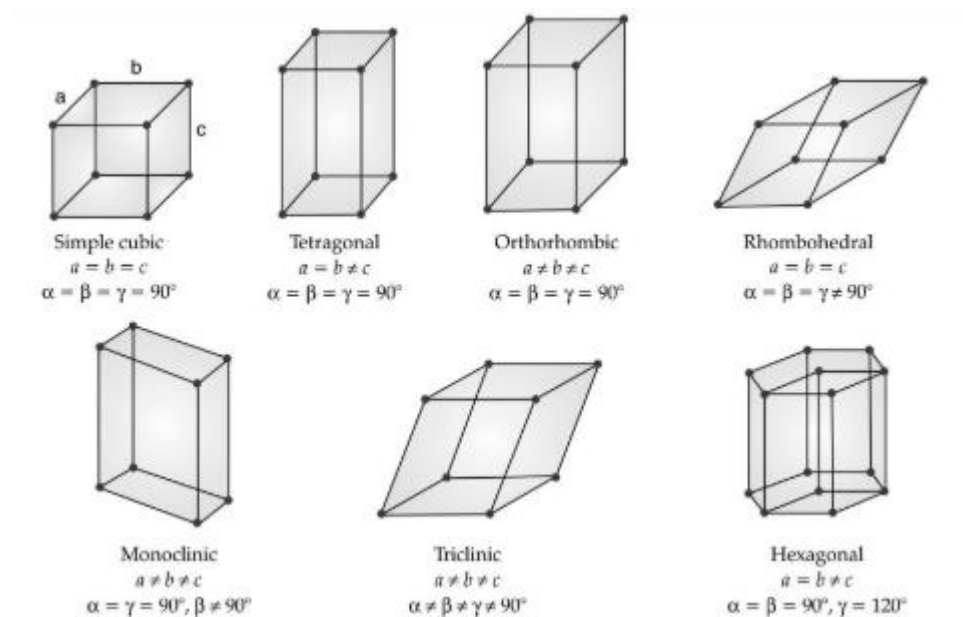


Figure 1.6: Seven Simple Unit Cells

Commonly, pharmaceuticals fall into three categories, orthorhombic, monoclinic, and triclinic, owing to their relatively complex structures resulting in lower symmetries.

It is this arrangement of atoms which determines the physical properties of the material and has a bearing on properties such as morphology, particle size, and polymorphism. These properties then affect the performance of the drug by impacting the dissolution and bioavailability along with tableting and flow properties of the material. With so much knowledge and information available about crystalline systems, these systems are the go-to for early-stage development challenges. However, the same advantages afforded through the crystalline phase also result in some unfavourable properties for pharmaceuticals. Due to the low internal free energy that gives rise to the stability of the crystalline form, crystalline compounds can also result in poor solubility and dissolution performance.^{31,32} The use of the amorphous form can give rise to improved

solubility owing to the higher energy of this form in comparison to the crystalline form of the drug. This increased solubility can then lead to increased dissolution rates and bioavailability. However, the higher energy of the amorphous form also comes with an inherent propensity to convert from the metastable amorphous form back to the more stable and less soluble crystalline form.

A compound can exist in different crystal forms as shown in Figure 1.5. Polymorphs are different crystalline forms that result from various arrangements and various orientations of the molecule in the unit cell. These differences can impact the properties of the polymorph such as stability, solubility, melting point and morphology (see Table 1.2). While many polymorphic forms can exist, one form will have the lowest free energy and thus will be the most thermodynamically stable.

Table 1.2: Polymorphic organic compounds melting point data

Compound	Polymorph	Melting point (°C)
Paracetamol $C_8H_9NO_2$	Form I ³³ Monoclinic $P2_1/n$ $a= 12.930 \text{ \AA}$ $b= 9.400 \text{ \AA}$ $c= 7.100 \text{ \AA}$	169
	Form II ³⁴ Orthorhombic P_{cab} $a= 7.406 \text{ \AA}$ $b= 11.837 \text{ \AA}$ $c= 17.162 \text{ \AA}$	155-157
	Form III ³⁵ Orthorhombic $P_{ca}2_1$ $a= 11.837 \text{ \AA}$ $b= 8.560 \text{ \AA}$ $c= 14.818 \text{ \AA}$	182
Ritonavir	Form I ³⁶ Monoclinic $a= 13.433 \text{ \AA}$ $b= 5.293 \text{ \AA}$ $c= 27.092 \text{ \AA}$	122
	Form II ³⁶ Orthorhombic $a= 10.024 \text{ \AA}$ $b= 18.674 \text{ \AA}$ $c= 20.469 \text{ \AA}$	122
Mefenamic Acid	Form I ³⁷ Triclinic P1 $a= 14.556 \text{ \AA}$ $b= 6.811 \text{ \AA}$ $c= 7.657 \text{ \AA}$	230
	Form II ³⁷ Triclinic P1 $a= 7.758 \text{ \AA}$ $b= 9.277 \text{ \AA}$ $c= 9.399 \text{ \AA}$	233

Hydrates and solvates are a result of the crystallisation solvent being incorporated into the crystal lattice. Hydrates and solvates show differences in physicochemical properties when compared with the non-solvated form and have the potential to improve the performance of the compound for use in formulated dosages.

Co-crystals involve two or more compounds contained within the same crystal lattice where one compound is the API and are commonly used in crystal engineering to manipulate the performance properties of the final product. Successful co-crystallisation results in both starting products remaining unionised and held together by intermolecular interactions. Work investigating co-crystallisation looks to design systems that match potential APIs to cofomers by examining the hydrogen bond donors and acceptors of both and selecting those which have complementary structures (see Table 1.3).

Table 1.3: Solubility comparison of co-crystal material versus pure compound

Compound	Cofomer	Solubility / Dissolution
Acyclovir	Tartaric acid	The dissolution rate is much higher than that of the polymorphic forms. ³⁸
Carbamazepine	Cinnamic acid	Increased dissolution rate and solubility in comparison to pure carbamazepine. ³⁹
	Nicotinamide, Fumaric acid	Increased solubility in comparison to pure carbamazepine. ⁴⁰
Indomethacin	Saccharin	Increased solubility over a range of pH compared with pure indomethacin. ⁴¹

A majority of APIs exist as either a weakly basic or acidic compound which means salt formation is a possible alternative to crystallisation allowing researchers to tweak the physicochemical properties of the final drug product. Many of the current medicines on the market are salt forms. Salt formation is a result of proton transfer between ionisable functional groups to create a hydrogen bond. When selecting an appropriate counterion to form a salt complex there are a number of criteria which can be considered. Firstly, safety is important as the salt form must be safe for human consumption. pKa differences between the acid and the base should also be considered with a difference of three or more pKa units resulting in a greater likelihood of producing a salt.

1.2.2 Amorphous Pharmaceuticals

Amorphous solids differ from crystalline solids in that they only contain short-range ordering due to hydrogen bonding and other non-covalent forces but have no long-range ordering of atoms characteristic of crystalline materials.⁴² This results in a random orientation of the atoms allowing the same molecule to form many varying conformations. This lack of order associated with amorphous materials results in no lattice planes which would be seen in a crystalline material. Therefore, X-rays scattered by an amorphous material form what is known as an amorphous halo during an X-ray powder diffraction (XRPD) experiment, as shown in Figure 1.7.

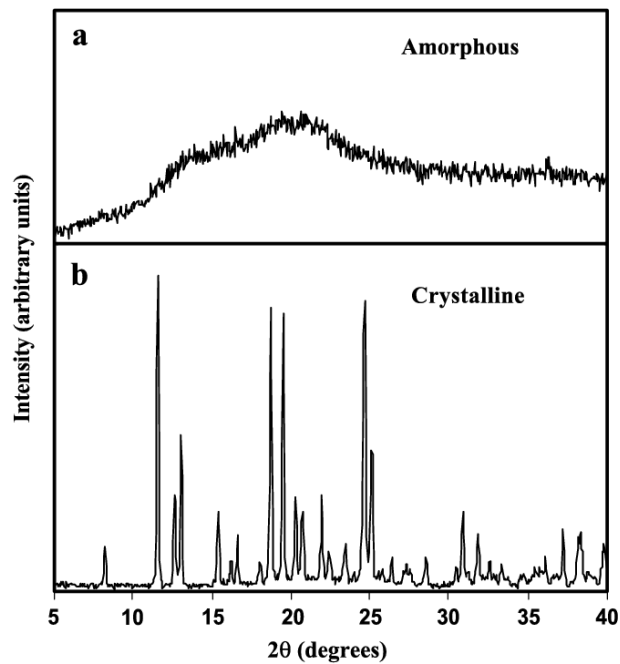


Figure 1.7: Example amorphous (a) vs crystalline (b) XRPD patterns of Sucrose⁴³

The state of an amorphous solid is generally described in two ways, “glassy state” or “rubbery state”.^{44,45} The state in which an amorphous solid is formed is governed by the T_g . Below the T_g , amorphous solids are considered to be in the glassy state; in this state, molecular mobility is limited and stability is increased due to the limited number of interactions possible. Above the T_g , the amorphous solid enters the rubbery state which is similar to a supercooled liquid in its behaviour. In this state, there is greater molecular mobility which can lead to crystallisation.

Amorphous solids contain higher free energy than the crystalline form meaning they can be considered metastable. This increased free energy can lead to improved solubility and therefore increased bioavailability, making them a promising candidate for poorly soluble drugs.^{46,47} With these improved properties also come disadvantages, with the main one being the tendency for an amorphous

form to crystallise back to a more stable form.^{48,49} Thus, the inhibition of this crystallisation behaviour through the use of additives has become a popular technique.^{50,51}

Two major forces are competing within an amorphous solid, the thermodynamic tendency for crystallisation and the low molecular mobility which hinders crystallisation (Figure 1.8).

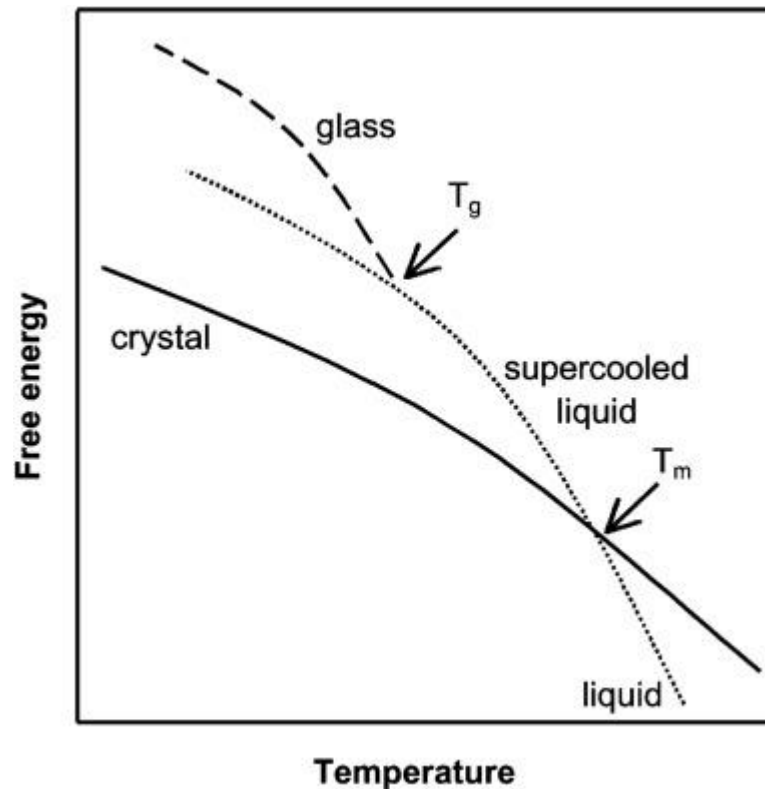


Figure 1.8: An example of a free energy - temperature phase diagram. T_m represents the melting temperature above which the liquid is in its stable form, with the crystal phase at the lowest free energy phase below T_m . T_g represents the glass transition temperature⁵²

As the temperature is decreased to below the melting point, there is a driving force towards nucleation of the molecule. By contrast, when the temperature is lowered

and nears T_g , there is a decrease in molecular mobility which hinders molecular rearrangement and stops the transformation to the crystal form.⁵³ Due to the improvement of solubility and bioavailability afforded through the amorphous form in comparison to other solubility enhancement techniques,^{11,54} it is of great importance to understand the physicochemical properties to allow for more routine use of the amorphous form.

1.2.3 Solid Dispersions / Amorphous Solid Dispersion

There are numerous examples of the amorphous form of a drug showing a marked improvement in solubility when compared to the crystalline form.^{55,56} However, the number of marketed products containing an amorphous API remains relatively low, but there are examples of marketed medicines employing an amorphous API. This is due to the instability associated with working with amorphous compounds. A lot of research has been conducted regarding the physical stability of amorphous materials and possible mechanisms that can lead to increased stability, however, there is still a lack of understanding in this area. This is the primary reason for research into ASD systems. These are systems which contain the amorphous drug mixed with an excipient, usually a polymer, which acts as an inhibitor to the crystallisation. Examples of ASD systems currently on the market can be seen in Table 1.4.

Table 1.4: Commercially available products utilising an amorphous form API

Product Name	Compound	Carrier Polymer	Manufacturing Method	Company Name
Lozanoc	Itraconazole [®]	HPMCP ¹	Spray Drying	Mayne
Intelence	Etravirine [®]	HPMC ²	HME ³	J & J
Gris-Peg	Griseofluvin [®]	PEG ⁴ 6000	Melt Extrusion	Pedinol
Norvir	Ritonavir [®]	PVP ⁵	HME	Abbvie

¹ Hydroxypropyl methylcellulose phthalate

² Hydroxypropyl methylcellulose

³ Hot Melt Extrusion

⁴ Polyethylene Glycol

⁵ Polyvinylpyrrolidone

The polymer in these systems is thought to act in a number of ways which inhibit the crystallisation of the amorphous drug. Firstly, it is generally considered that the formation of intermolecular bonds between the drug and polymer, such as hydrogen bonding or Van der Waals interactions, is the main inhibitor of crystallisation. Another assumption for these systems is that the polymer acts as somewhat of a physical barrier, in that it physically stops the drug molecules from interacting with each other due to the bulky polymer chains. The last assumption is that due to the high glass transition temperature of the polymer, the T_g in the dispersion is raised in comparison to the pure amorphous drug which then lowers the molecular mobility and inhibits the crystallisation.^{57,58} The performance of the polymer chosen as a means of inhibiting crystallisation will be based on the degree of miscibility between the drug and polymer.⁵⁹

1.3 Dissolution

1.3.1 Dissolution Theory / History

Dissolution testing is an *in-vitro* test used to evaluate drug release from its dosage form, playing an important role in product development as well as regulatory matters. Generally thought of as a solid to liquid process, it looks at the rate at which the solid dissolves into the liquid phase to produce a solution which is one homogenous phase.⁶⁰ For a dissolution process to occur several processes are needed, mainly the bonds within the solid phase need to be broken which then allows solid particles to be incorporated into the liquid phase to create the solution (see Figure 1.9).

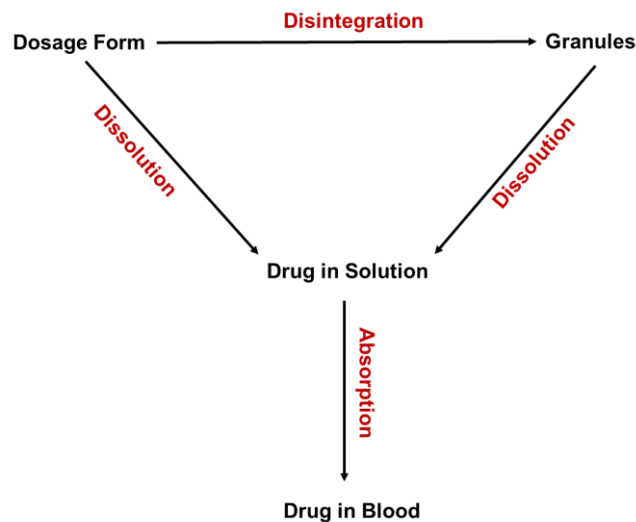


Figure 1.9: Schematic of Simple Representation of Dissolution Process

Dissolution of solids is described by the Noyes and Whitney⁶¹ model along with the Nernst model.⁶² Binary mixtures have a more complex dissolution process which led to the Higuchi model being developed in the 1960s.⁶³ Further developed by Van Drooge⁶⁴ to describe ASD dissolution by including phase transitions from amorphous to crystalline.

The first relationship used to describe the dissolution rate was published in 1897 and is known as the Noyes-Whitney equation,⁶¹ although published over 100 years ago the relationship is still valid and used in dissolution studies. Describing the rate of solution of solids for diffusion-controlled processes, by,

$$\frac{dC}{dt} = k(C_s - C) \quad \text{Eqn. 1.1}$$

The terms of the equation are dC/dt which is the solute dissolution rate, C_s is the particle saturation concentration, C is the concentration in the bulk solution and k is the rate constant of the dissolution. As more understanding of dissolution was obtained variations of this original equation began to be published. The first coming in 1900 from Brunner, this new relationship began to consider more parameters which could affect the dissolution performance. Parameters such as surface area, temperature and type of apparatus used are included. Eqn 1.2 demonstrates the inclusion of surface area (S).

$$\frac{dC}{dt} = K_1 S(C_s - C) \quad \text{Eqn. 1.2}$$

Brunner then further expanded on this work a few years later with the help of Nernst, leading to the Nernst-Brunner equation now considering diffusion processes as described by Fick's second law of diffusion. Where D is the diffusion coefficient, V the volume of dissolution medium and h the thickness of the diffusion layer.

$$\frac{dC}{dt} = \frac{DS}{Vh}(C_s - C) \quad \text{Eqn. 1.3}$$

It was not until much later that researchers began to realise the importance of the absorption process in the gastrointestinal tract (GI). In the 1950s studies began to show that when a drug is absorbed quickly in the GI tract the dissolution rate of

the drug is then the limiting factor for its performance in the body. Moving into the 1960s and 70s the research moved to look at the impact of dissolution on the prediction of bioavailability, with a focus on the effect of the formulation in effectively delivering the drug. With this new knowledge, the importance of dissolution testing was realised, and the first pharmacopoeia monographs containing dissolution testing as a quality control test began to appear.

1.3.2 Dissolution of Amorphous Solid Dispersions

The dissolution profile of ASDs is of high importance when it comes to researching and understanding such systems. Research has shown that in its amorphous form a molecule can have a much higher drug release when compared to the crystalline alternative as shown in Figure 1.10.

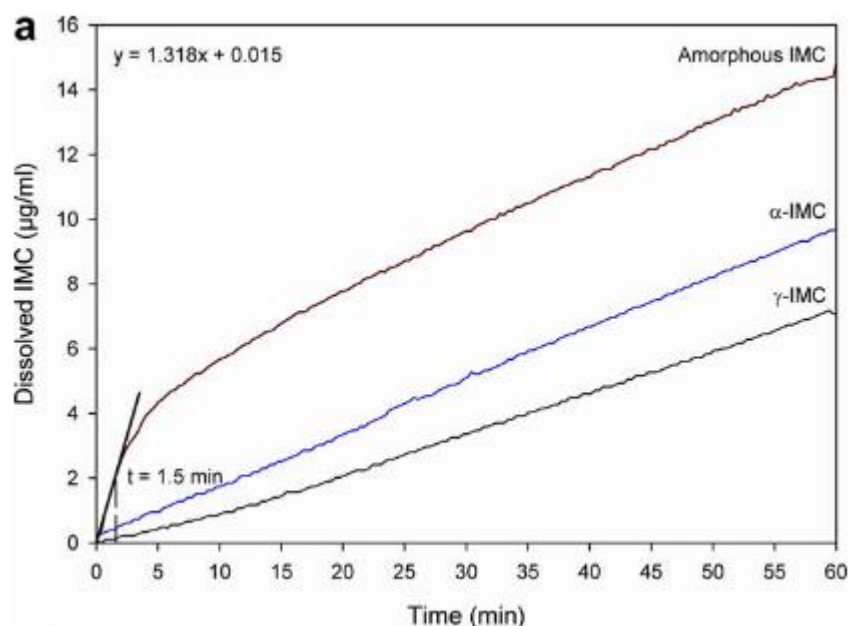


Figure 1.10: Comparison of amorphous and crystalline indomethacin dissolution profiles⁶⁵

The spring and parachute drug model is routinely used to characterise ASD dissolution profiles where the polymer is being used as an inhibitor for crystallisation. This model describes an initial build-up of drug supersaturation (spring) which is then followed by a period of precipitation (parachute).⁶⁶ The difference in dissolution profile in comparison to a crystalline drug is shown in Figure 1.11.

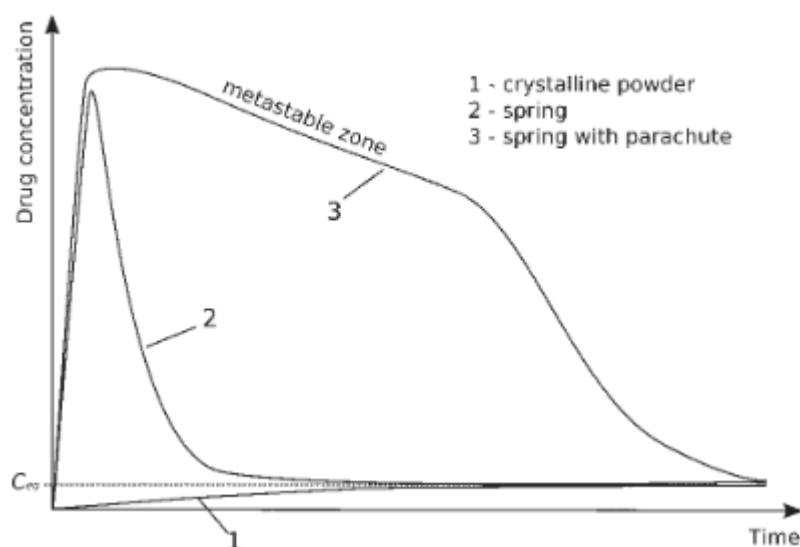


Figure 1.11: Dissolution profile comparison of amorphous and crystalline drug⁶⁷

1.3.3 Crystallisation during dissolution

ASDs can undergo a crystallisation process during dissolution in two ways. Firstly through a solid to solid transformation where the ingress of water allows for greater molecular mobility within the system leading to a greater chance of crystallisation.⁶⁵ The other process which can take place is solution mediated crystallisation where the drug forms a supersaturated solution, where the concentration is higher than the stable form.⁶⁸ Both of these processes are characterised by an initial nucleation and then crystal growth.

Nucleation is the first step in crystallisation, where stable aggregates are formed from the supersaturated solution and is vital to the stability of ASDs. This process is a first-order phase transition which follows first order kinetics. Nucleation is described through two mechanisms, homogenous and heterogeneous nucleation. Homogenous nucleation takes place with no external input and is a rare process as most systems will contain some level of impurity. Heterogeneous nucleation occurs when nuclei form at a preferred site within the system such as an existing crystal or the walls of the vessel.

Once nucleation has occurred crystal growth begins within the system. When considering ASDs, the nucleation step becomes the rate-limiting step as the polymer presence works to inhibit the nucleation beginning. The speed at which crystal growth takes place is affected by the rate of diffusion of molecules to the surface of the crystal and then how quickly they can be accepted into the crystal lattice.

1.4 Cellulose

Cellulose is the most abundant naturally occurring polymer on earth, being found in primary and secondary plant cell walls where it acts as structural support to provide protection to the cells. It is predominantly produced by plants, however, it is also found in other organisms such as bacteria and fungi but at a much lower yield when compared with cellulose from plants. As cellulose is found primarily in plants it is a renewable material that can be sourced all over the world and is also biodegradable as it simply decomposes over time.

1.4.1 Cellulose Structure

Cellulose is a complex carbohydrate polymer (see Figure 1.12) comprised of chains based on anhydro- β -D-glucopyranose units covalently bound by β -(1-4) glycosidic linkages. The monomer units are linked with hydrophilic interactions between equatorial hydroxyl groups and acial hydrophobic methanetriyl groups (see Figure 1.13).²⁴ The hydrophobic and hydrophilic interactions that occur due to these groups contribute to the high mechanical strength associated with cellulose.

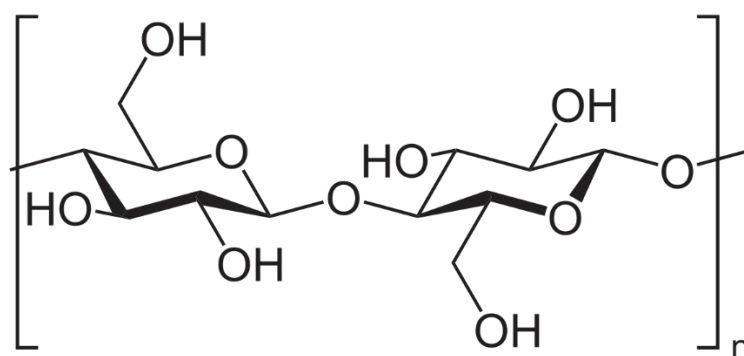


Figure 1.12: Chemical structure of cellulose monomer

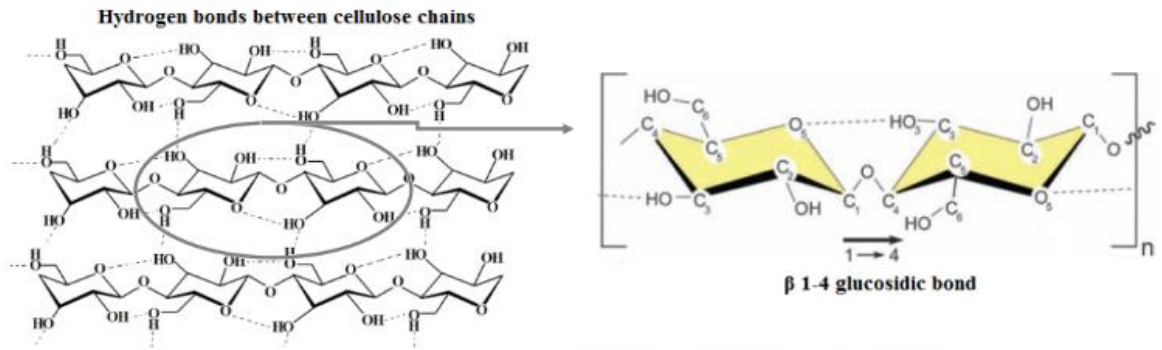


Figure 1.13: Depiction of hydrogen bonding between chains of cellulose (left image) and covalently bound glucose units which make up the cellulose chains (right image)⁶⁹

The degree of polymerisation (DP) of cellulose is an important property when considering the structure. The DP is a description of the chain length and can affect the mechanical and physiological properties of cellulose. The usual range of DP is 300 to 15,000 and this is dependent on the source used to obtain the cellulose.⁷⁰

The mechanical properties associated with cellulose arise from the linear structure of cellulose, the monomer units are bonded by a mixture of both intra and inter-molecular hydrogen bonds between the three hydroxyl groups on each repeating unit. This bonding process results in linear microfibrils being present in lignocellulosic biomass which are highly crystalline and are comprised of both crystalline and amorphous regions, through acid hydrolysis the cellulose nanocrystals can be isolated.

There are four known polymorphs of cellulose (I, II, III and IV). Cellulose I is native cellulose which exists in two different forms; Ia which is a triclinic unit cell and Ib

which has a monoclinic unit cell (see Figure 1.14). These polymorphs are commonly characterised using X-ray diffraction, nuclear magnetic resonance (NMR) and Fourier transform infrared (FTIR) spectroscopy. Cellulose I can also be converted to cellulose II through mercerization and cellulose III by treatment in an ammonia solution.

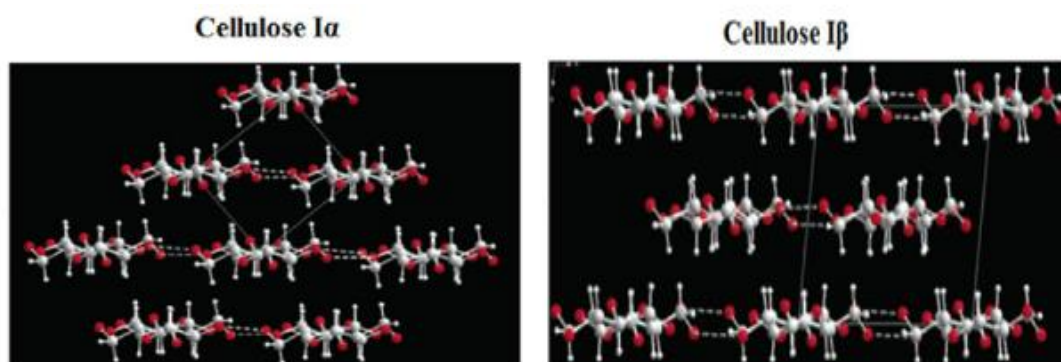


Figure 1.14: Cellulose I α and I β unit cell⁶⁹

Unit cell parameters have been widely published in the literature for both unit cells, I α parameters of $a=0.672$ nm, $b=0.596$ nm, $c=1.040$ nm, $\alpha=118.08^\circ$, $\beta=114.80^\circ$ and $\gamma=80.375^\circ$, I β parameters of $a=0.778$ nm, $b=0.820$ nm, $c=1.038$ nm, $\alpha=90^\circ$, $\beta=90^\circ$ and $\gamma=96.5^\circ$.

1.4.2 Cellulose nanomaterials

Cellulose nanomaterials is a broad term which is used to describe both cellulose nanocrystals (CNCs) and cellulose nanofibrils (CNFs). Cellulose, in its natural form, is found in a rod-like shape which is due to the microfibril nature of the cellulose chains. Within the chains, there are many cellulose crystals which are separated by amorphous regions. As mentioned in section 0 the crystalline

domains can be released through cleavage, usually in the form of an acid hydrolysis procedure (Figure 1.15), which results in the production of CNCs.

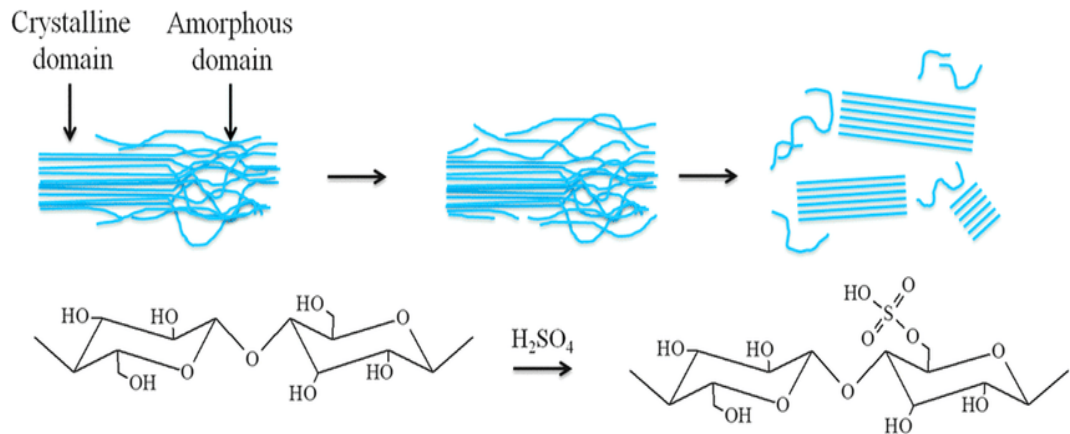


Figure 1.15: Illustration of acid hydrolysis process to isolate cellulose crystalline domains⁷¹

Due to the elastic modulus and chemical and thermal properties associated with cellulose nanocrystals they are commonly used as a means of strengthening other materials.^{28,72} CNFs and fibrillated cellulose (microfibrillated cellulose (MFC) and nanofibrillated cellulose (NFC) are then subsequently produced through mechanical treatment of the isolated CNC material.

MFC and NFC are formed from microfibrils which are formed into a large unit, the dimensions of MFC are in the range of 10 to 40 nm diameter with a length greater than 1,000 nm.⁷³ NFC diameter is approximately 5-20 nm with a length greater than 1,000 nm.⁷⁴ Both NFC and MFC are sourced from a number of starting materials with the main material used being wood. As wood is widely used across many industries alternative greener materials should be sourced for the production of MFC.

1.5 Analytical Techniques

1.5.1 Small Angle X-Ray Scattering

SAXS is a tool used in structural analysis applications for structural details within the nanoscale range from approximately 1 to 150 nm. It provides information on the size and shape as well as the internal structure of disordered materials.⁷⁵ It can be used to provide insight into many fields due to the information obtainable, including porous materials,^{76,77} nanomaterials,^{78,79} polymers^{80,81} and many more.

The most basic description of how SAXS works is a sample is illuminated by an X-ray beam, which then causes characteristic scattering of the sample which is then read by a detector. A schematic of a typical SAXS instrument is shown in Figure 1.16.

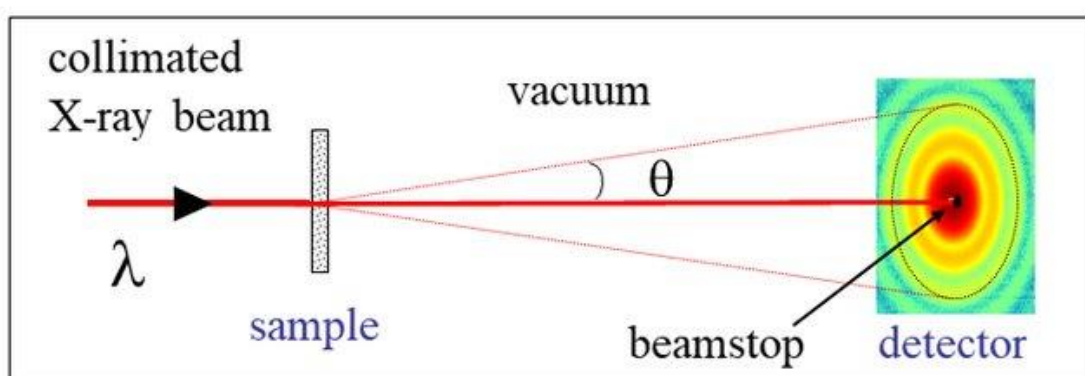


Figure 1.16: Schematic of basic SAXS experimental setup⁸²

When illuminated by the beam, small contrasting features within the sample cause the beam to deviate from its path, it is this scattered beam that is then measured on a detector to provide information on the system. The scattering is angle-dependent and is, therefore, able to be used to determine information regarding the particle structure. As a technique, SAXS is used for the analysis of the size

and shape of particle systems to resolve the structure. It uses elastic scattering (Figure 1.17) where the X-rays are scattered by the electrons in the system, which tells us that for SAXS to provide information on a system there must be a contrast in the electron density. If the sample and the buffer/matrix it resides in have the same electron density, they will produce the same signal and therefore no useful information can be gathered.

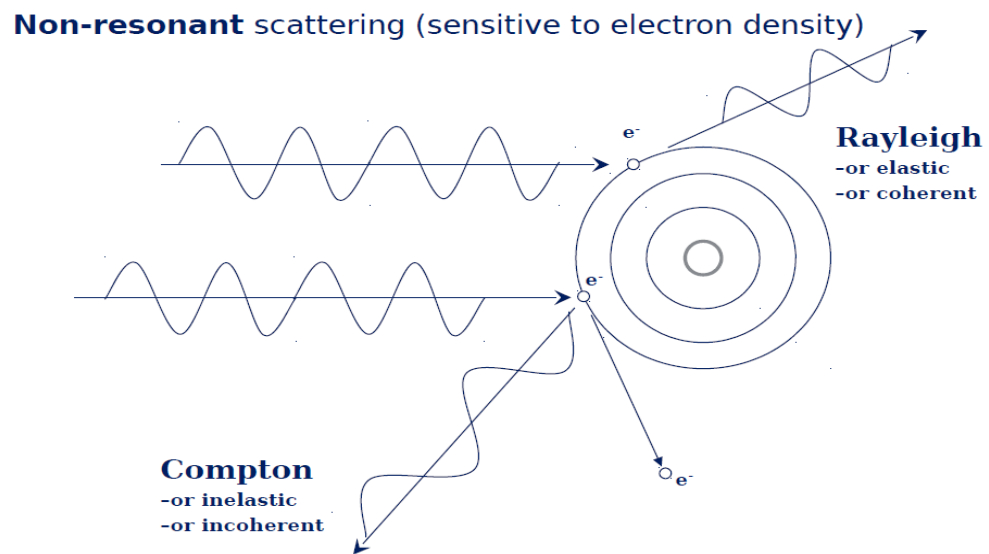


Figure 1.17: Elastic scattering depiction

SAXS probes angles of around 0.1 to 10° , which then allows systems up to approximately 150 nm to be studied and a variety of information can be obtained (Figure 1.18).

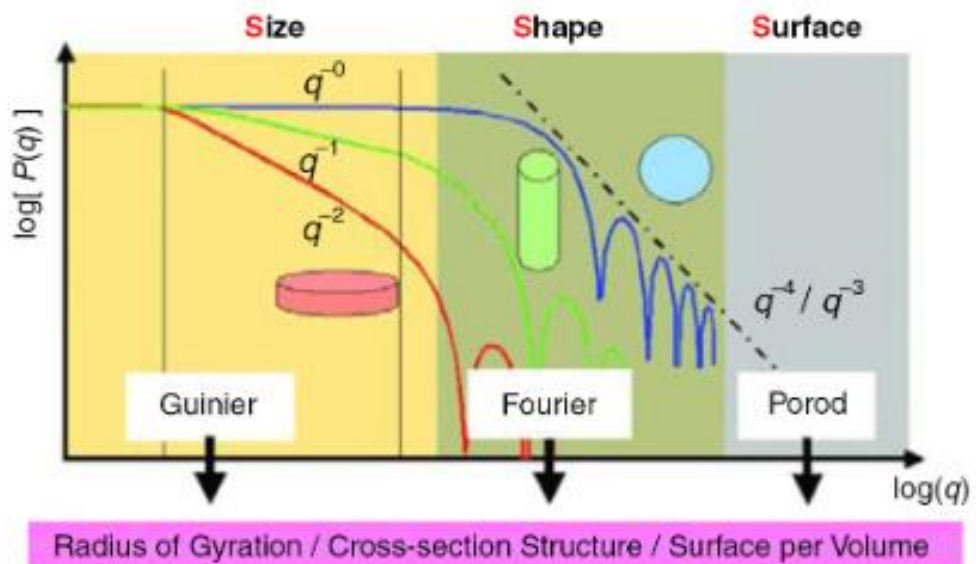


Figure 1.18: Typical SAXS scattering profile and data that can be extracted (where q is the scattering vector and P the form factor)⁷⁵

Figure 1.18 shows the typical scattering profile obtained from a SAXS experiment. We can see that it is split into several different regions which give us different information on the system. The first region, which is at a low scattering vector (Q), is the Guinier region. The first work involving SAXS occurred in the 1930s when Andre Guinier developed the first recognised SAXS camera, known as the Guinier camera. Using this new technique, he was able to study metal alloys containing aluminium and copper and found the presence of diffuse scattering features which he interpreted as copper platelets. This was then confirmed 58 years later with the use of transmission electron microscopy (TEM). At this time Guinier also developed the so-called Guinier law which relates the decrease in intensity to the radius of gyration (R_g). This is still one of the most commonly used data analysis tools in the field of SAXS (see Figure 1.19).^{83,84,85}

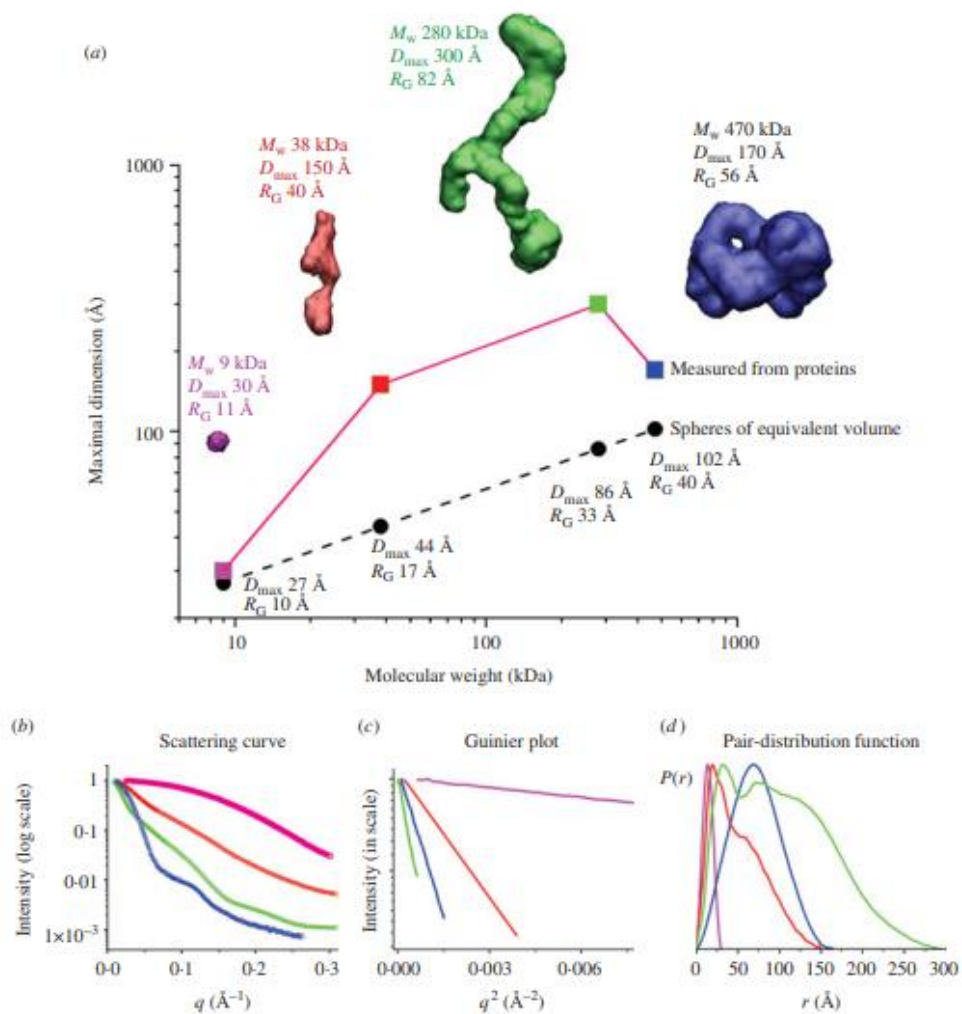


Figure 1.19: a) Molecular weight from various shaped proteins b) scattering curves demonstrating the intensity as a function of size c) guinier plots showing calculation of radius of gyration in aggregated and non-aggregated systems d) pair distribution function for both aggregated and non-aggregated systems⁸⁶

Moving to a higher Q value enters into the Porod region, which can be used as a means of gathering information on surface properties such as surface-to-volume ratio and interactions at the surface interface. The WAXS region follows at higher Q which provides information on lower-size systems, typically less than 1 nm. In between the Porod and Guinier regions is the Kratky region, this section of the

profile is used in biological studies and can provide information on the folding of a protein (Figure 1.20).

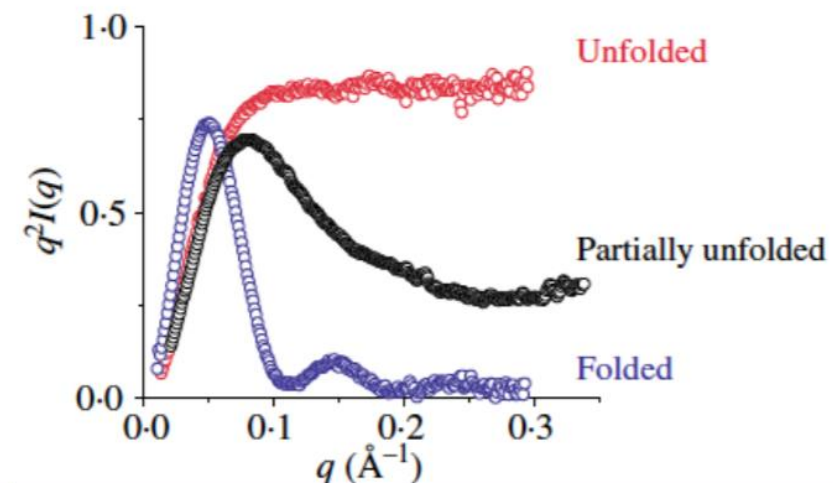


Figure 1.20: Example Kratky plot for determining folding behaviour of proteins in solution⁸⁶

One of the most prominent fields where SAXS has found use is the study of biological systems within solutions.^{86,87,88} As XRPD experiments require crystallisation for analysis, SAXS began to be looked at as potentially a tool to study biological macromolecules in solution without the need for a crystal. This allowed scientists to determine the size and mass of proteins as well as the folding and unfolding.

Porous materials are used in a range of industries such as catalysis and drug delivery, where high surface areas allow for greater interactions. SAXS can be used as a means of studying mesoporous materials where the pores range in size from approximately 2 to 50 nm. Using SAXS details such as pore size, distribution and spacing between pores can be determined.⁹⁰

Protein crystallisation is an interesting area of research due to several potential applications, for instance, the separation and purification of proteins from solution. SAXS can detect aggregation within the protein structure during crystallisation, this allows conditions to be optimised at an early stage of the process development.^{91,92}

1.5.1.1 SAXS Pharmaceutical / Amorphous Applications

SAXS has found limited application in studying amorphous pharmaceuticals, however, recently work has begun to be published showing the potential to use SAXS in conjunction with WAXS as a tool for studying amorphous systems.

There is interest in studying the disorder within amorphous pharmaceuticals regarding the processing method chosen and what disorder this may cause, and also changes which may occur within the system as a result of storage conditions. Being able to simultaneously gather WAXS data allows for fingerprinting of the crystalline phase in materials which may have been produced during production or storage. Using SAXS differences observed at low Q values can begin to show the presence of differing amorphous nanostructures. This has been used to determine differences between process conditions such as API milled alone or co-milled with a polymeric excipient. Comparison with crystalline material can be used as an indicator of what structural features may or may not remain present after amorphisation has occurred. Particularly useful in samples with no measurable crystallinity from powder diffraction experiments, the SAXS signal obtained can vary greatly showing density fluctuations at the nanoscale.⁹³

SAXS can also be used qualitatively for the analysis of polyethylene glycol (PEG) containing ASD systems, due to the ability of SAXS to analyse lamellar phases.

Obtainable from the scattering vector (q) value the long period (L) of the lamellar region can be calculated for a given molecular weight of PEG, by,

$$L = \frac{2n\pi}{q} \quad \text{Eqn 1.4}$$

Studying changes in this structural feature via SAXS can inform on the location of API within the polymer matrix. Comparison of PEG peaks within the SAXS region can begin to show increases in the long period as a consequence of API being included, this begins to indicate that API molecules are contained within the PEG structure. Simultaneous WAXS measurements allow for crystallisation identification as complementary information to the SAXS data, with decreases in L accompanied by crystallisation of the drug. This therefore suggests the amorphous drug to be incorporated within the lamellar structure while the crystalline drug is excluded. Using this information may help in predicting which API may form a more stable dispersion with PEG as APIs that interacted with the lamellar phase stayed amorphous for longer than those that did not.^{94,95}

1.5.2 X-Ray Powder Diffraction / Wide Angle X-Ray Scattering

XRPD is an analytical technique which is primarily used as a means of structural analysis for organic and inorganic molecules. The diffraction occurs due to constructive interference between monochromatic X-rays which have been reflected from repeating planes within the lattice. This phenomenon can be described by Bragg's Law (see Figure 1.21), this law relates the wavelength of the X-ray source to the angle of diffraction to inform on the lattice dimensions within a sample. When Bragg's law is met, peaks are observed at differing angles (Θ) which can then be related to the d-spacing (\AA) which occurs between planes within the crystal lattice. This relationship results in Bragg's equation which is shown in

Eqn 1.5, where n is the diffraction order, λ the wavelength, d the distance between layers of atoms and Θ the angle of diffraction.

$$n\lambda = 2d \sin \Theta \quad \text{Eqn 1.5}$$

To obtain distances from within the crystal lattice the wavelength used needs to be similar to the distance within the crystal, the most common source for this is copper with a wavelength of 1.541 \AA . In three dimensions the planes within a crystal lattice are described by Miller indices (hkl) , which are used to identify how the plane intersects with the axes of the crystal.

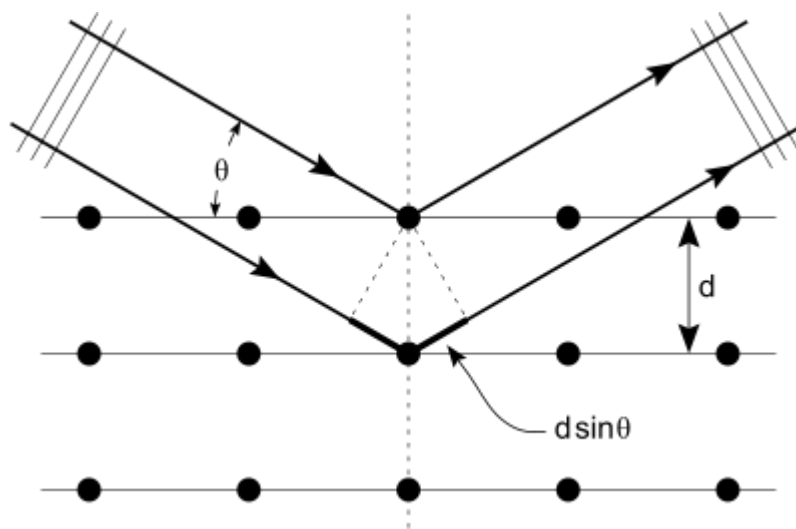


Figure 1.21: Braggs law diagram

This produces a regular pattern of reflections (spots) which correspond to the distance within the reciprocal lattice, from this the real spacing of the lattice can be calculated. This is usually represented with the Ewald sphere (Figure 1.22), where the scattering vector S_0 is equal to a scattered wave vector S . This places a crystal at the centre of a sphere where the scattering vector passes through and contacts the surface of the sphere. This corresponds with a lattice position of $0,0,0$ which relates to the origin of reciprocal space. To meet the Bragg condition,

the scattered wave vector must overlay the surface of the sphere to allow constructive interference and reflection to be observed. To allow for all of the lattice points to be determined the crystal requires to be rotated which allows the capture of as many points as possible.

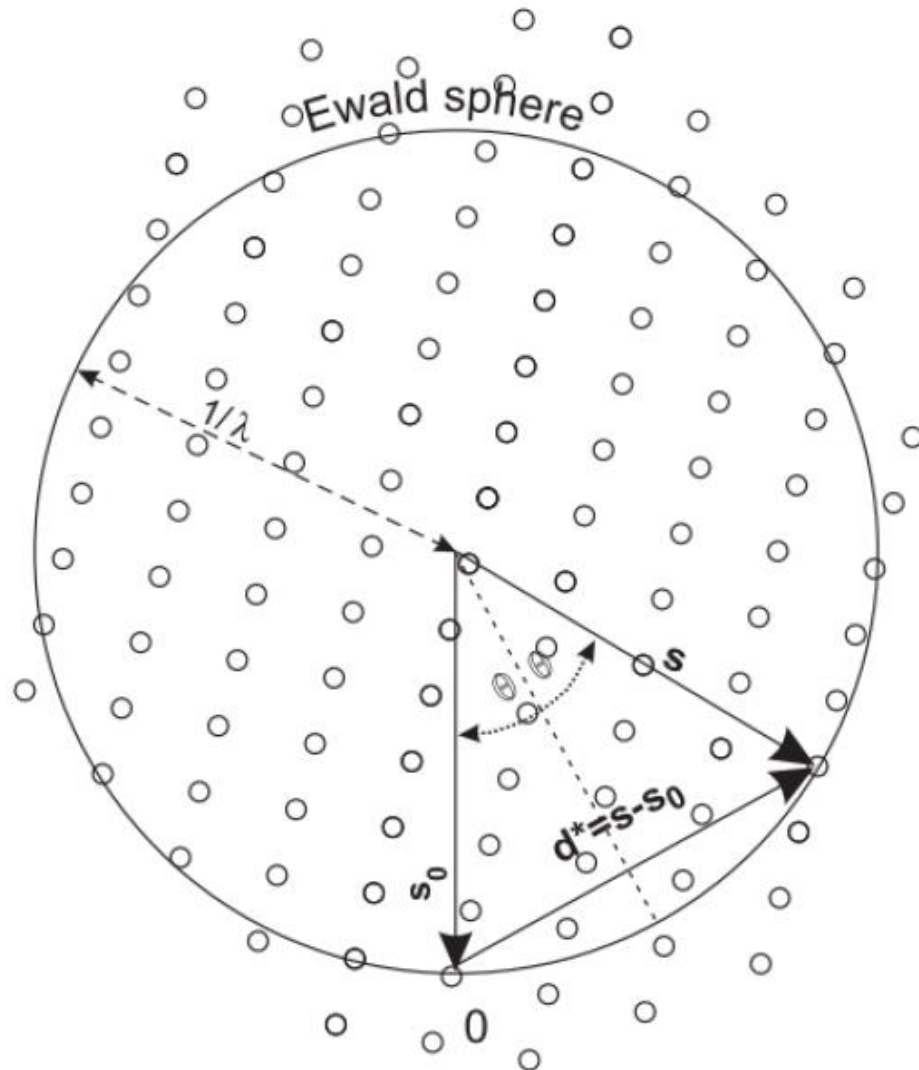


Figure 1.22: Ewald sphere with 0 as the origin of reciprocal space

For lattice points which do not intersect with the surface, and therefore do not satisfy Bragg's law the incident wavelength can be altered to a lower wavelength to give access to smaller d-spacings.

Utilising the relationship between the reciprocal lattice and real space the information gathered from the reflected intensities can be used to obtain information on the crystal lattice and the unit cell. The diffraction pattern observed is the Fourier transform of the crystals electron density which can be defined with a structure factor F_{hkl} , at each reciprocal lattice point hkl as shown in Eqn 1.6.

$$F_{hkl} = \int_{cell} \rho(xyz) \cdot e^{[2\pi i(hx+ky+lz)]} dV \quad \text{Eqn 1.6}$$

Where $\rho(xyz)$ is the electron density of the system and $(hx + ky + lz)$ are 3-dimensional coordinates of a specific atom on a given plane. To obtain a diffraction pattern an inverse Fourier transform of the electron density can be performed as shown in Eqn 1.7.

$$\rho(xyz) = \frac{1}{V} \sum_{h,k,l} F_{hkl} \cdot e^{[2\pi i(hx+ky+lz)]} \quad \text{Eqn 1.7}$$

Where V is the volume of the unit cell. This equation results in the “Phase Problem” as the intensities can be measured directly by integration of the reflections, but any information about the phase is lost. Due to this, it is not possible to perform an inverse Fourier transform as shown in Eqn 1.7.

1.5.3 Thermal Analysis

Both differential scanning calorimetry (DSC) and thermogravimetric analysis (TGA) were used for studying phase separation and water uptake in amorphous materials in Chapter 5.

1.5.3.1 Differential Scanning Calorimetry

DSC is used as an analysis technique for studying new materials and mixed-phase materials. During an experiment, a temperature profile is applied to a

sample which allows for the identification of phase transitions, melting points and solid-to-solid transitions within the material to be studied.⁹⁶ With the use of an empty reference pan, the difference in the input energy to maintain the same temperature as the sample pan is recorded to determine the thermal behaviour of the sample. This gives insight into any endothermic or exothermic transitions taking place and allows the kinetics and thermodynamics of the transitions to be studied.

When analysing amorphous pharmaceuticals using DSC the level of residual crystallinity can be calculated and also information on the stability of the amorphous phase can be determined. The stability of the amorphous phase can be informed through the presence of an exothermic event in the DSC that relates to the recrystallisation of the amorphous phase, demonstrating the material is not stable against crystallisation. The T_g can also be determined through DSC analysis and is observed as a small dip in the baseline. At this temperature the material has increased molecular mobility, which allows the amorphous molecules to change from a glassy state to a rubbery state.⁹⁷

1.5.3.2 Thermogravimetric Analysis

TGA analysis works in the same way as DSC in that the sample is taken through a temperature profile and a comparison with an empty reference pan is used to inform on the sample. The difference in comparison to DSC is that the information available now relates to mass loss within the system. In the context of amorphous pharmaceuticals increasing mass loss can be an indication of amorphous content as the lattice can take water on more easily.⁹⁷

1.5.4 Spectroscopic Analysis

Fourier transform infrared spectroscopy (FTIR) was used for the analysis of amorphous materials in Chapter 5, while terahertz (THz) Raman spectroscopy was utilised for the analysis of ASD samples in Chapter 4.

1.5.4.1 Fourier Transform Infrared Spectroscopy

FTIR identifies chemical bonds within a molecule by passing IR radiation through a sample and measuring the transmitted signal which is not absorbed by the sample. The transmitted signal contains frequencies that are characteristic of functional groups within the molecule and the stretching and vibrations of individual bonds.

Changes in intermolecular interactions occurring when a sample moves from crystalline to amorphous can be studied with the use of FTIR. Peak broadening observed in spectra of amorphous samples can be explained by a loss of hydrogen bonding within the molecule.⁹⁸

1.5.4.2 Terahertz Raman Spectroscopy

Raman spectroscopy is often used as a complementary technique to FTIR. When the incident radiation interacts with the sample a photon at a specific frequency can induce excitation of the electric state from the ground state to a higher energy state. This phenomenon is known as the Raman effect and occurs as a result of inelastic scattering. During a Raman experiment both elastic (Rayleigh) and inelastic (Raman) scattering take place. The required Raman scattering can then be categorised as either Stokes or anti-Stokes. Stokes is when the difference in energy is a result of a loss in energy, while anti-stokes is from a gain in energy.

The anti-stokes measurements are the important ones for Raman spectroscopy due to the higher intensity in comparison to stokes.

THz Raman is used for characterising structures and interactions of compounds in the low wavenumber range (less than 100 cm^{-1}), specifically on intra and intermolecular interactions. At THz frequencies, crystalline compounds exhibit unique fingerprint spectra which can help to determine the solid form of the molecule,⁹⁹ whereas amorphous materials produce largely featureless spectra.¹⁰⁰ The contrast between the spectra produced from crystalline and amorphous materials allows THz Raman to be used as a means of identifying the crystallisation of amorphous pharmaceuticals.¹⁰¹

1.6 Manufacturing Techniques

There are several options available when it comes to manufacturing an ASD. The techniques available can be broadly split into two categories, solvent evaporation and melting processes. The work in Chapter 4 utilised hot melt extrusion (HME). Ball milling was employed in Chapter 5 to produce amorphous samples from a bulk crystalline starting material.

1.6.1 Hot Melt Extrusion

Falling into the melting processes, hot melt extrusion (HME) is commonly used throughout various industries including pharmaceutical where it can be used for the amorphisation of APIs. Many processes are involved in an HME experiment, firstly the material is fed through a feeder into the barrel of the extruder, at this stage the material is subjected to heating and mixing in the form of a twin rotating screw. The screw allows the material to pass through the barrel and forces it

through a die situated at the end of the barrel which is where the extruded material is collected (see Figure 1.23).

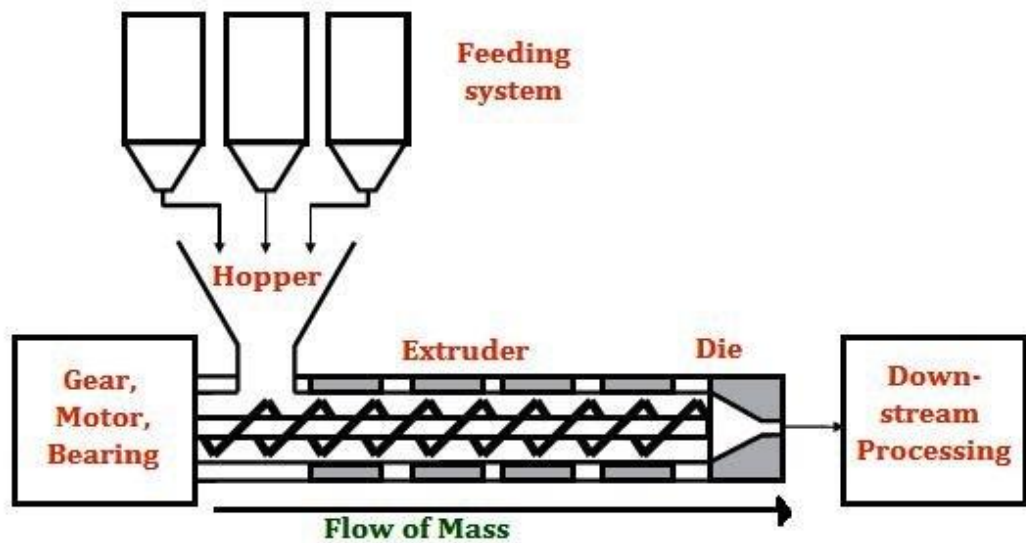


Figure 1.23: Schematic diagram of hot melt extruder¹⁰²

Polymers are critical in the manufacture of ASDs but in HME they are also necessary for the processing. The drug is solubilised or dispersed within the molten polymer during the HME process. Several key properties of the polymer must be known to enable the use of the polymer in the manufacture of an ASD¹⁰³:

- Melting point and T_g
- Molecular weight
- Particulate properties of the polymer
- Interactions between the polymer and compound of interest

1.6.2 Ball Milling

Ball milling is a high-energy process commonly used as a means of particle size reduction. This is achieved by both shear and impact stresses acting on the

material during the milling experiment. Milling of a bulk crystalline material can also cause the crystal structure to be completely broken resulting in the formation of an amorphous form of the compound.

There are two routes to amorphisation during a milling process, firstly the creation of crystal defects which eventually cause the crystal to lose all long-range order. Or there can be a melt quench process due to the temperature within the milling jar caused due to the frequency of milling.¹⁰⁴

Chapter 2: Aims and Objectives

2.1 Aims

The overall aim of this thesis was to explore the application of X-ray techniques for the analysis of pharmaceuticals and other organic molecular systems. Specifically, the work addresses three main aims, namely to:

- 1) Develop an in-situ experimental set-up using WAXS to monitor phase changes associated with ASDs upon exposure to dissolution media (Chapter 4)
- 2) Investigate the application of SAXS in combination with other techniques as a characterisation tool for amorphous small organic molecules (Chapter 5)
- 3) Optimise a 2D WAXS method for the characterisation of cellulose fibres and films to investigate the crystallinity and orientation index of colloidal samples pretreated with different shear forces (Chapter 6)

2.2 Objectives

Aim 1 was achieved by the following:

- a) Designing and testing a sample stage to allow for in-situ crystallisation monitoring
- b) Assessing the effect of processing temperature and drug loading on ASD stability

Aim 2 was achieved by the following:

- a) Preparing a range of powdered samples of an API provided by GlaxoSmithKline (GSK) with varying amorphous content from crystalline to fully amorphous for SAXS analysis
- b) Investigating all samples with a suite of analytical techniques to provide characterisation measurements to compare against SAXS measurements

- c) Analysing all available data to assess the extent, amount and disposition of amorphous content in the milled samples to contrast with SAXS data

Aim 3 was achieved by the following:

- a) Adapting a WAXS method to be used for the analysis of cellulose fibres and films
- b) Comparing Segals' method and deconvolution method for calculating crystallinity for the samples characterised in this chapter
- c) Investigating the crystallinity and orientation results for fibres vs films, stretched vs non-stretched fibres and lab-scale vs batch-scale samples to explore the effect of process history on the structure at the nanoscale

Chapter 3: Materials and Methods

3.1 Materials

Paracetamol was purchased from Mallinckrodt Inc (CAS 103-90-2). Hydroxypropyl methylcellulose (HPMC) grade Affinisol™ 15LV was donated by the Dow Chemical Company (CAS 9004-65-3). The chemical structures of both are shown in Figure 3.1. A Millipore *Milli-Q* water system equipped with 0.22 µm filters was used to provide deionised water.

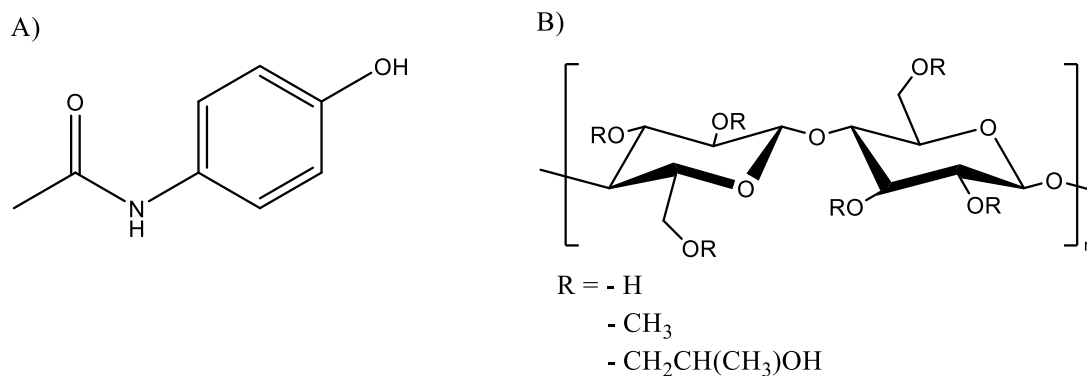


Figure 3.1: Chemical structure of A) Paracetamol and B) Affinisol™ 15LV where n denotes the structural unit for Affinisol™

GSK2838232M was supplied by GSK. Sodium alginate made from brown algae was purchased from Sigma Aldrich (CAS 9005-38-3), MFC and NFC cellulose fibres and films, sodium alginate and calcium alginate films were all supplied by colleagues in Chemical and Process Engineering (CPE), University of Strathclyde.

3.2 Methods

3.2.1 Manufacturing Methods

3.2.1.1 Hot Melt Extrusion

ASD samples of paracetamol and Affinol™ were extruded with a Thermo Scientific Process 11 twin screw extruder equipped with a Brabender Mini Twin (MT-S) Loss in Weight (LIW) feeder operated in gravimetric feeding mode. Samples were prepared for extrusion by first weighing out the Affinol™ and paracetamol to the correct weight for the composition of ASD required. The weighed powders were then combined in a Pharmatech AB-015 bin blender and blended for 20 minutes with a blend speed of 15 RPM and agitator speed of 75 RPM. Once blended and a homogenous powder was produced the samples were loaded into the HME and extruded at a range of temperatures (130, 150 and 170°C) with a feed rate of 0.1 Kg/hr and a screw speed of 100 rpm.

3.2.1.2 Ball milling

250 mg of GSK2838232M were placed in a 5 mL steel ball mill jar along with either one or two 7 mm steel balls. Milling was performed for between 5 and 60 minutes at a milling frequency of 25 or 30 Hz. Details of specific milling times, milling frequency and the number of milling balls used can be found in section 5.2.1. Milling was conducted using a Retsch MM400 ball mill.

3.2.2 Analytical Techniques

3.2.2.1 Small Angle X-Ray Scattering (SAXS)

SAXS data were acquired using a Xenocs Xeuss 2.0 SAXS/WAXS laboratory beamline equipped with a Genix 3D microsource Cu K α 1 $\lambda=1.541\text{\AA}$ and Pilatus 1M area detector. Powdered samples obtained via ball milling were sandwiched between two sticky Kapton dots to hold them in place and mounted in a transmission sample holder. Data workup and analysis were performed using Foxtrot software version 3.4.9, where background corrections and image masking were performed. Porod invariant data analysis was performed using SasView version 5.0.

3.2.2.2 Wide Angle X-Ray Scattering (WAXS)

WAXS data were acquired using a Xenocs Xeuss 2.0 SAXS/WAXS laboratory beamline equipped with a Genix 3D microsource Cu K α 1 $\lambda=1.541\text{\AA}$ and Pilatus 1M area detector. ASD extruded samples were loaded into a custom 3D printed sample holder, water was added via a syringe to induce crystallisation. Cellulose fibre and film samples were glued to metal washers and mounted in a transmission sample holder. Data collection parameters varied between sample types. Foxtrot software version 3.4.9 was used to conduct background subtraction and image masking before processing the data into 1D diffractograms.

3.2.2.3 X-Ray Powder Diffraction (XRPD)

All extrudate and physical mixture samples were analysed using XRPD. Sample extrudate was placed into a sample holder with no further treatment. Powdered physical mixture samples were placed into a sample holder and smoothed with a

glass slide to prevent any preferred orientation effects. Samples were analysed using Bragg-Brentano reflection XRPD on a Bruker D8 Discover Diffractometer equipped with Θ/Θ geometry, Ni filtered $K_{\alpha 1,2}$ Cu radiation, $\lambda = 1.540596 \text{ \AA}$, a LynxEye 1D position sensitive detector and an automated 9 position flip-stick multi-sample holder.

All ball-milled samples analysed by XRPD were ground before loading into 0.7 mm borosilicate capillaries. Capillaries were continuously rotated during data collection to ensure good powder averaging. Samples were analysed by Debye-Scherrer transmission using a Bruker D8 Advance II capillary diffractometer equipped with Θ/Θ geometry, primary monochromated radiation (Cu $K_{\alpha 1}$, $\lambda = 1.540596 \text{ \AA}$), a LynxEye 1D position sensitive detector and a rotating capillary sample stage.

Variable temperature XRPD was collected using a Bruker D8 Advance capillary diffractometer in transmission geometry, equipped with Θ/Θ geometry, primary monochromated radiation (Cu $K_{\alpha 1}$, $\lambda = 1.540596 \text{ \AA}$), a LynxEye 1D position sensitive detector and a rotating capillary sample stage. An Oxford Cryosystems Cryostream was used to control the temperature of the sample before data collection.

All XRD patterns were analysed using Diffrac EVA version 4.2. The crystallinity of cellulose samples was performed using a deconvolution analysis method within the software. Data evaluation and visualisation of ASDs and ball-milled samples was conducted to monitor the amorphous and crystalline content.

3.2.2.4 Differential Scanning Calorimetry (DSC)

DSC measurements were carried out in a Netzsch DSC214 Polyma differential scanning calorimeter. 3-5 mg of ball milled sample was weighed out and placed into an aluminium pan with a pierced lid for analysis. The thermal analysis was carried out with Netzsch Proteus Analysis software version 80. The analysis provided the temperature of endothermic and exothermic events to be used to calculate % crystallinity.

3.2.2.5 Thermogravimetric Analysis (TGA)

TGA analysis was carried out using a Netzsch STA449 F1 Jupiter. 3-5 mg of ball milled sample was weighed out and placed into an aluminium pan with a pierced lid for analysis. The thermal analysis was carried out using Netzsch Proteus Analysis software version 80. The analysis provided data on mass loss as a function of increasing amorphous content within samples.

3.2.2.6 Fourier Transform InfraRed Spectroscopy (FTIR)

Attenuated total reflectance (ATR) FTIR spectra were collected using a Bruker Tensor II IR spectrophotometer equipped with a diode laser, KBr beamsplitter and a Digitech detector. Powdered samples were placed directly on an ATR accessory, this allowed analysis of powdered samples with no further preparation. A background scan was subtracted from all spectra to remove instrumentation background effects and reduce noise in the baseline, this was performed in Bruker OPUS software. Data analysis of peak assignment and spectra stacking for comparison was performed using Spectragryph software version 1.2.

3.2.2.7 Scanning Electron Microscopy (SEM)

Powdered samples were mounted to aluminium stubs and sputtered with a 20 nm layer of gold. Images were captured in backscattered mode with a beam voltage of 10 kV. Data were acquired using a Hitachi TM4000 SEM plus and images were produced at a magnification of 1.0 k to allow for visual data analysis of the sample morphology.

3.2.2.8 Terahertz (THz) Raman

THz Raman analysis was carried out using an Ondax THz Raman Spectroscopy System equipped with a 785 nm laser. Data analysis was performed using Spectragryph software version 1.2.

Chapter 4: Physical Stability of Amorphous Solid Dispersions

4.1 Introduction

Modern drug discovery techniques, such as combinatorial chemistry and high throughput screening, have led to an increase in poorly soluble drug candidates, often leading to low oral bioavailability and other issues in the development pipeline.^{105,106,107} Many of these new drug candidates are larger molecules with higher molecular weights and lipophilicities that result in poorer solubility.^{107,108,109} Some formulation strategies can be employed to increase the solubility and dissolution performance of such compounds. A popular approach for improving oral bioavailability is the use of ASDs which have higher solubilities than their crystalline counterparts.^{111,112,113} However, the amorphous form of a drug has higher energy and thus reduced thermodynamic stability than the crystalline form. The higher energy of the amorphous form can cause it to be thermodynamically unstable with a tendency to recrystallise.^{114,115} This undesirable transformation can take place during processing,¹¹⁶ dissolution¹¹⁷ and storage.¹¹⁸

The solubility advantage from using the amorphous form gives a maximum increase in solubility known as amorphous solubility.^{46,119,120} During dissolution, the solution can become supersaturated and, in doing so, allows for nucleation and crystallisation of the drug to occur.^{121,122} The crystallisation process that then occurs will vary based on the compound being studied and if stabilising excipients are present. Polymers are commonly used to prevent nucleation and crystal growth from the supersaturated solution created during dissolution.^{123,124}

This study examines the use of WAXS to study the phase behaviour of paracetamol-containing dispersions during dissolution studies. Paracetamol has been involved in many studies showing the improvement of dissolution performance when used as an ASD. Phase transformations were monitored through the use of a novel WAXS setup and THz Raman. The time required for

the onset of crystallisation was monitored as a function of drug loading and HME processing temperature using both X-Ray and THz Raman. Lower drug loading and higher processing temperatures were found to increase the stability of the amorphous form, with no crystallisation observed below the critical concentration.¹²⁵

Paracetamol is an API in the class of analgesics and is used in the treatment of pain and fever. Paracetamol can be found in class III of the BCS classification system owing to its solubility of approximately 23.7 mg/ml in water at body temperature.^{126,127} A widely studied compound, paracetamol is known to exist in a variety of solid forms including solvates/hydrates, co-crystals, salts and three polymorphic forms I, II and III.¹²⁸ Form I packs in a herringbone motif and is the most stable form while forms II and III are metastable and exist in a layered structure.

Polymer selection in ASD technologies is of vital importance to the overall stability of the product as well as being used in the extrusion process to allow the drug to solubilise within the polymer. There are several chemical-physical properties of the polymer which need to be considered when choosing a suitable candidate for formulation. Properties of importance are glass transition temperature (T_g), thermal stability, ability to stabilise amorphous drugs and how well the polymer can dissolve an API. All of these properties play a role in the amount of stabilisation offered to the amorphous API when solubilised in a polymer. The stabilisation of the API results from the reduced molecular mobility of the API and the formation of polymer-API interactions. These interactions come in the form of intermolecular interactions such as hydrogen bonding, electrostatic interactions, ionic forces and π - π interactions. These interactions between polymer and API

reduce the tendency of the API to form the API-API interactions that can lead to the recrystallisation of the amorphous form.

In this chapter, we examined the recrystallisation tendencies of ASDs containing paracetamol and the polymer, Affinisol™. Percent drug loading and extrusion temperatures are hypothesised to affect whether or not paracetamol crystallises upon dissolution.¹²⁵ Specifically, if drug loading is too high (above approximately 20%), undesirable crystallisation of paracetamol is expected to occur.¹²⁵ The work in this chapter aims to improve future drug development in the area of amorphous compounds by establishing a method by which to probe these parameters and operational windows for these parameters when producing stable ASDs of paracetamol.

4.2 Experimental

4.2.1 Hot Melt Extrusion

All amorphous paracetamol dispersions were extruded using a Thermo Scientific Process 11 twin screw extruder coupled with a Brabender Technologie mini twin feeder (section 2.2.2.1). Before extrusion, materials were weighed, and mixtures were sieved and then blended using a Pharmactech AB-015 bin blender to ensure a homogenous mixture before extrusion. The blender parameters used can be found in Table 4.1. Extruder parameters can be found in Table 4.2.

Table 4.1: Bin blender parameter settings for mixing of physical mixtures prior to hot melt extrusion

Blender Parameter	Value
Blend Speed	15 RPM
Agitator Speed	75 RPM
Blend Time	20 minutes
Agitator Time	20 minutes

Table 4.2: Hot melt extrusion parameters for manufacturing of ASDss

API-Polymer (wt%)	HME Processing temperature (°C)	Feed Rate (kg/hr)	Screw Speed (rpm)
10:90	130, 150 and 170°C	0.100	100
20:80	130, 150 and 170°C	0.100	100
25:75	130, 150 and 170°C	0.100	100
27.5:72.5	130, 150 and 170°C	0.100	100

4.2.1.1 X-ray Powder Diffraction

Extruded dispersions were characterised offline using a Bruker D8 Advance II transmission flat plate diffractometer as outlined in section 3.2.2.3. Samples were analysed to confirm amorphicity (over a two-theta range of 3-35°, with a step size of 0.017° and 1 second per step).

4.2.1.2 Wide Angle X-ray Scattering

WAXS data was collected on a Xenocs Xeuss 2.0 SAXS/WAXS laboratory beamline as described in section 3.2.2.2. Instrument setup details are outlined in Table 4.3.

Table 4.3: WAXS instrument collection parameters used for dissolution studies

Collection Parameter	Value
Collection time	6 hours (Multiple 60 s images)
Sample to detector distance	171 mm
Collimation setting	High Flux (1.2 x 1.2 mm)
Source	Copper ($\lambda = 1.541 \text{ \AA}^{-1}$)

A transparent 3D-printed sample holder (Figure 4.1) was designed to allow for bespoke dissolution experiments to be carried out on the instrument. This sample holder was then mounted in a metal sample stage to allow alignment of the beam to the sample.

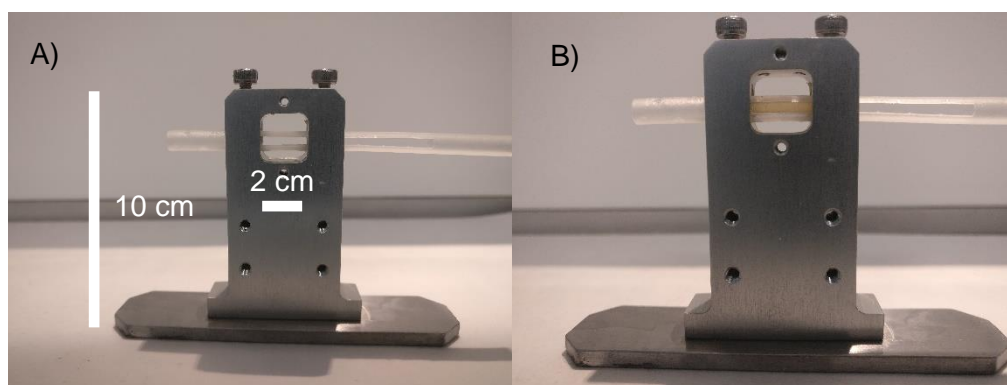


Figure 4.1: A) the transparent 3D-printed sample holder held in place with metal sample stage B) the transparent 3D-printed sample holder with extruded sample

4.2.1.3 Terahertz Raman

THz Raman data were collected with an Ondax-Raman PhAT probe equipped with a 785 nm laser source and connected to an RXN1 spectrograph unit as described in section 3.2.2.8.

4.3 Results and Discussion

In this chapter, we show that XRPD analysis can be used to determine the compositions of amorphous paracetamol/Affinisol™ extrudates in which crystallisation will not occur.

4.3.1 Raw materials and dry extrudate analysis

Reference XRPD patterns for raw materials were collected for comparison with patterns later obtained for formulated samples. The data for reference materials (Figure 4.2) showed a characteristic amorphous halo for Affinisol™ with a peak at approximately 34° two theta corresponding to sodium chloride impurity in the material. The XRPD pattern for paracetamol form I corresponded to XRPD patterns published in the literature.^{129,130}

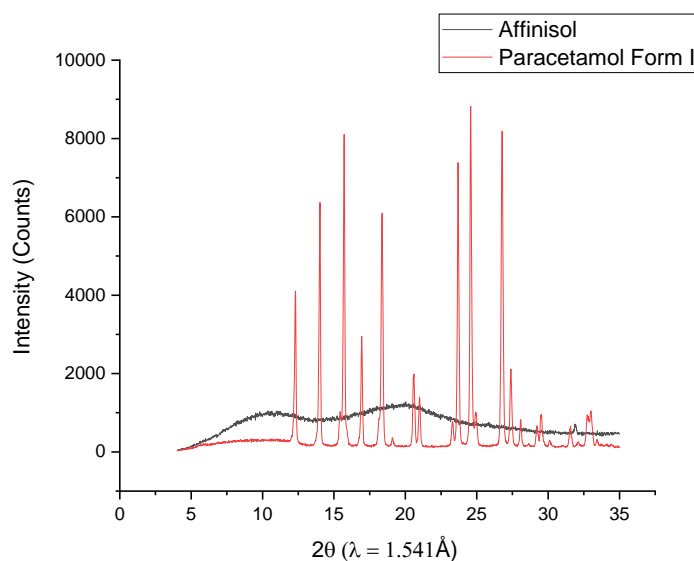


Figure 4.2: XRPD reference patterns for Affinisol™ (black line) and paracetamol form I (red line)

Hot melt extrusion was used to produce amorphous dispersions of paracetamol and Affinisol™ at varying compositions produced at a processing temperature of between 110-170°C, as shown by XRPD (Figure 4.3).

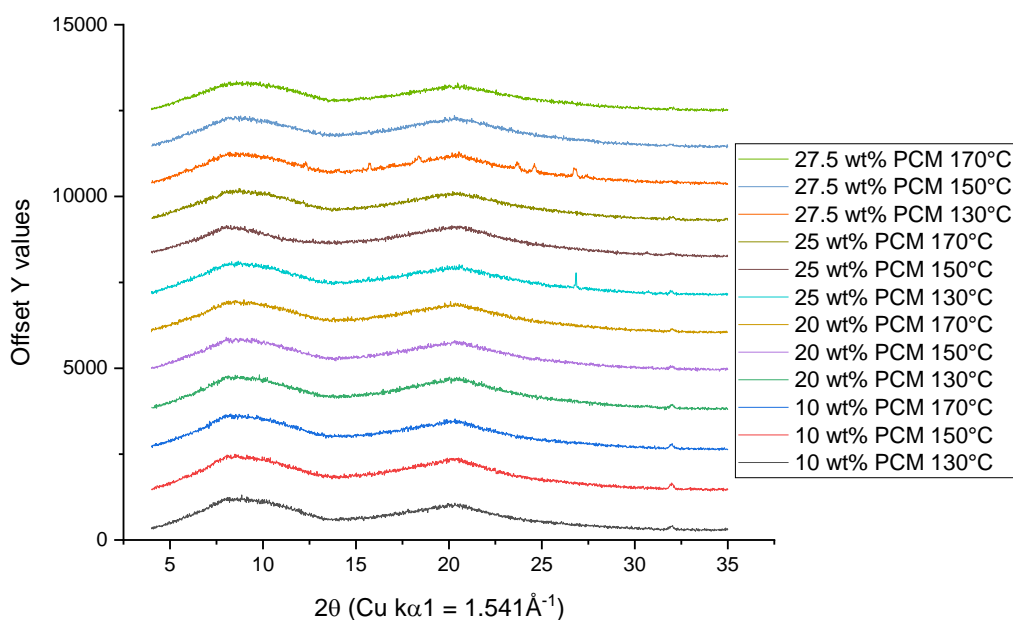


Figure 4.3: XRPD patterns for paracetamol Affinisol™ ASDs produced at varying compositions at three different processing temperatures

The XRPD data in Figure 4.3 shows the characteristic amorphous halos which are expected for amorphous samples. The peaks appearing at approximately 34° two theta most likely result from the sodium chloride impurity within the Affinisol™ raw material. As evidenced by the presence of additional sharp peaks in the XRPD patterns, both the 25 and 27.5 wt% paracetamol compositions extruded at 130°C contained crystalline material and weren't fully amorphous after extrusion due to the processing temperature being lower than the critical temperature for those compositions.

4.3.2 Analysis of Formulated Samples

4.3.2.1 Reference Terahertz Raman Spectra of Amorphous and Crystalline Paracetamol in the Presence of Affinisol™

THz Raman spectroscopy was used to establish if the paracetamol in the extrudate samples would crystallise in water. THz Raman spectroscopy was performed on a high drug loading sample (50 wt%) which was extruded at 155°C. The THz Raman spectra for paracetamol in both amorphous and crystalline forms in the presence of Affinisol™ are shown in Figure 4.4. From these spectra, we can see that there are three distinct peaks associated with crystalline paracetamol appearing at approximately 32, 56 and 89 cm^{-1} . These peaks are characteristic of form I paracetamol.¹³¹

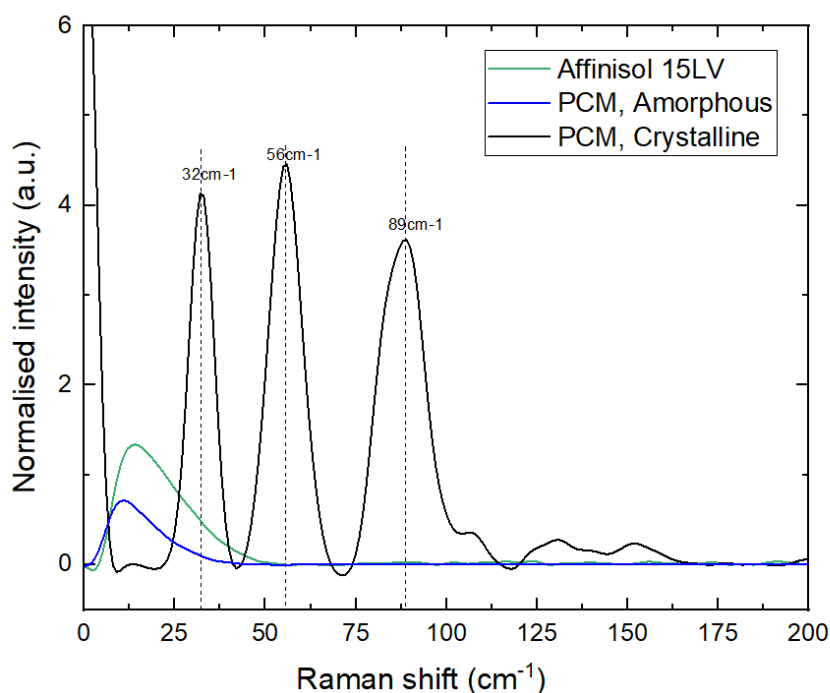


Figure 4.4: THz Raman spectra for amorphous paracetamol (blue), crystalline paracetamol (black) and Affinisol™ (green)

A bundle of 50 wt% paracetamol extrudate was placed in a plastic petri dish and deionised water was introduced until the whole sample was immersed. The deionised water was introduced to probe what happens in the early stages of dissolution experiments. THz Raman spectra were continuously collected for the sample in the petri dish until crystallisation was observed. Paracetamol crystallisation was observed approximately three to four minutes after the introduction of water. This change was indicated by the emergence of the three peaks associated with crystalline paracetamol (see Figure 4.5).

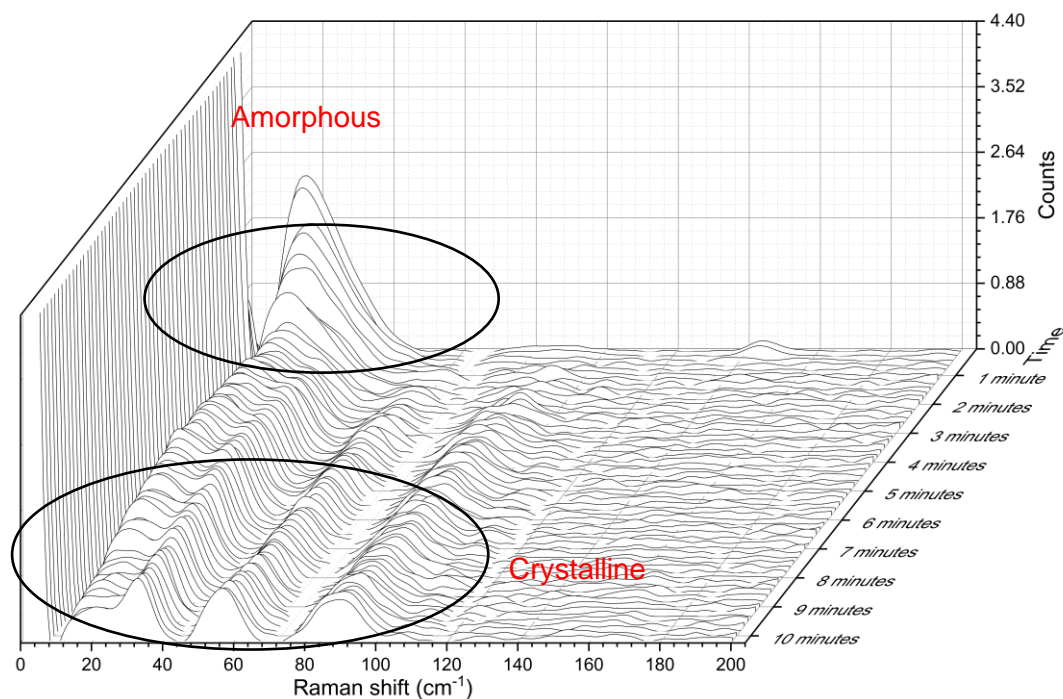


Figure 4.5: THz Raman spectral evolution of 50 wt% paracetamol extrudate immersed in deionised water

The crystallisation of the material was also indicated by a change in the colour of the extrudate (Figure 4.6). Prior to the introduction of water, the extrudate was a clear and colourless extrudate; the appearance of the extrudate changed to a white opaque material as the paracetamol crystallised inside the extrudate. This colour change and the appearance of peaks are used throughout this chapter as indications of crystallinity.

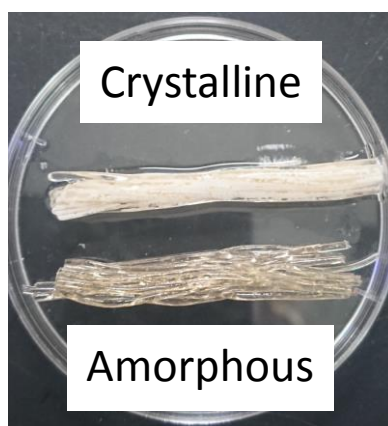


Figure 4.6: 50 wt% extrudate before and after being immersed in water

4.3.2.2 Analysis of 10 wt% Paracetamol ASD Formulation

X-ray diffraction was performed on all 10 wt% paracetamol samples, as well as a 10 wt% physical mixture, as shown in Figure 4.7.

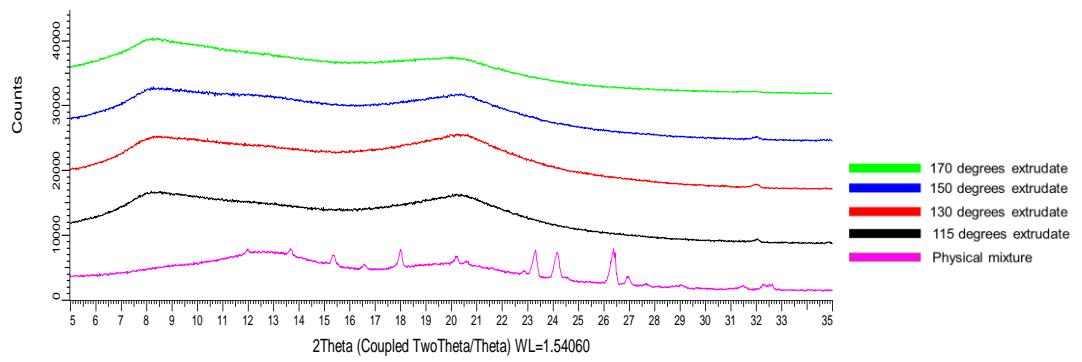


Figure 4.7: X-ray diffraction patterns of 10 wt% paracetamol as a physical mixture and extrudates produced at different temperatures

It can be seen that the physical mixture still has peaks consistent with crystalline paracetamol. On the other hand, all extrudate samples at various temperatures have resulted in a fully X-ray amorphous sample for this concentration of paracetamol.

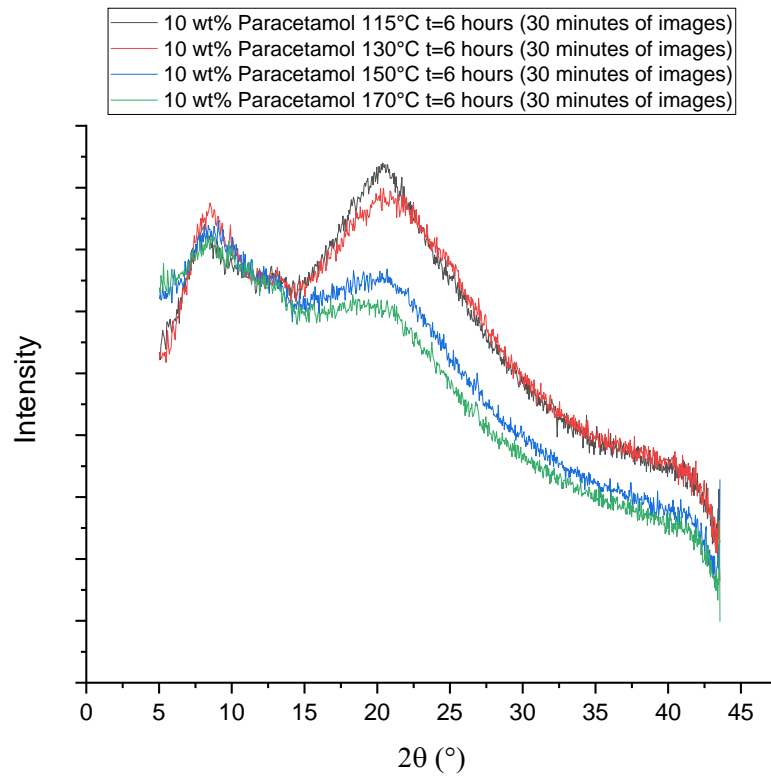


Figure 4.8: WAXS data of dissolution profile of 10 wt% paracetamol extruded at 115, 130, 150 and 17°C. Profiles are at 115°C (Black), 130°C (Red), 150°C (Blue) and 170°C (Green) all at t=6 hours after introduction of 1 mL of deionised water using a syringe

All extrudate samples were loaded into the sample holder as per Figure 4.1, 1 mL of deionised water was introduced using a syringe. The sample was continuously scanned over a time frame of 6 hours, with each image lasting for 60 seconds. No crystallinity was observed in any of the 10 wt% samples over this timeframe using this experimental setup.

For all samples, the data at T=0 hours had spectra which were more flattened out than at T=6 hours (see Figure 4.8). It is hypothesised that the flatter broader spectra at T=0 are due to the presence of more liquid water which has not

evaporated or been absorbed by the extrudate filaments. Also, the placement of the filament in the water at T=0 was difficult to control resulting in an unpredictable amount of filament exposure to the beam, and thus some T=0 spectra were broader and flatter while others had more peak definition. After six hours most of the water has been incorporated into the filament. Thus, we consider the spectra at T=6 hours to be more reliable as the samples appeared to be homogenous gels at this point. Consequently, the introduction of water proved to be a challenge in obtaining reproducible data at T=0 hours. However, because we are interested in what happens in the crystallinity of the sample after dissolution starts and crystallinity is indicated by distinct sharp peaks in the WAXS spectra, the broad peaks at T=6 hours in the absence of sharp distinct crystalline peaks are sufficient to show the sample is still amorphous, and thus the spectra at T=0 are not needed.

4.3.2.1 Analysis of 20 wt% Paracetamol ASD Formulation

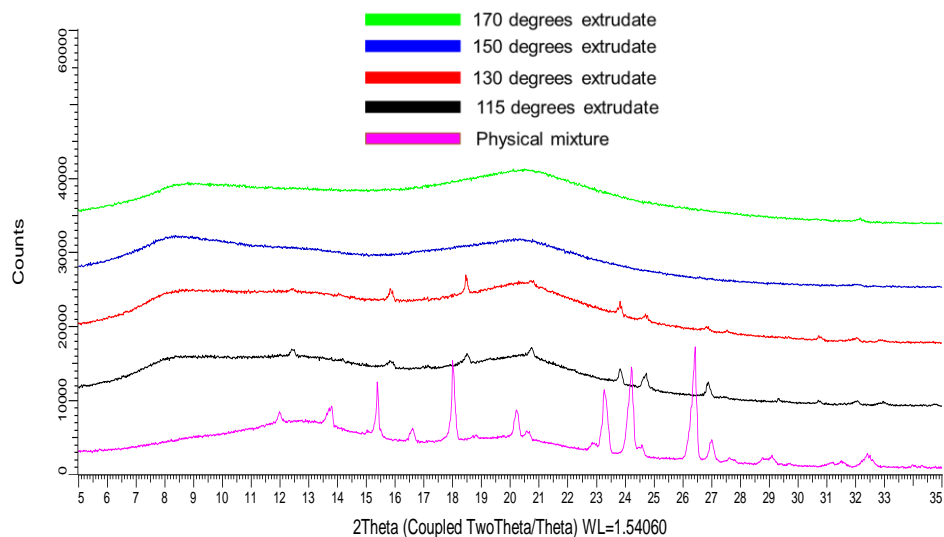


Figure 4.9: X-ray diffraction patterns of 20 wt% paracetamol as a physical mixture and extrudates produced at different temperatures

It can be seen that the physical mixture still has peaks consistent with crystalline paracetamol (see Figure 4.9). There are also crystalline peaks present in the samples extruded at 115 and 130°C, while the samples extruded at 150 and 170°C are fully X-ray amorphous.

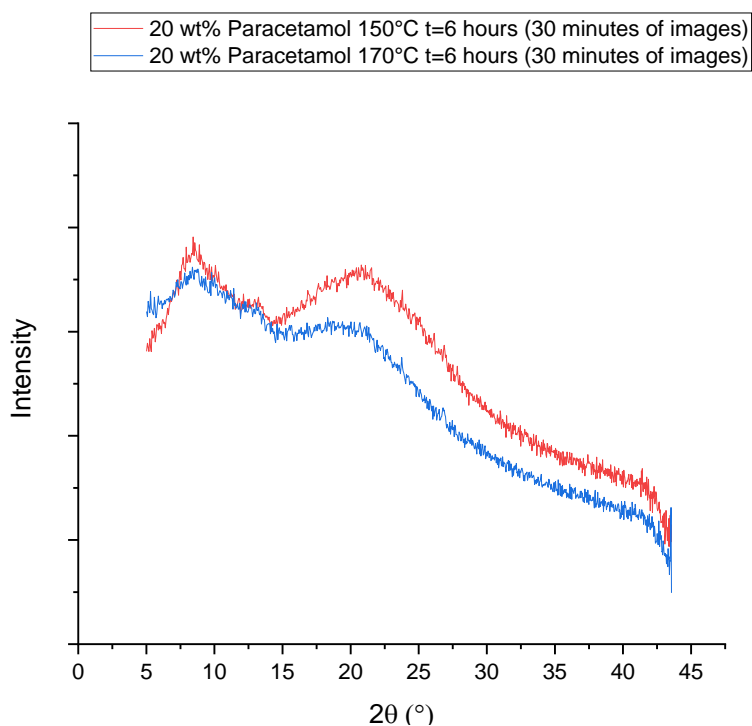


Figure 4.10: WAXS data of dissolution profile of 20 wt% paracetamol extruded at 150 and 170°C. Profiles are at 150°C (Red) and 170°C (Blue) all at t=6 hours after introduction of 1 mL of deionised water using a syringe

Extrudate samples were loaded into the sample holder as per Figure 4.1, 1 mL of deionised water was introduced using a syringe. The sample was continuously scanned over a time frame of 6 hours, with each image lasting for 60 seconds. No crystallinity was observed in any of the 10 wt% samples over this timeframe using this experimental setup (see Figure 4.10).

4.3.2.2 Analysis of 25 wt% Paracetamol ASD Formulation

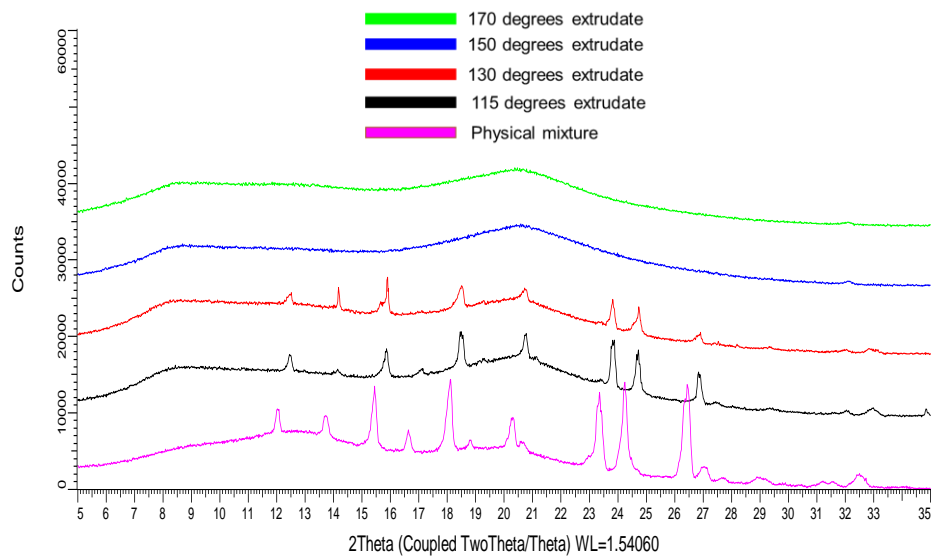


Figure 4.11: X-ray diffraction patterns of 25 wt% paracetamol as a physical mixture and extrudates produced at different temperatures

It can be seen that the physical mixture still has peaks consistent with crystalline paracetamol. There are also crystalline peaks present in the samples extruded at 115 and 130°C, while the samples extruded at 150 and 170°C are fully X-ray amorphous (see Figure 4.11).

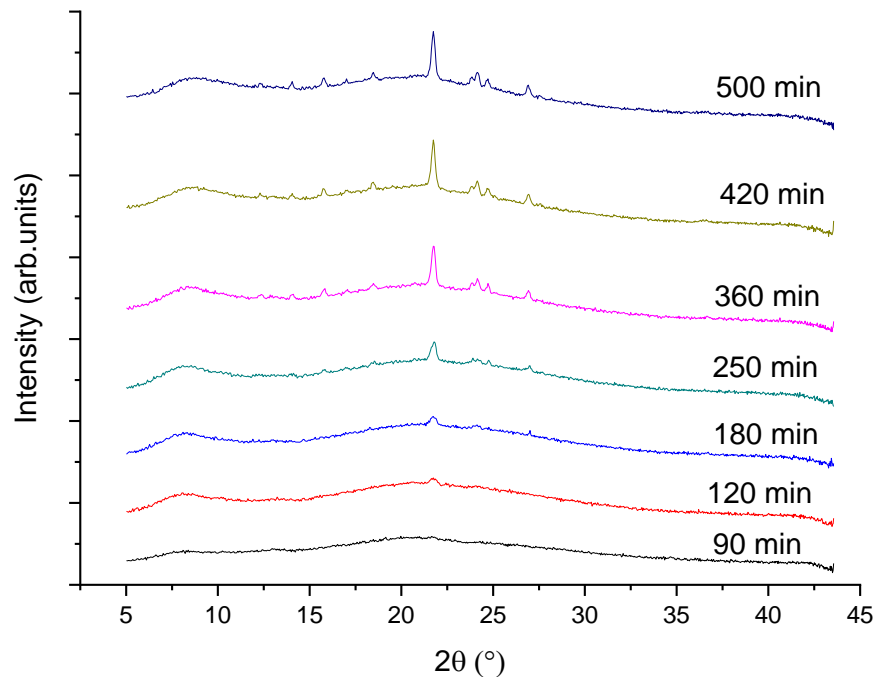


Figure 4.12: WAXS patterns of 25 wt% 150°C paracetamol ASD after wetting with deionised water

The 25 wt% sample extruded at 150°C was loaded into the sample holder as per Figure 4.1, 1 mL of deionised water was introduced using a syringe. The sample was continuously scanned over a time frame of 500 minutes.

After 90 minutes the profile is still showing no peaks and appears X-ray amorphous, at around 120 minutes the first crystalline peaks were observed at approximately 22°. As time increases and the contact time with the deionised water increases more crystalline peaks can be seen to be emerging. These peaks continue to increase in size until approximately 420 minutes where the peak size appears to plateau until the final time point of 500 minutes (see Figure 4.12).

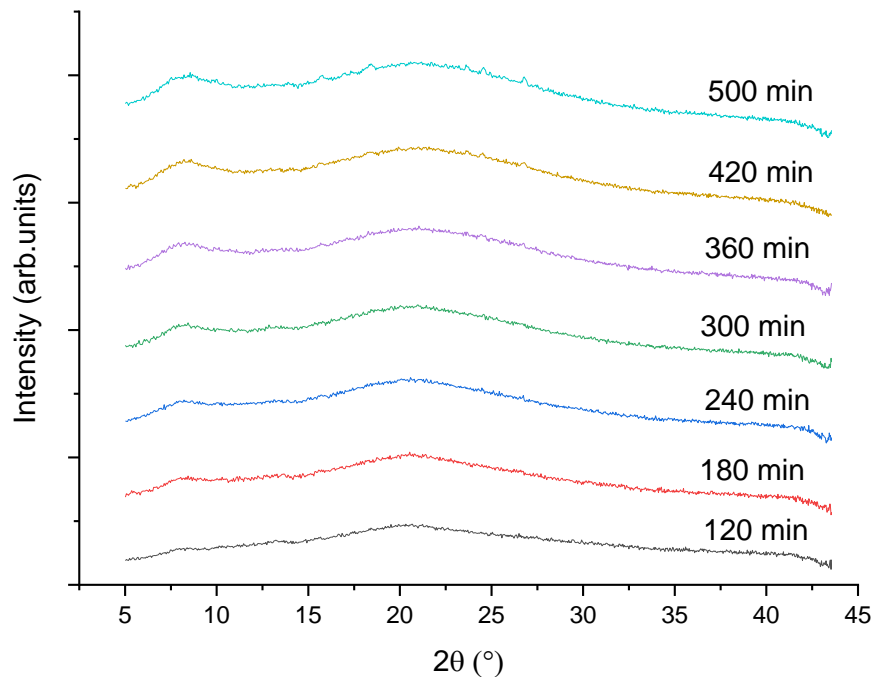


Figure 4.13: WAXS patterns of 25 wt% 170°C paracetamol ASD after wetting with deionised water

The 25 wt% sample extruded at 170°C was loaded into the sample holder as per Figure 4.1, 1 mL of deionised water was introduced using a syringe. The sample was continuously scanned over a time frame of 500 minutes.

After 360 minutes the profile is still showing no peaks and appears X-ray amorphous, at around 420 minutes the first crystalline peaks were observed at approximately 22-27°. At the final time point of 500 minutes, these peaks appear to have increased in size and there are also further crystalline peaks seen between 15 and 20° (see Figure 4.13).

4.3.2.3 Analysis of 27.5 wt% Paracetamol ASD Formulation

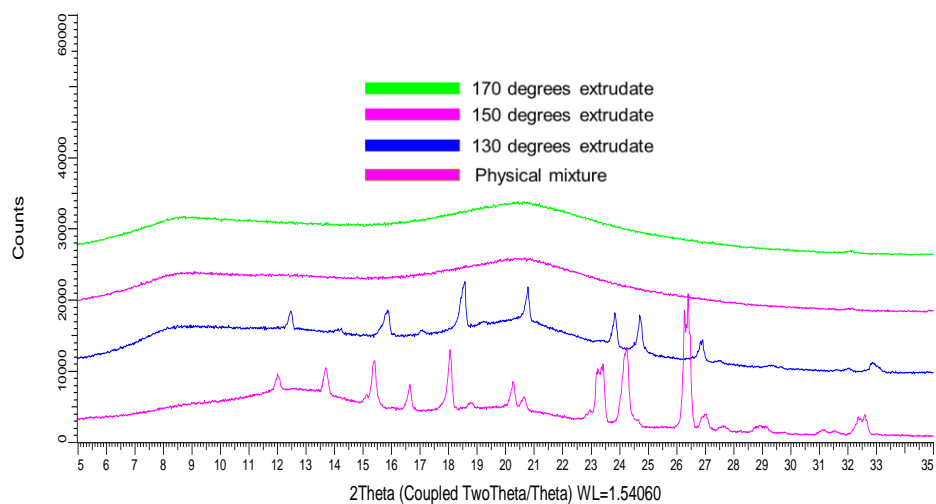


Figure 4.14: X-ray diffraction patterns of 27.5 wt% paracetamol as a physical mixture and extrudates produced at different temperatures

It can be seen that the physical mixture still has peaks consistent with crystalline paracetamol. There are also crystalline peaks present in the samples extruded at 130°C, while the samples extruded at 150 and 170°C are fully X-ray amorphous (see Figure 4.14).

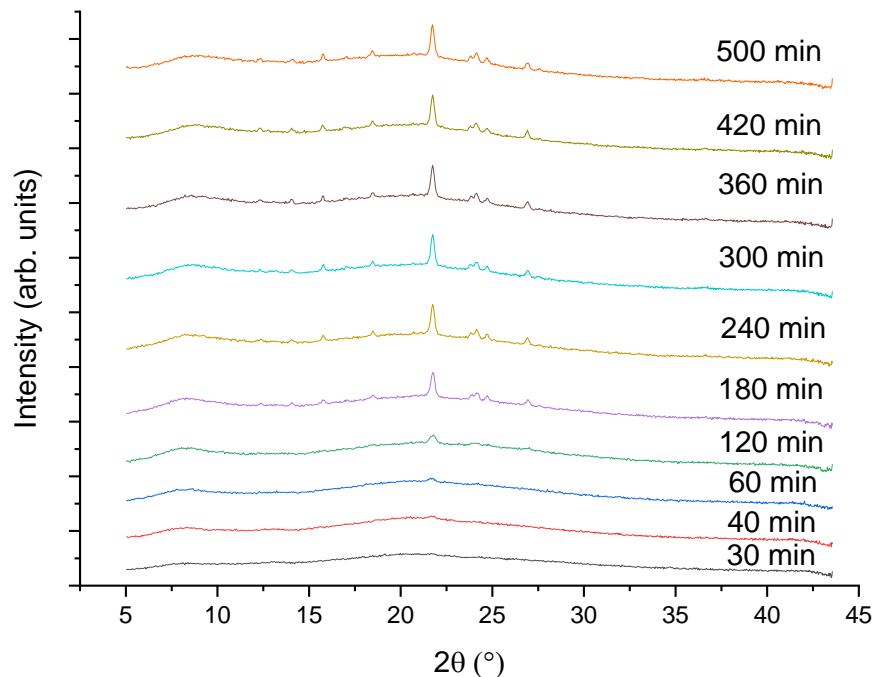


Figure 4.15: WAXS patterns of 27.5 wt% 150°C paracetamol ASD after wetting with deionised water

The 27.5 wt% sample extruded at 150°C was loaded into the sample holder as per Figure 4.1, 1 mL of deionised water was introduced using a syringe. The sample was continuously scanned over a time frame of 500 minutes.

After 30 minutes the profile is still showing no peaks and appears X-ray amorphous, at around 40 minutes the first crystalline peak is observed at approximately 22° , from tracking this peak there is an increase in peak size consistent with increasing crystallinity with time. After 180 minutes more crystalline peaks become visible in the range of $\sim 13-27^\circ$, this again confirms the increasing crystallinity of the sample with time (see Figure 4.15).

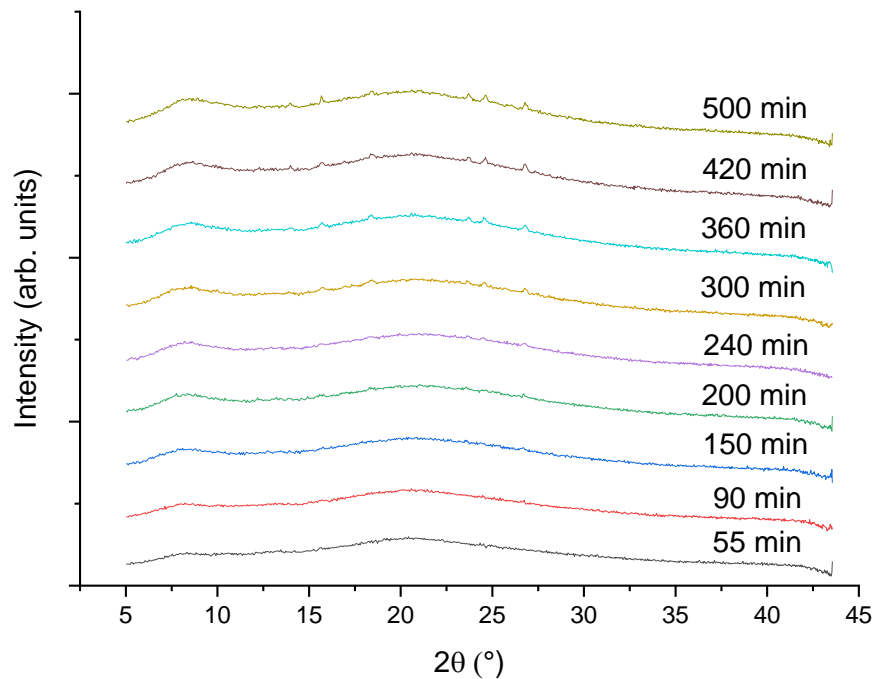


Figure 4.16: WAXS patterns of 27.5 wt% 170°C paracetamol ASD after wetting with deionised water

The 27.5 wt% sample extruded at 170°C was loaded into the sample holder as per Figure 4.1, 1 mL of deionised water was introduced using a syringe. The sample was continuously scanned over a time frame of 500 minutes.

After 90 minutes the profile is still showing no peaks and appears X-ray amorphous, at around 150 minutes the first crystalline peak is observed at approximately 22°, from tracking this peak there is an increase in peak size consistent with increasing crystallinity with time. After 300 minutes more crystalline peaks become visible in the range of ~13-27°, this again confirms the increasing crystallinity of the sample with time (see Figure 4.16).

The increased stability of ASDs of the same composition when processed at a higher temperature is explained by the increased molecular motion resulting in a greater solubility of the paracetamol in the Affinisol™. The greater molecular mobility afforded to the paracetamol and Affinisol™ at higher extrusion temperatures allows for better mixing to be achieved. At lower temperatures, the drug and polymer mixture is subjected to micromixing, as opposed to when the temperature is increased, molecular level mixing is achieved creating greater drug-polymer miscibility with an absence of crystalline API to act as nucleation sites promoting crystallisation.

Previous research studying paracetamol and Affinisol™ dispersions suggested that there may be a “critical concentration” for drug loading to maintain stability within the system¹²⁵. Through the use of in-line THz Raman spectroscopy, this was deemed to be at 20 wt% paracetamol. During the conduct of the study, it was observed that at 20 wt% paracetamol and below the API was undersaturated and fully amorphous. However, above this “critical concentration” the system was at a supersaturated level where crystalline material may be present in the polymer-API matrix. The work shown here has helped to confirm this finding with no crystallisation observed at paracetamol concentrations of 20 wt% and below, while formulations containing 25 wt% and 27.5 wt% paracetamol underwent recrystallisation when exposed to deionised water.

It is thought that there are three main mechanisms of dissolution that ASDs can undergo. There is carrier controlled release, whereupon dissolution media ingress into the polymer a gel-like material is formed in which the API has to diffuse to the surface to be delivered. Dissolution-controlled release occurs when the polymer and API both release together (congruent release), this allows the polymer to continue to stabilise the amorphous API in solution. Finally, there is the drug-

controlled release which is described as the polymer matrix dissolving into the dissolution media and the amorphous API can dissolve at a drug-controlled rate.

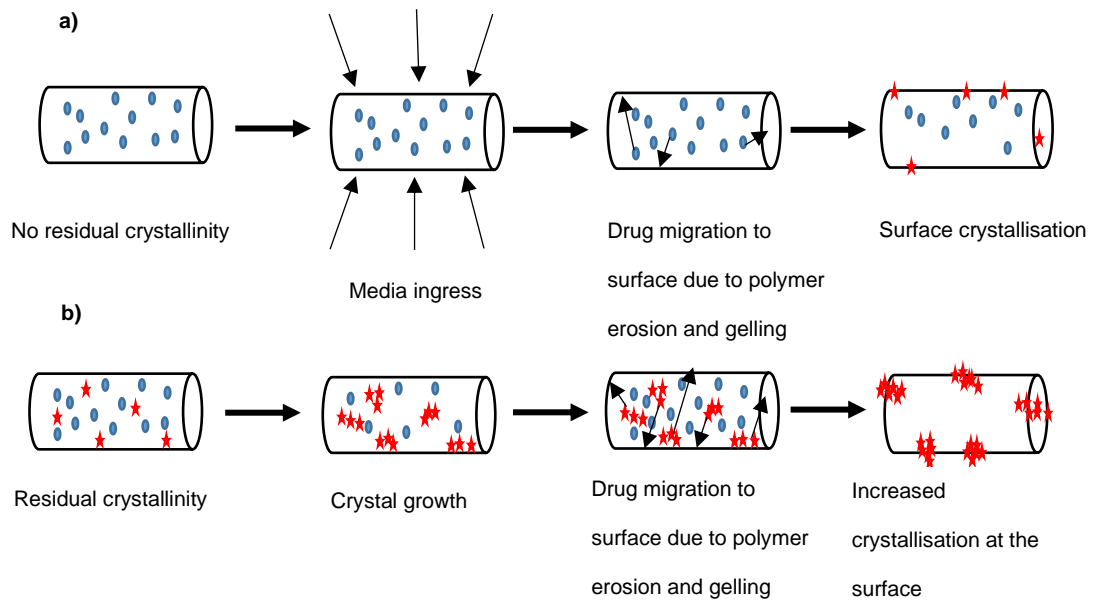


Figure 4.17: Schematic representation of crystallisation pathways during the dissolution of ASDs a) No residual crystallinity, limited surface crystallisation b) Residual crystallinity, surface crystallisation. Amorphous material = ●, crystalline material = ★

For samples above the critical concentration of 20 wt% paracetamol which underwent a crystallisation process, it was observed that crystallisation had occurred on the surface of the extrudate which had formed a gel-like material. These observations suggest that a carrier-controlled release dissolution mechanism has taken place, and the gelling of the polymer matrix has facilitated the diffusion of the API to the surface due to the increased molecular mobility. At the non-sink conditions used for these studies, the migration of the amorphous paracetamol to the surface has allowed drug-rich regions of amorphous paracetamol. The drug-rich amorphous regions have then been able to interact and finally crystallise at the surface (see Figure 4.17).

4.4 Summary

Modification of existing SAXS sample holders allowed for WAXS studies to be carried out with an area detector on the X-ray instrument. There is an advantage of quick image times from the combination of micro source flux and the use of an area detector over conventional X-ray position-sensitive detectors and sealed tubes. This instrument set-up for data acquisition allowed for the successful identification of the phase transition from ASD to a crystalline form during the dissolution study. Initial experiments confirmed the hypothesis from the previous work¹²⁵ in that results show a stable drug loading range below 20 wt% paracetamol as no crystallisation was observed after 6 hours of initial dissolution. Supersaturated samples above this drug loading threshold did show crystallisation.

It was also noted that for samples which did crystallise, the temperature of the extrusion had an impact on the time of the onset of crystallisation of the paracetamol. When samples of equivalent drug loading were extruded at different temperatures, the samples extruded at higher temperatures appeared to be more stable in that they took longer to show initial crystallisation. The extent of crystallisation at equivalent time points was indicated by the increased number and intensity of diffraction peaks than samples extruded at lower temperatures.

A more refined sample holder stage would help with the consistency of measurements for this type of analysis and allow for a better method of introducing dissolution media. With a more refined setup, it may be possible to extract more information from the data obtained.

Clearly, an improved understanding of the changes within an ASD structure upon drug release could lead to a better understanding of the underlying mechanisms involved when an API starts to crystallise. A longer-term goal remains to use this knowledge to improve the formulation and processing of ASDs. Further work would be required combining SAXS with WAXS to compare structural changes at different lengthscales.

The work presented here shows the feasibility of using a lab-based SAXS instrument in terms of incident flux coupled with an area detector clearly showing the emergence of crystallinity over time. The repeated observation of crystallisation on the extrudate surface can be explained by diffusion occurring at the surface of the extruded ASD.^{117,131} The mixed phase samples of ASD in dissolution media masked any contribution from changes in the ASD matrix such as swelling, erosion, and disintegration that may have been expected to give rise to SAXS signals. Thus, the recommendation from this work is to track changes in crystallinity in the lab using WAXS and resort to synchrotron-based SAXS, pair distribution function (PDF) and/or computed tomography (CT) measurements to assess pre-crystallisation changes in the ASD sample. The release of paracetamol from these systems would therefore appear to be impacted by a crystallisation-mediated process whereby the dispersed paracetamol recrystallised at the surface and subsequently dissolves in addition to any erosion of the ASD matrix. Tracking the physical form during dissolution using diffraction or scattering techniques serves as a useful tool to assess the stability and performance of the ASDs.

Chapter 5: Investigation of Crystallinity in an Active Pharmaceutical Ingredient

5.1 Introduction

Amorphous pharmaceuticals are an attractive solution to address solubility issues that are commonly encountered with newly developed active pharmaceutical ingredients.⁴⁶ Many crystalline pharmaceuticals can be prepared in their amorphous form to overcome solubility issues associated with the crystalline state. This can result in improved properties such as increased solubility and oral bioavailability, allowing promising drug candidates displaying poor solubility in their crystalline form to be utilised.^{2,3,4}

However, amorphous solids often suffer from poor stability arising from excess free energy compared with crystalline forms which can lead to recrystallization. This risk of physical instability also presents regulatory challenges in getting amorphous solids through regulatory approval.^{5,6,7,8} Although a promising method for increasing solubility and bioavailability, for some products the formation of an amorphous phase can be problematic with the unexpected or uncontrolled appearance of amorphous content and associated variability in physical and chemical properties. For example, an amorphous phase can be produced unintentionally during the processing of a drug substance or drug product. The energy provided by manufacturing methods (milling, sieving etc) can disrupt the crystal lattice of material and lead to the formation of varying amounts of an amorphous phase within the bulk crystalline API.^{9,10,11,12}

The amorphous state is not as straightforward to characterise or identify unambiguously as the crystalline form, often requiring the use of multiple techniques. Crystalline material can be characterised by routine analytical techniques such as single crystal and powder XRPD to provide detailed structural information with thermal methods such as DSC providing information on characteristic thermal properties.^{142,143} WAXS or traditional XRPD techniques can

access information on the atomic/molecular dimensions within materials corresponding to a length scale in the Ångstroms. Thus, it can be used for phase ID, pattern indexing, as well as crystal structure determination yielding crystal structure in atomic resolution in three dimensional periodic lattices. WAXS however cannot provide information on the material structure at the nanoscale in materials given the restrictions in accessing very low scattering angles arising from standard XRPD instrument geometries. SAXS can determine structural features of particle systems at the nano and meso scale and is most commonly used for looking at the structure and dynamics of large molecules in low ordered environments. The main difference when comparing SAXS and WAXS is the length scales accessible, where WAXS can probe lengths comparable to atomic planes in a crystal, SAXS looks at much bigger length scales due to the lower angle of the scattering observed. SAXS can also be used to analyse a wide range of samples such as nanoparticles, where it is used to characterise size and shape,^{79,144} structural biology to determine the structure of proteins in solution^{145,146} and in the polymer industry to determine structural properties and crystallisation behaviour for a wide range of applications.^{147,148} Interestingly, given the potential structural features (Figure 5.1) in mixed phase or phase separated amorphous systems in particular, SAXS has seen relatively limited application in their characterisation. Recently SAXS analysis of partially amorphous pharmaceutical materials has been reported showing the useful information that can be delivered from this technique.

In SAXS, the detection and analysis of X-ray scattering from the edges of domains within a system are possible. For example, in an amorphous system, domain edges can correlate to the boundary of the phase densities between crystalline

and amorphous regions as compared to the scattering within the lattice itself, as demonstrated in Figure 5.1.

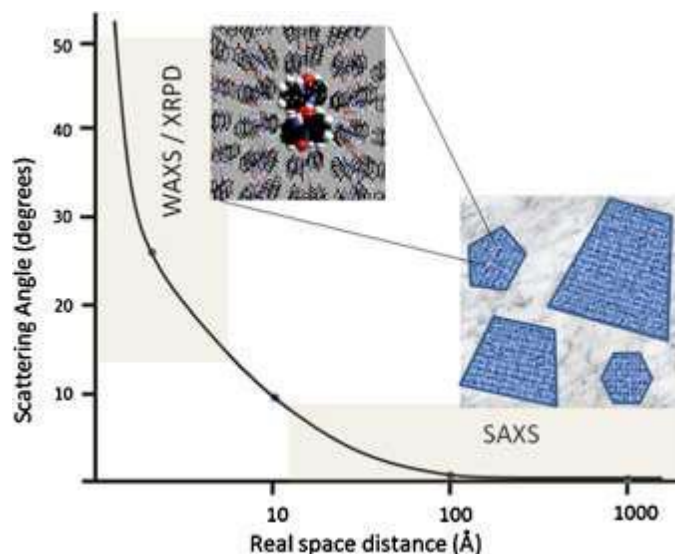


Figure 5.1: Demonstration of structural features present in SAXS vs XRPD data⁹³

Density fluctuations must be present within a material for a SAXS signal to be observed, and it is, therefore, possible that an ideal crystalline or amorphous sample would not produce a signal as there would be no contrast within the sample.⁹³ However, when amorphous material is present in a bulk crystalline material, or vice versa, there is the potential for different density domains to exist producing a SAXS signal.⁹³

The Porod invariant (Q), which can be obtained from SAXS data, can be used as a means of measuring the nano-heterogeneity of amorphous samples. In a multi-phase system with regions of differing scattering length densities (SLD), the Porod invariant is equal to the integral over the whole scattering vector and is directly proportional to the mean-square density fluctuation.^{93,149} The Porod invariant across the whole scattering range is defined as shown in Eqn 5.1, where I_q is the intensity over the whole scattering vector and q^2 is the scattering vector.

$$Q = \int_0^{\infty} I_q q^2 dq \quad \text{Eqn 5.1}$$

Along with the mean square density fluctuation for a two-phase system shown in Eqn 5.2.

$$\langle (\rho - \bar{\rho})^2 \rangle = (\Delta\rho)^2 \cdot \varphi_1\varphi_2 \quad \text{Eqn 5.2}$$

In Eqn 5.2 $\bar{\rho}$ is the average density throughout the scattering volume, φ_1 and φ_2 are the volume fractions of both phases and $\Delta\rho$ is the electron density difference.

These equations can be combined to give:

$$Q = \int_0^{\infty} I_q q^2 dq = \langle (\rho - \bar{\rho})^2 \rangle \cdot (\Delta\rho)^2 \cdot \varphi_1\varphi_2 \quad \text{Eqn 5.3}$$

Therefore, the invariant is a measure of a sample's heterogeneity and can be used to gather information on the nature of the distribution of crystalline and amorphous domains within a sample. A study looking at the Porod invariant of three pharmaceutical APIs (sulfamerazine, simvastatin and desvenlafaxine succinate) investigated the use of SAXS and the Porod invariant as a means of determining structural differences of glassy systems prepared via different methods and also the structure and stability of cryo-milled samples. This study found that different methods of amorphisation of the same molecule resulted in markedly different SAXS profiles, the harsher method of melt-quenching produced practically no SAXS signal while a sample amorphised by milling produced a SAXS signal comparable to the starting crystalline material. These results indicated that although both samples appear to be fully amorphous, as shown by WAXS, the nanoscale amorphous structure varied based on the method of amorphisation. The study also found that the degree of nano-heterogeneity, as measured by the invariant, was impacted by the length of time a sample is subjected to milling. Samples that had been milled for longer tended to show reduced SAXS intensity,

lower nano-heterogeneity and were more stable in the amorphous form than samples with a shorter milling time that tended to recrystallise back to the original crystalline state.⁹³

The work in this study aims to evaluate the use of SAXS in the characterisation of amorphous small organic molecules, employing invariant analysis of samples subjected to ball milling at various parameters. A variety of other techniques such as XRPD, DSC, TGA, FTIR and SEM will be used to provide complementary data to allow a better understanding of the SAXS data.

5.2 Experimental

The raw material, GSK2838232M as provided by GSK, was analysed as received to provide a benchmark for amorphous materials generated and analysed in this chapter.

5.2.1 Preparation of amorphous GSK2838232M samples

Amorphous samples of GSK2838232M were prepared via ball milling with a Retsch MM400 ball mill as described in section 3.2.1.2. A series of eight increasingly amorphous samples were prepared by adding approximately 250mg of GSK2838232M starting material to a 5mL ball milling jar along with one 7 mm steel ball performed at a frequency of 25Hz. Increasing amorphicity was achieved by increasing the milling time as shown in Table 5.1.

Table 5.1: Ball milling parameters used to produce amorphous samples

Sample	Milling Time (minutes)	Milling Frequency (Hz)	Milling balls used
1	5	25	1 x 7 mm
2	10	25	1 x 7 mm
3	20	25	1 x 7 mm
4	30	25	1 x 7 mm
5	40	25	1 x 7 mm
6	45	25	1 x 7 mm
7	50	25	1 x 7 mm
8	60	25	1 x 7 mm
9	60	30	2 x 7 mm

A further fully X-ray amorphous form was also prepared via ball milling. 275mg of GSK2838232M was added to a 5mL ball milling jar along with two 7mm steel balls. The milling was performed at a frequency of 30 Hz for 60 minutes.

5.2.2 Small Angle X-ray Scattering

SAXS data were gathered using a Xeuss 2.0 SAXS/WAXS laboratory beamline (Xenocs, Grenoble) as described in section 3.2.2.1. Samples were loaded in 0.7 mm borosilicate capillaries and mounted in a capillary sample stage at a distance of 2500 mm from the detector. The beam was set to high-resolution mode to give a beam size of 0.6 x 0.5 mm. Data were collected from each sample in the range of 0.045-0.26 Å in the SAXS region.

Table 5.2: Instrument parameters used for SAXS experiments

SAXS Instrument Parameters	
Source	Cu α_1 – 1.54189Å
Collimation / Beam setting	High resolution (0.6 x 0.5 mm)
Detector	SAXS – Pilatus 1M
Calibrated sample to detector distance	2476.64 mm
Sample stage	Standard Transmission Stage
Image time	3600 s
Range	0.012 – 0.26 Å ⁻¹ , 0.1-3.5° (139 – 2.4 nm)

5.2.3 X-ray Powder Diffraction

All ball-milled samples and the starting material were analysed using XRPD to determine the amorphous nature. Samples were analysed using a Bruker D8 Advance II capillary diffractometer as described in section 3.2.2.3. Small amounts of samples (10-50 mg) were packed into 0.7 mm borosilicate capillaries and scanned in the range of 3-40° 2 θ with a step size of 0.017° and a 10 s/step count time.

Variable temperature XRPD was collected on the starting material using a Bruker D8 advance capillary diffractometer as described in section 3.2.2.3. Small amounts of samples (10-50 mg) were packed into 0.7 mm borosilicate capillaries and scanned in the range of 3-40° 2 θ with a step size of 0.017° and a 10 s/step count time.

5.2.4 Fourier Transform Infrared Spectroscopy

ATR-FTIR data were collected using a Bruker Tensor II bench ATR IR spectrometer as described in section 3.2.1.6. Data was collected in the region of 400-4000 cm^{-1} with a resolution of 4 cm^{-1} and 16 scans were obtained for each sample.

5.2.5 Differential Scanning Calorimetry

DSC data were collected using a Netzch DSC214 Polyma instrument as described in section 3.2.2.4. 3-5 mg of sample was weighed into an aluminium pan with a pierced lid. The sample was initially heated from 20-280°C at a heating rate of 10°C/min. Following this samples were then further analysed by heating from 20-130°C at a heating rate of 10°C/min and cooled back to 20°C at a cooling rate of 10°C/min, under flowing helium purging gas at 40 ml/min. A blank correction was carried out with an empty pan before sample analysis.

5.2.6 Thermogravimetric Analysis

TGA analysis was collected using a Netzsch Jupiter F1 449 instrument as described in section 3.2.2.5. 3-5 mg of sample was accurately weighed out into an aluminium pan with a pierced lid. The sample was then heated from 20-300°C at a heating rate of 10°C/min, with a helium purge gas flow of 50 ml/min. A blank correction was carried out with an empty pan before sample analysis.

5.2.7 Scanning Electron Microscopy

SEM images were acquired for all ball-milled samples along with the starting material using a Hitachi TM 4000 plus as detailed in section 3.2.2.7. Samples were mounted on aluminium stubs with sticky carbon tabs and sputtered with a 20 nm layer of gold using a Leica EM ACE 200 sputter coater. Images were captured in backscattered mode with a beam voltage of 10 kV.

5.3 Results and Discussion

5.3.1 Characterisation of GSK2838232M starting material

5.3.1.1 X-ray Diffraction Characterisation of Crystalline Material

The parent material GSK2838232M was characterised as received using XRPD to give a reference pattern to confirm phase identity and compare against subsequent samples with potential amorphous content. The starting material comprised sharp diffraction peaks, and no obvious amorphous halo was evident in the background confirming the essentially crystalline nature of the material (Figure 5.2).

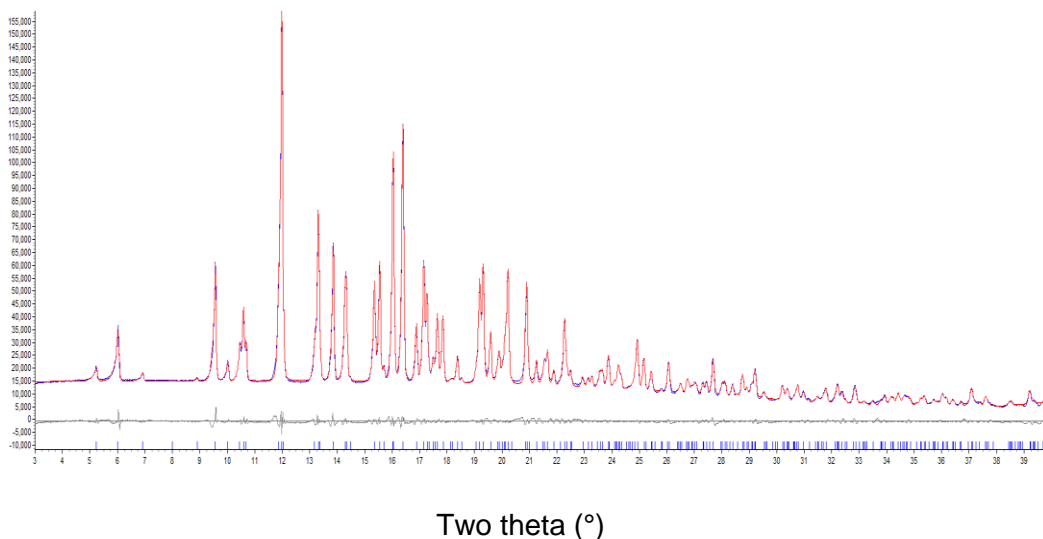


Figure 5.2: Pawley fit of the XRPD data of the starting material in the range of 3-40° two theta.

The Pawley fit^{19,20,21} to the data was performed in the Topas software package¹⁵³ in which zero point, background, peak shape, peak intensity and lattice parameters were refined. The refined, room temperature lattice parameters obtained from the fit were $a = 15.15 \text{ \AA}$, $b = 11.03 \text{ \AA}$, $c = 17.45 \text{ \AA}$ and $\beta = 104.41^\circ$.

5.3.1.2 DSC Analysis

DSC analysis of the starting material (Figure 5.3) showed that GSK2838232M had an onset temperature of melting at 265.7°C, along with an endothermic transition at 118.2°C.

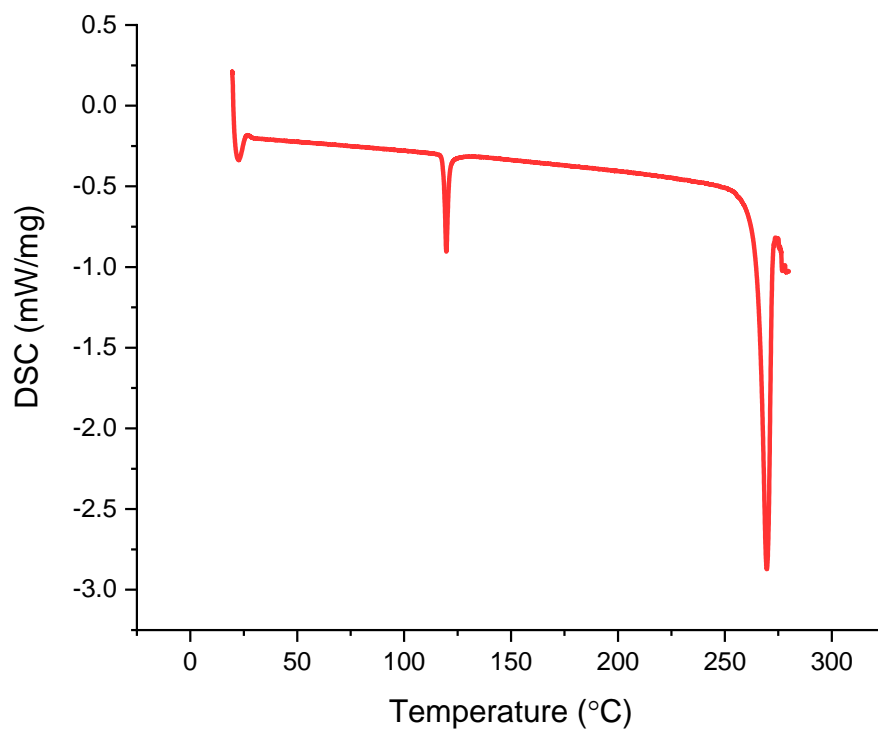


Figure 5.3: DSC profile of GSK2838232M in the range of 20-280°C

A further DSC experiment with an additional cooling cycle was performed to investigate whether the endothermic transition, seen at approximately 120°C, was reversible (Figure 5.4).

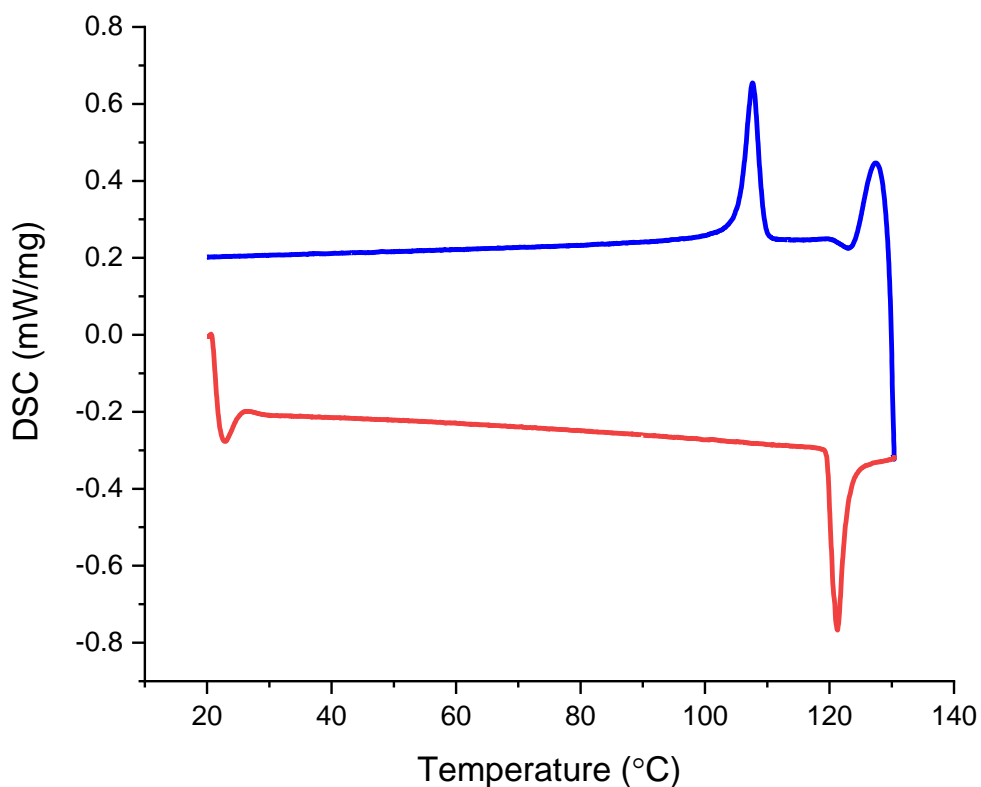


Figure 5.4: DSC heating (red line) and cooling (blue line) analysis of GSK2838232M

The repeat experiment confirmed the presence of the endothermic event upon heating. An exothermic peak was observed at around 107.1°C during the cooling cycle suggesting that the endothermic event was reversible.

5.3.1.3 Variable Temperature XRPD Analysis for Investigation of Potential Solid-Solid Transition in Starting Material

Variable temperature XRPD was performed to probe the sample for polymorphic transitions (see Figure 5.5).

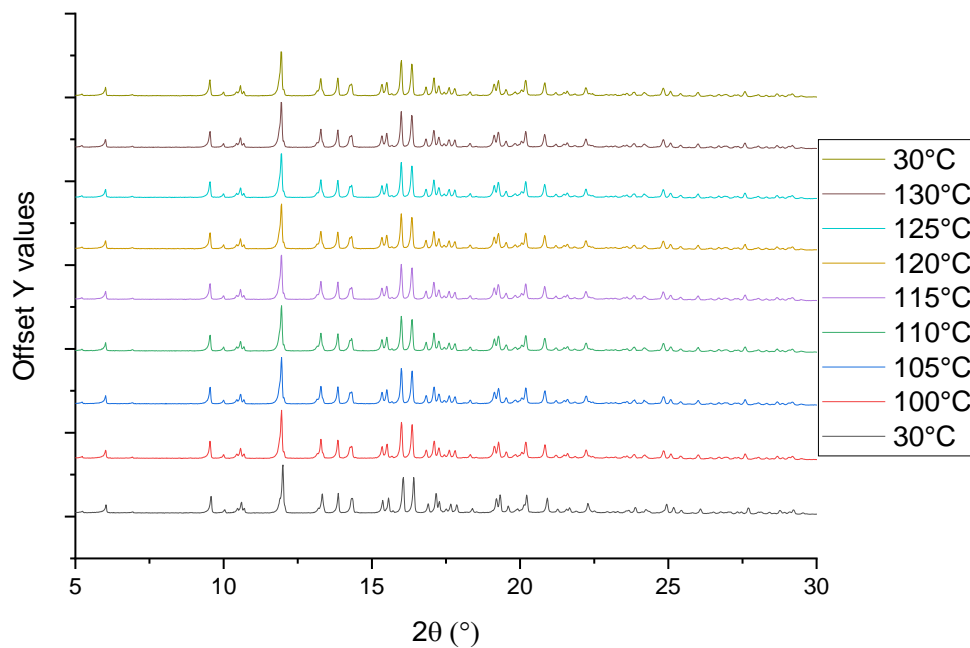


Figure 5.5: VT-XRPD diffractograms of GSK2838232M

A shift in the peak as indicated by the vertical line to lower two theta was observed between the first plot (30°C) and the second plot (100°C) as shown in Figure 5.6. No further differences in XRPD patterns were observed upon further heating.

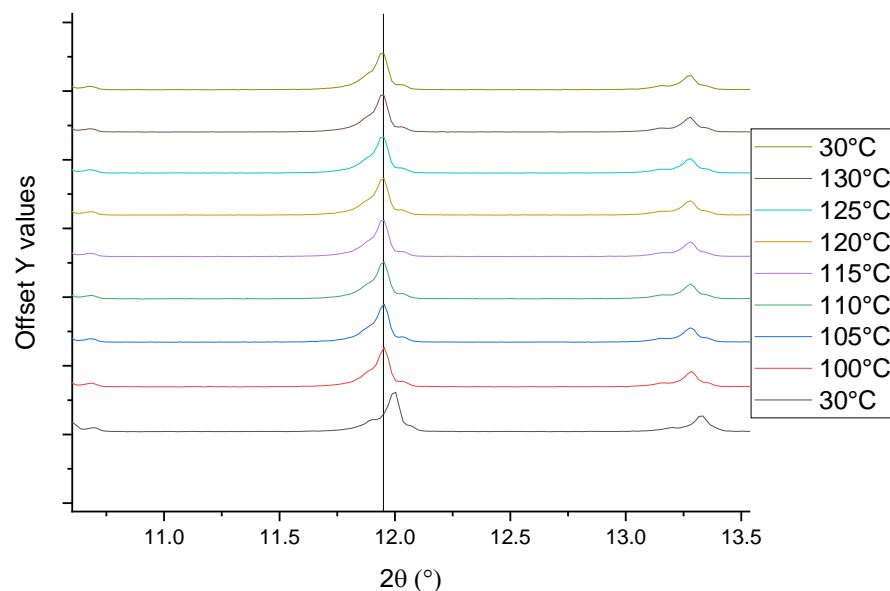


Figure 5.6: Zoomed in VT-XRPD diffractograms highlighting peak shift between 30°C and 100°C profiles, profiles displayed up to 130°C.

The observed peak shift is consistent with a thermal expansion of the crystal. This expansion would result in larger d-spacings for the longer range cell dimensions within the lattice, corresponding to a lower measured two theta value.^{154, 155} No evidence of a polymorphic transition was observed through this analysis as indicated by the lack of any other peak shifts. Thermal expansion as a cause for the initial peak shift was confirmed by indexing each pattern to calculate the lattice volume for each sample, as shown in Figure 5.7. The thermal expansion results demonstrated an increase in volume between the first and second temperature points, with no further increases or decreases observed. The increase in lattice volume occurred prior to the transition temperature seen in DSC, no further lattice volume changes were seen at this transition temperature. Although these results were interesting, there was no evidence to suggest the peak was relevant to the amorphous phase, and the finding had no direct relevance to the study.

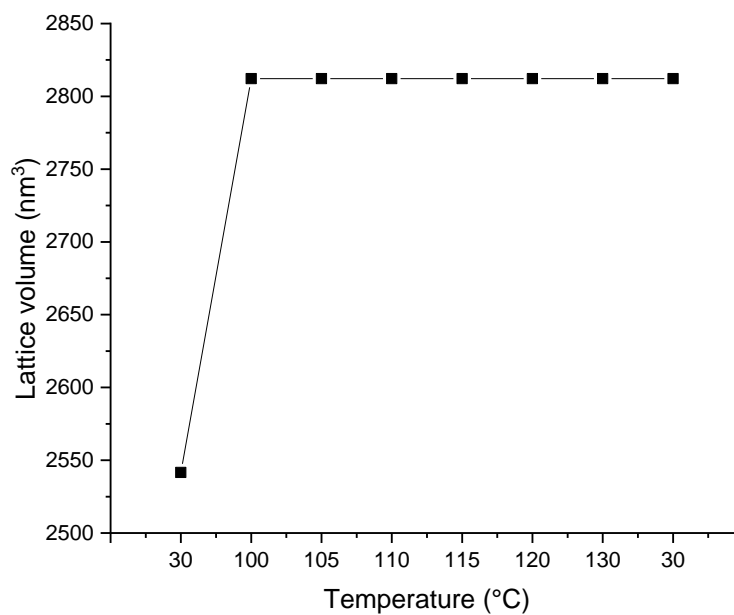


Figure 5.7: Crystal lattice volume of GSK2838232M as a function of temperature as measured by VT-XRPD

5.3.2 Characterisation of the relative crystallinity of ball-milled samples

5.3.2.1 X-ray Powder Diffraction Analysis for Characterisation of Increasing Amorphous Content

A series of amorphous samples were prepared using a Retsch MM400 ball mill with successively longer milling times. Each of these samples was then characterised using the same suite of techniques used for the starting material. Initial screening of the samples was performed using XRPD to determine at which ball mill settings amorphous material was introduced to the sample.

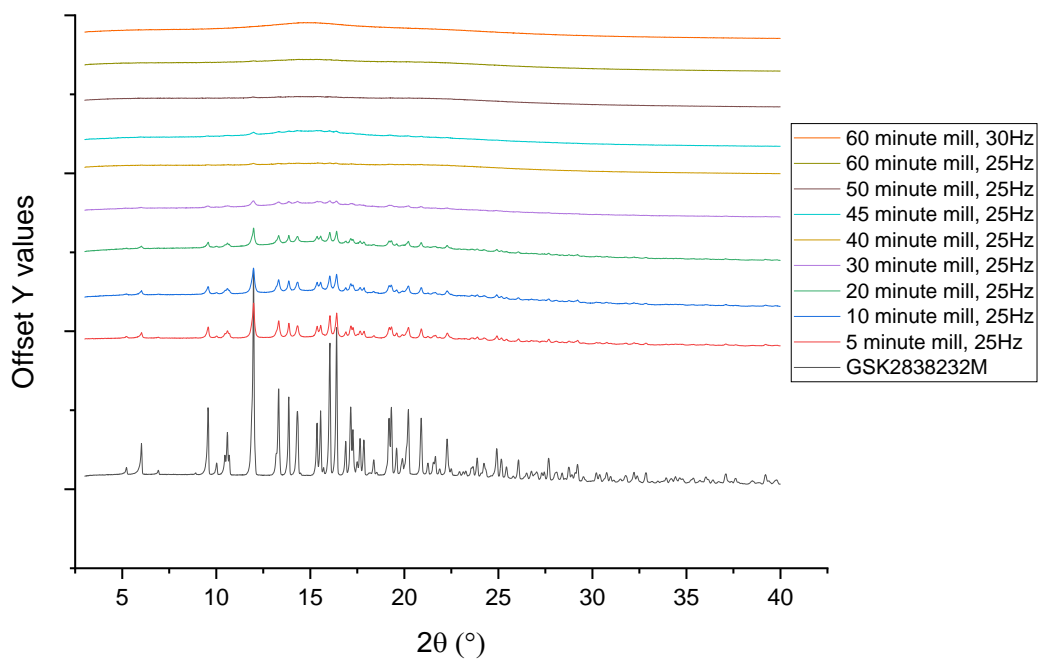


Figure 5.8: XRPD plots of series of amorphous samples produced with a Retsch MM400 ball mill

There are some characteristic strong diffraction peaks for GSK2838232M at a two theta of 12° , 13.5° and 16.5° . The peak at 12° two theta is the largest, and most intense in the pattern. Tracking this peak as the milling time increases showed a steady decrease until the peak was no longer present in the final diffractogram indicating a fully X-ray amorphous sample had been obtained at these milling conditions. This final diffractogram of a fully X-ray amorphous sample corresponds to a milling time of 60 minutes with a milling frequency of 30Hz, (Figure 5.8).

5.3.2.2 Relative Crystallinity Analysis Using DSC

DSC analysis of the milled samples (see Figure 5.9) confirmed the amorphous nature of the samples observed in the X-ray diffraction experiments. The DSC profiles of the samples show that there is an exothermic peak consistent with a re-crystallisation event found in the temperature range of 175-189°C. The increasing size of this feature is consistent with the increasing amorphous content of the samples, showing the same trend as was seen in the XRPD data with increasing amorphous content as a function of milling time.

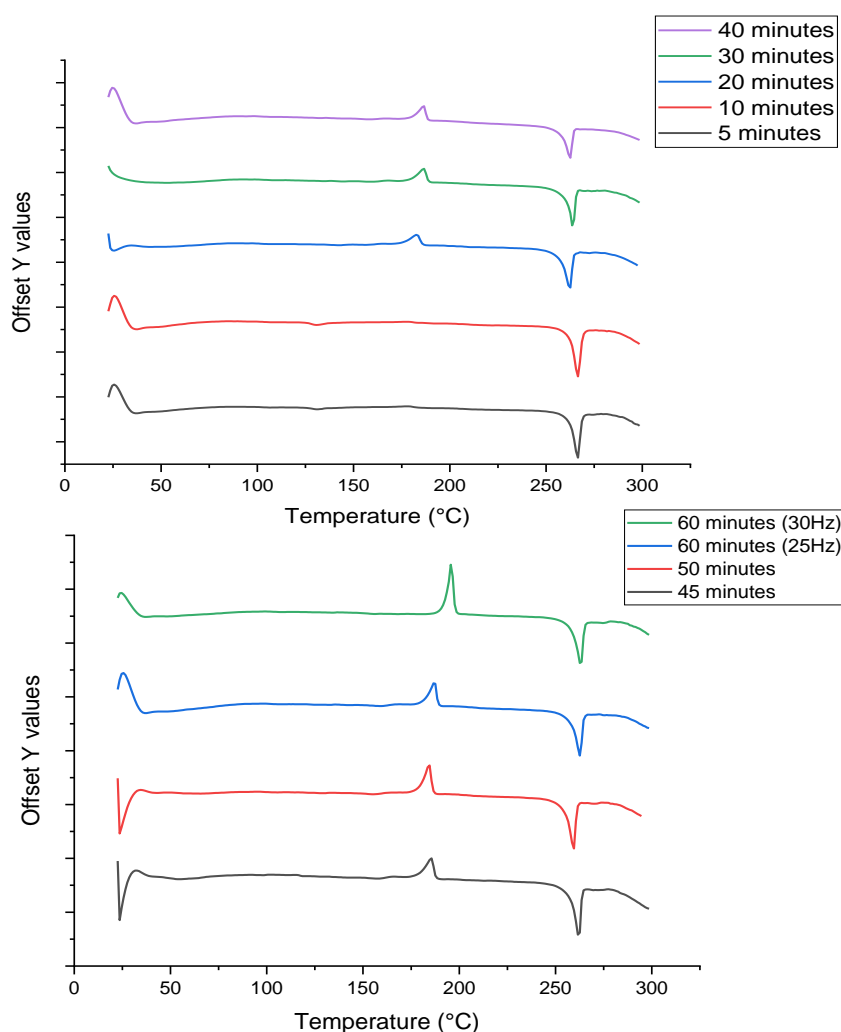


Figure 5.9: DSC profiles of all ball milled GSK2838232M samples (Top plot 5 minutes to 40 minutes milling, bottom 45 minutes to 60 minutes milling)

Mass fraction of crystalline material calculations were carried out based on the heat of crystallisation enthalpy and heat of melting as obtained from the DSC data Eqn 5.4.¹⁵⁶

$$X_c = \frac{\Delta H_m - \Delta H_c}{\Delta H_m^0} \quad \text{Eqn 5.4}$$

Where ΔH_m is the enthalpy of fusion of the sample at the melting temperature, ΔH_c is the crystallisation enthalpy of the sample and ΔH_m^0 is the heat of fusion of the crystalline GSK2838232M at the melting temperature. ΔH_c and ΔH_m values were obtained from NETZCH Proteus thermal analysis software. Results from this calculation are shown in Figure 5.10.

The mass crystalline fraction was converted to a percent crystallinity in the sample by multiplying X_c by 100. This method of calculating crystallinity has been used in other studies to show the % crystallinity of a sample containing amorphous material.¹⁵⁷ The data in Figure 5.10 shows a consistent downward trend to a minimum value of 7% crystallinity. The change to a higher milling frequency resulted in a substantial drop in % crystallinity, from 38% to 7%, due to the higher frequency of the impacts caused within the milling jar.^{158,159} There is some agreement with the data obtained from XRPD with an overall downward trend due to increased milling. However, unlike XRPD, which showed an absence of peaks at 60 minutes suggesting a fully amorphous sample had been produced, DSC analysis suggests there is still a low level of crystallinity within the sample. This could be due to several reasons, such as the difference in sensitivity of the two techniques, with DSC shown to be more sensitive to crystalline material.^{160,161} XRPD may be underestimating the crystallinity within the sample. The DSC method also relies on using the provided crystalline sample as the 100% crystalline baseline for the rest of the calculations. The initial sample used for this

may have had some amorphous material present which would then result in the calculation not being fully correct for the then milled samples. Finally, the sample presentation method for both techniques differs. For XRPD the sample was loaded into a borosilicate capillary which was then heat sealed, this would prevent any atmospheric changes to the sample. While for the DSC measurements the samples were loaded into pans with a pierced lid, this could have let any humidity within the room interfere with the sample and begin a recrystallisation process.

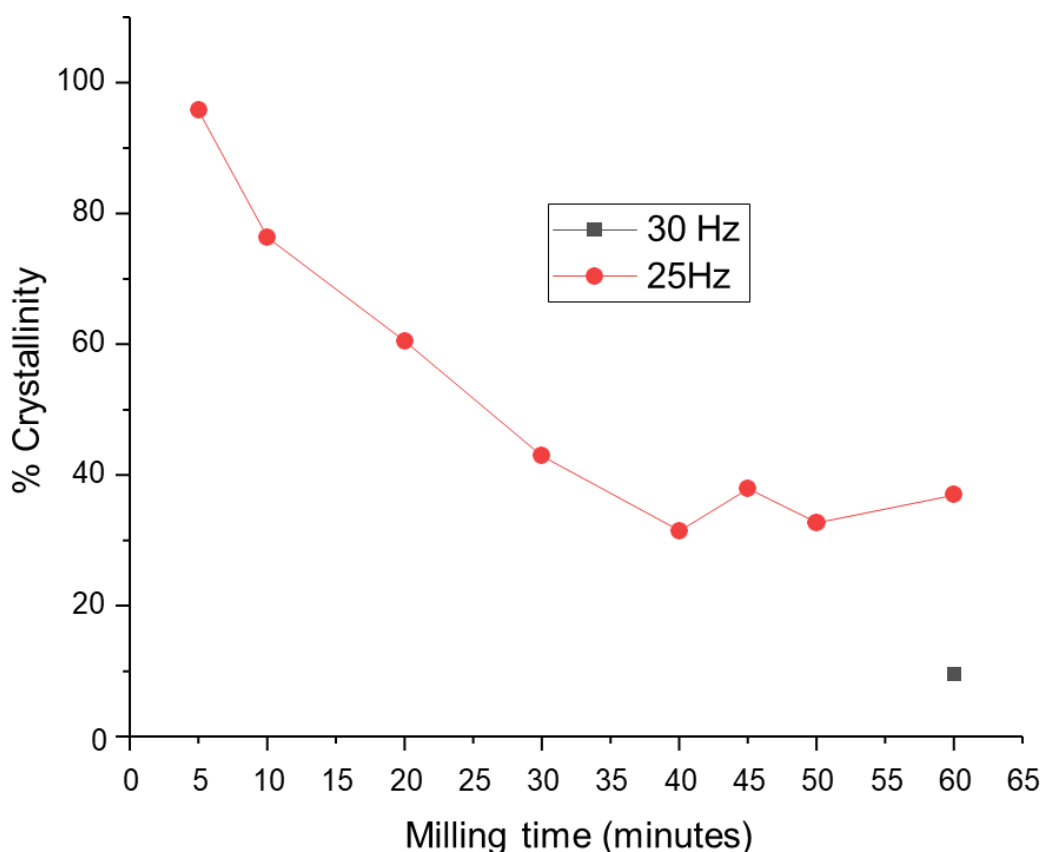


Figure 5.10: Crystallinity values calculated from DSC data using enthalpy of crystallisation and enthalpy of melting

5.3.2.3 Thermogravimetric Analysis of Mass Loss

TGA analysis showed an overall increase in mass loss as milling time increased. Milling loss starts at 0% in the parent material and increases to just over 1% mass loss in the heating range 30-90°C, this loss is most likely associated with surface water losses. Water from within the crystal lattice is released due to the milling process, some of this released water will have been able to attach to the surface of the molecule. As amorphous solids have a greater surface area than crystalline solids there is the potential for more water to be found on the surface and subsequently lost during the TGA experiment (Figure 5.11).^{162,163} The general trend of increasing mass loss as milling time is increased suggests an increase in amorphous content.

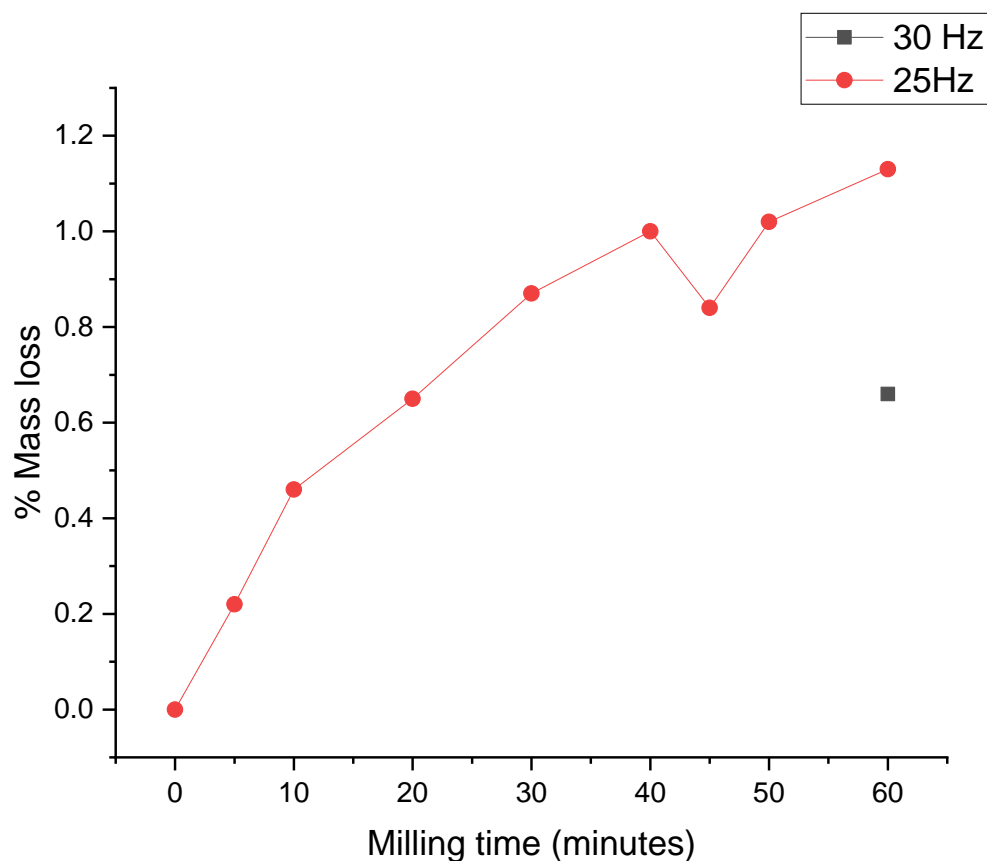


Figure 5.11: Mass loss trend analysis based on TGA data

5.3.2.4 Spectroscopic Structural Analysis using FTIR

FTIR analysis can provide information on structural modifications as a result of changing interactions within the molecule. Degradation of the sample can also be analysed via FTIR with loss of peaks signalling potential degradation from the crystalline to amorphous form.^{31,32,98} FTIR analysis of the milled materials shows peak broadening when compared to the crystalline material, particularly in the fingerprint region (Figure 5.12). This is consistent with disordered (amorphous)

solid materials having a greater variety bond lengths and bond energy distributions than seen in a crystalline material.^{166,167}

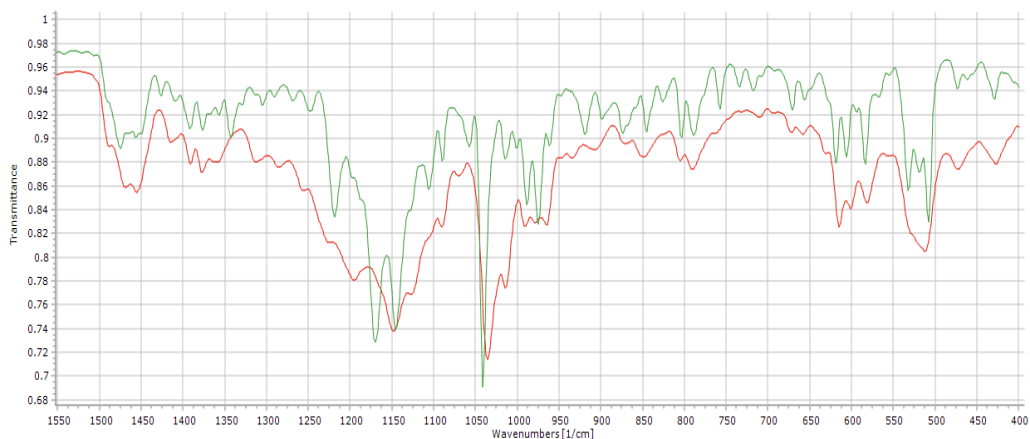


Figure 5.12: Fingerprint region from IR analysis. Red = amorphous sample, green = crystalline sample

5.3.2.5 SEM Analysis of Milled Samples

To probe any physical changes to the particles in the parent material and ball-milled samples, SEM images were collected for all samples. GSK2838232M parent material (see Figure 5.13), before any milling, consists of large crystalline particles with smaller crystalline material attached to the surface of the larger crystals.

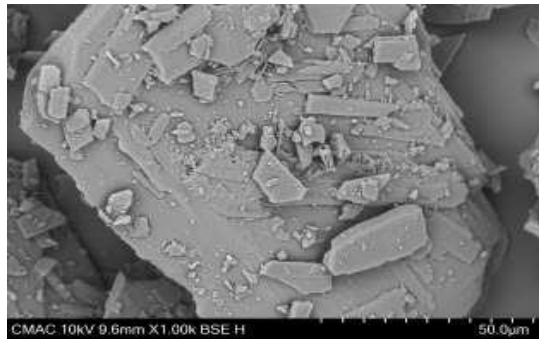


Figure 5.13: SEM image of GSK2838232M parent material. Scale bar indicated 50 µm

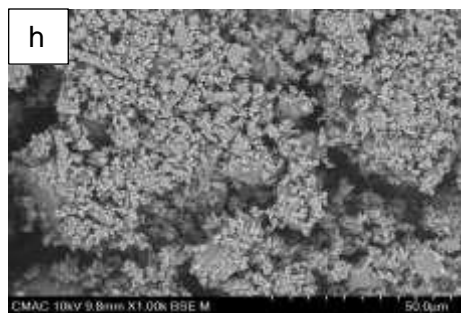
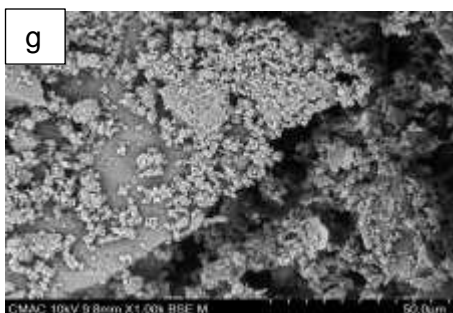
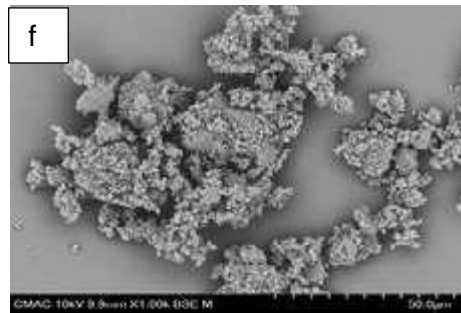
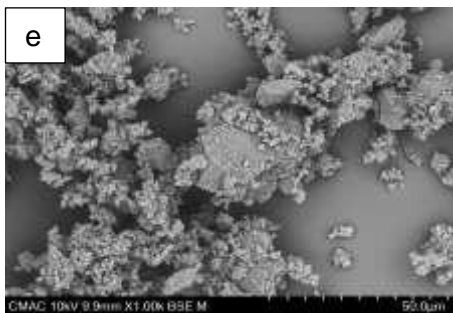
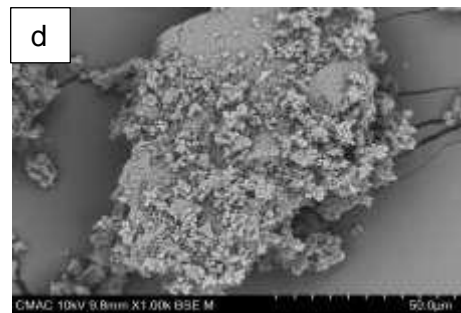
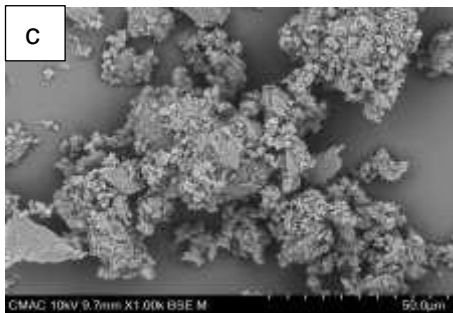
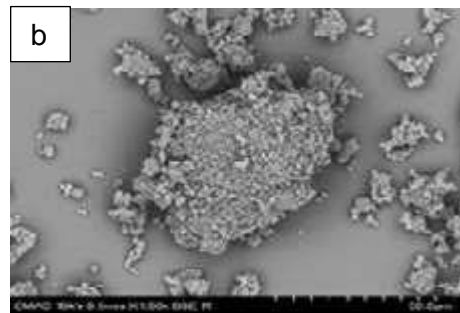
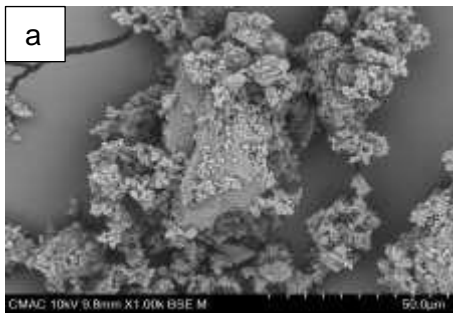


Figure 5.14: SEM images of milled samples, scale bar indicates 50 μm . a) 5 minute milled sample, b) 10 minute milled sample, c) 20-minute milled sample, d) 30-minute milled sample, e) 40-minute milled sample, f) 45 minute milled sample, g) 50-minute milled sample and h) 60 minute milled sample.

As the sample is milled for between 5 and 60 minutes with a milling frequency of 25 Hz the particle morphology shows larger particles that show faces and sharp edges consistent with crystalline material with smaller, potentially amorphous, powder like material attached to the surface. The larger particles can be seen to decrease in size as the milling time is increased (see Figure 5.14).

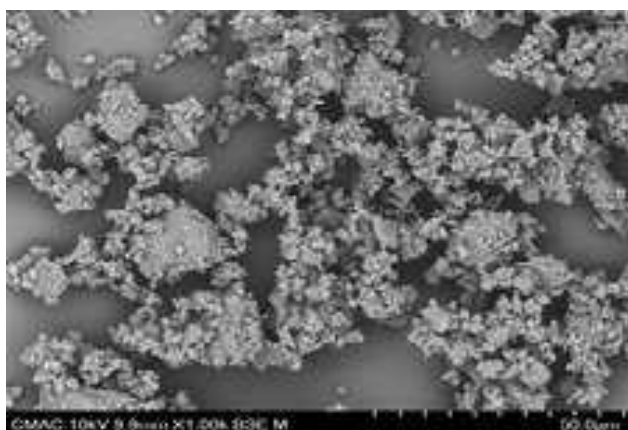


Figure 5.15: SEM image of X-ray amorphous material milled for 60 minutes at 30 Hz. Scale bar indicated 50 μm

By the final sample which was subject to harsher milling conditions (see section 5.2.1) the presence of larger particles is mostly gone, and the sample was more homogenous in appearance (see Figure 5.15).

5.3.2.6 Characterisation of Amorphous Samples Using SAXS

SAXS analysis was carried out on all samples to examine the ability of SAXS as a technique for studying amorphous pharmaceuticals using GSK2838232M samples as a case study. Previous techniques from this work provided a baseline characterisation of the amorphous nature of each of the raw materials and milled samples. All techniques show a crystalline starting material that trends to a lower crystalline content as milling time is increased. Initial SAXS experiments focused on method development to determine the best experimental parameters for analysing the samples. The parameters investigated included beam spot size, image time and mounting method to produce data with a good signal to noise while keeping analysis time to a minimum.

The samples were first analysed in a standard transmission powder sample holder as shown in Figure 5.16, which mounts the samples in a metallic washer sandwiched between two dots of sticky Kapton film as demonstrated in Figure 5.17.

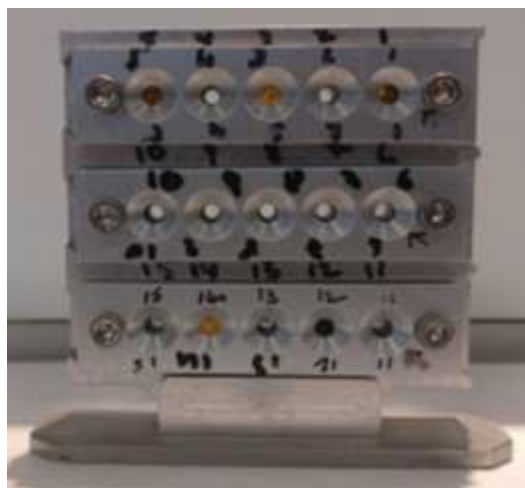


Figure 5.16: Multi-well SAXS powder transmission sample holder



Figure 5.17: Powder GSK2838232M sample mounted in metallic washer between sticky Kapton film.

Using this sample holder requires one background to be taken using a washer setup with the Kapton dots with no sample, this background is subtracted from all sample data. The background is taken in this way as it is not feasible to stick the Kapton dots to the washer for a background scan and then remove those specific Kapton dots to allow the sample to be loaded. The Kapton dots are easily damaged and any pulling or stretching can then impact the signal produced.

Three samples were analysed as follows using the same Kapton tape background. Three (different) washers were then loaded with the starting material. Each sample was scanned using the same experimental parameters, and the sample background was subtracted from the data collected. The three plots still varied significantly after background subtraction (Figure 5.18) indicating the lack of reproducibility for this mounting method.

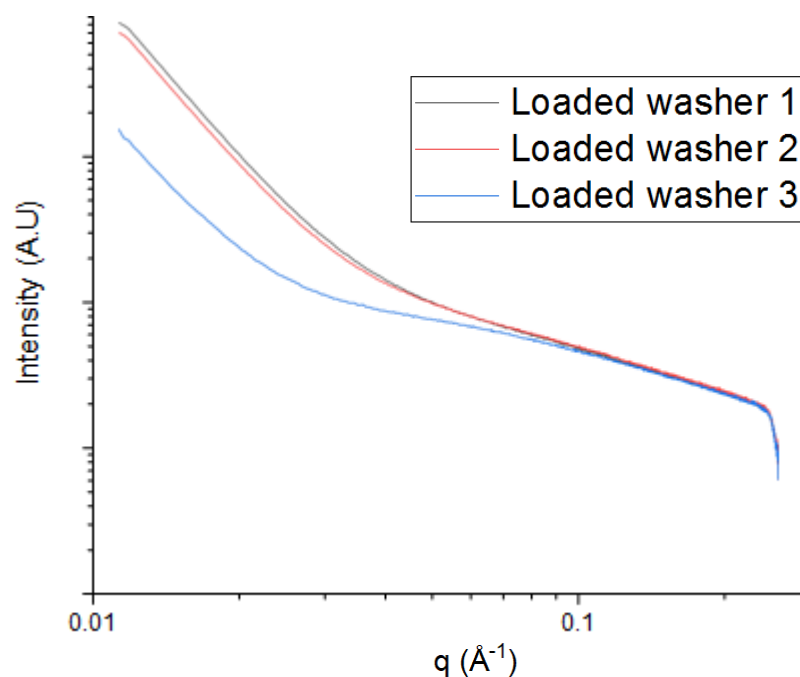


Figure 5.18: SAXS profiles of GSK2838232M mounted in three separate washers

To overcome this lack of reproducibility, an experimental set-up using a capillary sample holder as shown in Figure 5.19 was tested.

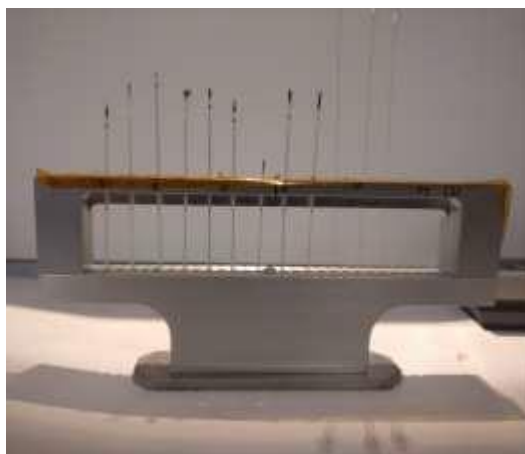


Figure 5.19: Multiple position glass capillary sample holder

Due to minor variations in glass thickness for individual capillaries, the capillary sample holder experimental set-up required a background to be collected for each capillary used. Therefore, each sample had a corresponding background subtracted for the capillary used. Apart from the different sample holders, the same experiment as above was performed, in that, the starting material was loaded into three separate capillaries, and all were analysed with the same experimental parameters. Samples were loaded into capillaries using similar methods to achieve a consistent sample packing density between samples. The results of which are shown in Figure 5.20.

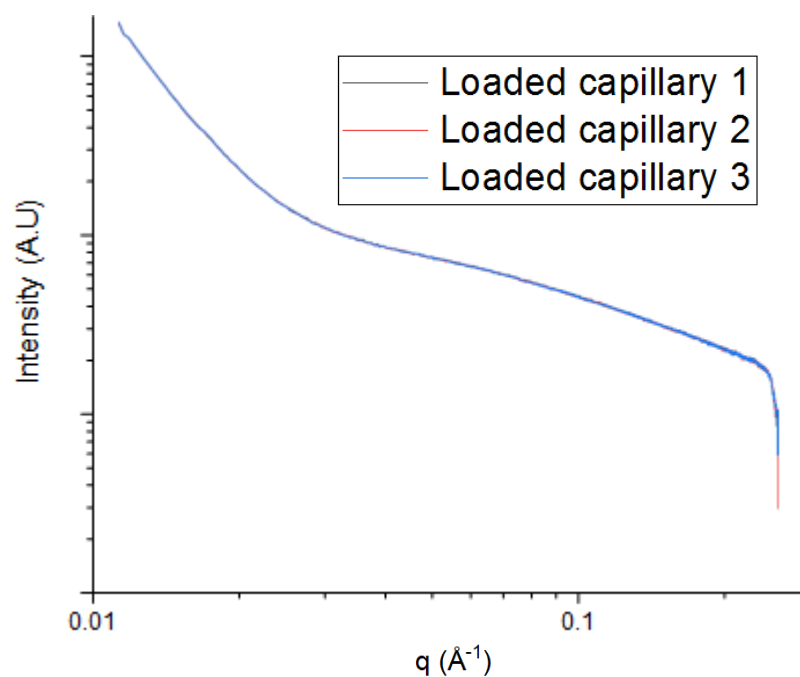


Figure 5.20: SAXS profiles of GSK2838232M mounted in three separate 0.7 mm borosilicate glass capillaries

As seen in the overlaid SAXS profiles in Figure 5.20, this experimental set-up resulted in significantly improved reproducibility when compared to the previous transmission powder washer sample holder. Consequently, the capillary sample holder was utilised for all experiments.

SAXS analysis from capillary samples was performed on all milled samples exhibiting differing amorphous content (Figure 5.21) as characterised previously by X-ray diffraction, DSC and SEM analysis.

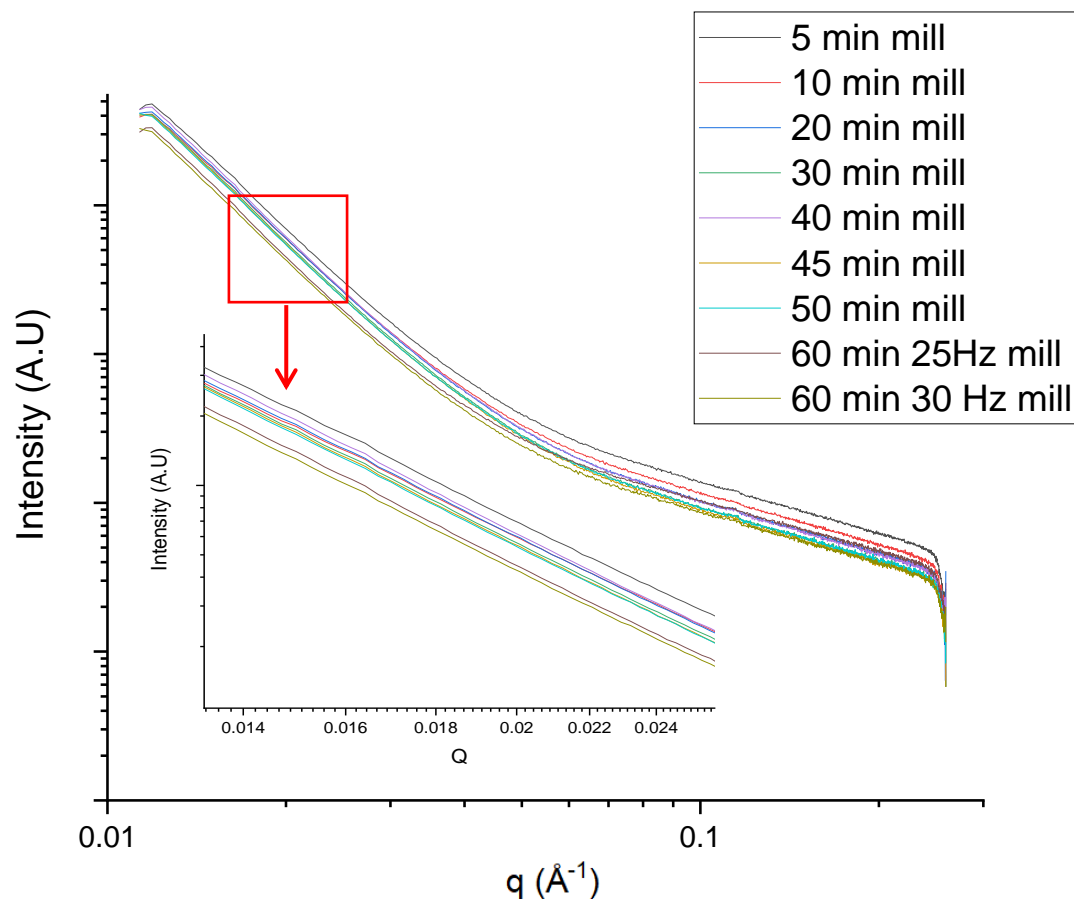


Figure 5.21: 1D SAXS data of milled GSK2838232M samples

The SAXS data presented here show an overall decrease in intensity across the whole scattering vector range ($0.012\text{-}0.26 \text{ \AA}^{-1}$) as milling time increases. This decrease indicated that the degree of nano-heterogeneity, a measure of density differences caused as a result of the mixed phase domains present in the sample, is decreasing as milling time and amorphous content increase. By contrast, the SAXS profiles remain very similar in overall shape as milling time increases. The similarity in profiles likely indicates that while the overall amorphous content of the sample is increasing, the small-scale local ordering is remaining similar to that of the original crystalline material.⁹³ Other amorphisation methods, such as melt-

quenching, may lead to greater changes in the profile shape as the local ordering is more impacted by the harsher processes.

As an indicator of overall nano-heterogeneity within the sample, the Porod invariant is used to quantify the density heterogeneity and the entropy of a system. This method has been used to study phase separation of elastomers,¹⁶⁸ to measure particle growth of amorphous materials in water¹⁶⁹ and generally as a means of analysing systems with multiple phases.¹⁷⁰ Porod's Invariant is calculated over all of the scattering range and is a more quantitative measure of the results when compared to simply looking at the individual profiles. The adequacy of Porod's invariant to provide information on multi-phase systems relies on a number of factors including the volume of both phases, the boundaries between the phases and the sharpness of these and also the size distribution of the domains.

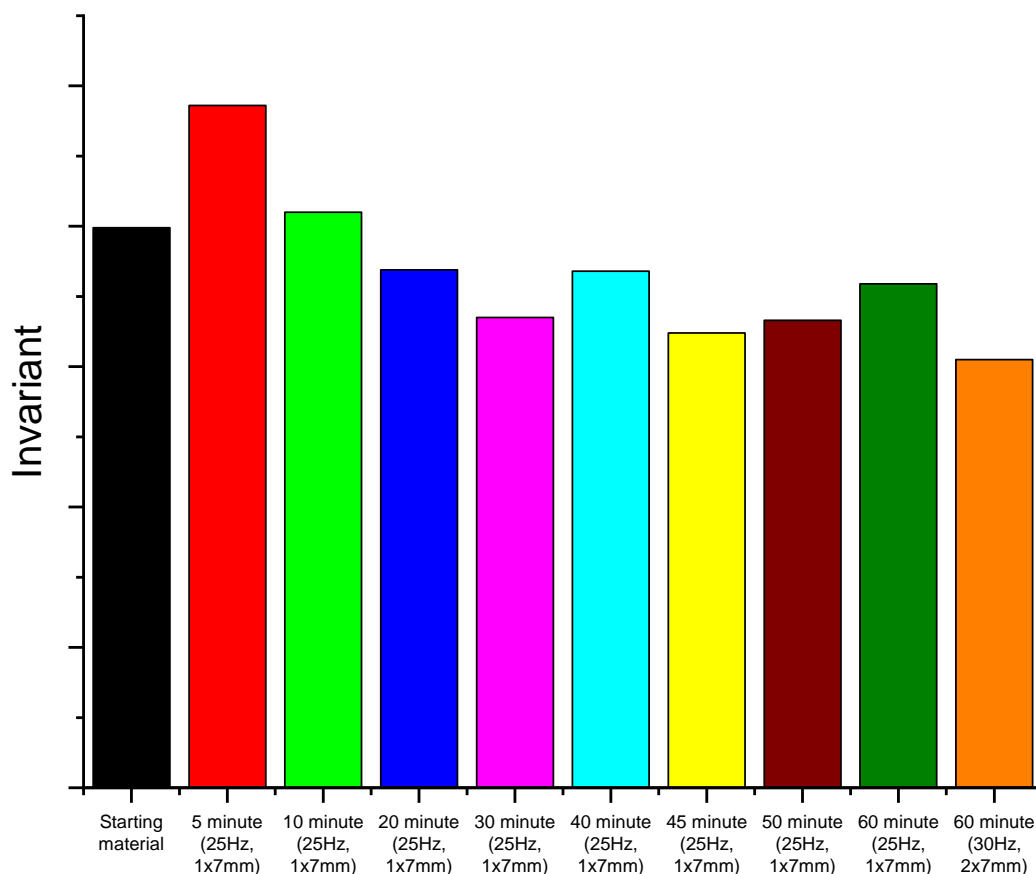


Figure 5.22: SAXS Porod invariant analysis of GSK2838232M and subsequent milled samples

The general trend that can be seen is a slight decrease in the invariant as milling time is increased (see Figure 5.22). This trend is consistent with an increase in the emergence of amorphous content and a decrease in heterogeneity.

There is an inconsistency between values at 40 to 60 minutes of milling time. This overlap may be a result of the technique not being sensitive enough to distinguish the small differences in amorphicity at these milling times. As only single measurements at each sample were taken no statistical differences can be measured for this result set. This lack of differentiation was also seen with the

crystallinity based on the DSC data. In those calculations, we saw the same inconsistency of values between 40-60 minutes, with the percent crystallinity almost plateauing at approximately 35%, until the milling frequency was increased resulting in a decrease to 7% crystallinity as measured by DSC.

SAXS as a technique has been used for the characterisation of various amorphous samples such as nanoparticles,¹⁷¹ silicon¹⁷² and polymers.¹⁷³ Data analysis methods vary between these samples, from simple intensity-based determinations coupled with knowledge of the density and structure of the system, where calculations can be performed to inform on fluctuations of a samples size by calculating the radius of particles. The concentration and radius of samples can be determined by integration of the intensity over reciprocal space, giving information on the weight % of different amorphous nanoparticles within a system. To the more complex computer modelling based data analysis where a wide range of information can be generated such as shape of voids within an amorphous solid. Computer modelling techniques can also be used to make *ab-initio* simulations as means of reconstructing inner shapes of materials based on their SAXS profiles. These data analysis techniques are designed to look at single phase amorphous systems, more work would be required to be able to fully implement these in multi-phase systems such as the ones studies in this work.

5.4 Summary

This work assessed the capability of SAXS as an analytical tool for characterising the amorphous form of the small organic molecule herein referred to as GSK2838232M. To assess SAXS the amorphous content of the samples was first measured by XRPD, DSC, TGA, FTIR and SEM. Ball milling of GSK2838232M using a Retsch MM400 ball mill produced a range of samples with

an amorphous content from roughly 3% (5-minute milling at 25 Hz) to 93% (60-minute milling at 30 Hz) as determined by DSC. XRPD was used to determine the crystalline nature of the starting material and resulting ball milled samples, with all samples showing peaks consistent with crystalline material until the sample had been milled for 60 minutes. At this point no peaks were present, indicating a fully X-ray amorphous sample had been produced. TGA analysis was able to demonstrate a general trend of increasing mass loss as a result of increased milling time, this is consistent with an increased surface area with increased amorphous content allowing for more surface water on the molecule to then be lost during the TGA analysis. FTIR spectra for all samples contained the same peaks indicating no degradation took place during the amorphisation of the samples, general peak broadening was observed in the amorphous samples when compared with the crystalline starting material. This is expected in amorphous samples due to the weakening of the interactions within the molecule. All techniques showed agreement in the overall trend of amorphous content increasing as a result of increased milling time. Method development for SAXS analysis of GSK2838232M highlighted the importance of the sample mounting method and appropriate background subtraction. This work found the best reproducibility was gained using borosilicate capillaries with a background subtraction for the corresponding capillary.

SAXS was shown to display consistent changes in the measured signal as a function of the process history of the sample providing a qualitative tool for the analysis of solid samples of small organic molecules. Differences observed in SAXS intensities can be related to decreasing heterogeneity, as the sample trends to more amorphous content and the density differences become less with fewer boundaries between the two phases. These differences can give insight into the

nano-structural changes between crystalline and amorphous forms. Using the Porod invariant allows for a more quantitative measure of the nano-heterogeneity by measuring the density fluctuations at the nano-scale, this was found to fluctuate with the length of milling the sample was exposed to. The precision of the values obtained requires further investigation as all data was produced based on one sample at each milling condition, additional samples would allow for statistical differences to be measured to confirm the values obtained.

Data interpretation of SAXS is informed by complementary methods thus uncertainties about particle sizes and shapes within a system can inhibit analysis. Due to this, SAXS is routinely used in conjunction with other techniques as was done here but is not currently able to be used as a standalone analysis technique for amorphous pharmaceuticals. Other techniques commonly used alongside SAXS are NMR, circular dichroism (CD), size exclusion chromatography (SEC) and dynamic light scattering (DLS).^{42,43,44,45} Another technique gaining interest in being used as a complementary technique to use with SAXS is pair distribution function analysis. This method of analysis could be used as a complementary technique to SAXS, thereby providing additional structural information to be fed into SAXS models for these amorphous pharmaceutical systems.¹⁷⁸

Further work could investigate using a different route to produce the amorphous material. Alternate preparation methods could have different effects on the underlying structure of the material. As the Porod invariant uses volume and size of domain differences along with the sharpness of the boundaries between the phases, other methods of amorphisation could be used to make these more pronounced to hopefully result in greater differences in the SAXS patterns obtained. More work on the data analysis could be investigated to hopefully allow for further structural data to be obtained from the SAXS data.

**Chapter 6: Wide Angle X-ray Scattering for the Analysis
of Crystallinity and Orientation of Biocomposite
Fibres and Films of Microfibrillated and
Nanofibrillated Cellulose Produced from Potato
Pulp**

6.1 Introduction

Cellulose is an abundant natural biopolymer that is widely researched owing to its suitability to be used in many fields such as pharmaceuticals, textiles,²⁶ food¹⁷⁹ and electronics.¹⁸⁰ It is also a biodegradable and renewable substance which has increased research efforts as a sustainable alternative for a variety of materials such as thin films and composites.^{181,182} Cellulose exists as both amorphous and crystalline regions, with hydrolysis methods used to extract the crystalline material to form cellulose nanocrystals (CNC).

Cellulose can be sourced from a range of raw materials including wood,¹⁸³ agricultural waste,¹⁸⁴ and a variety of fruit and vegetables such as potato,¹⁸⁵ bananas,¹⁸⁶ rice husk¹⁸⁷ and cotton fibres.¹⁸⁸ microfibrillated cellulose (MFC) and nanofibrillated cellulose (NFC) are terms used based on the fibrillation process followed when producing fibrils from cellulose. The extraction process will affect the properties of the MFC or NFC produced.

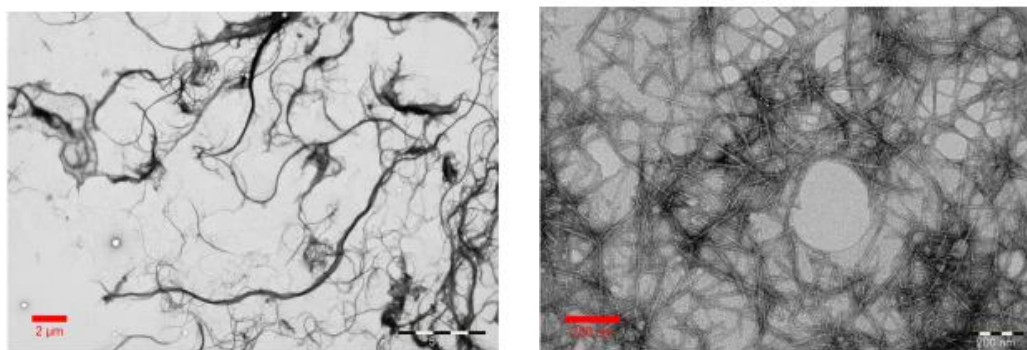


Figure 6.1: Transmission Electron Microscopy (TEM) images of MFC (left) and NFC (right)¹⁸⁹

Various pretreatment steps can be performed during the extraction process in an attempt to improve the mechanical properties of the cellulose biomaterial by

increasing the crystallinity and orientation of these crystals to improve overall strength.

Much of the interest in cellulose has centred around the biomaterials MFC and NFC due to the wide range of interesting properties associated with these materials. These properties include dimensional stability, high surface area and aspect ratio, and the ability to be chemically modified.^{12,13,14,15} CNC have excellent mechanical strength, however, due to their anisotropic nature, the strength of cellulose varies significantly based on the orientation. In the direction of the crystalline material, values of the Young's Modulus between 100 and 160 GPa can be achieved while in the opposite direction this is much lower with results ranging between 18-50 GPa.^{194,195} To be able to take advantage of this material's mechanical properties the orientation of the material must be controlled; this can be achieved via the production technique.

Commonly, extrusion and spinning techniques have been employed in the production of these materials to impart alignment of the fibrillated cellulose.^{196,197} To be able to produce fibres at an industrial scale, a continuous spinning process is required. However, cellulose, by itself, is unable to be processed using a continuous spinning method. In this work, sodium alginate was used as a carrier polymer to allow the cellulose fibres to be spun. Due to alginate possessing a similar structure to cellulose, it is predicted that the two will form a good connection with ionic cross-linking. The combination of sodium alginate with cellulose allowed for a wet spinning technique to be employed in this work.

WAXS is one of the most commonly applied techniques for analysing crystallinity within cellulose samples, this is due to the relative simplicity of the method combined with the ability to produce defined Bragg peaks from a crystalline material.

SAXS is a technique which has found application in the analysis of cellulose containing materials. Typically SAXS is used to determine the length scale and orientation of fibrils within cellulose and also the effect of various solvents on the structure. As this work is aiming to explore the orientation and degree of crystallinity of cellulose, SAXS was not used during this study, however, the implementation of SAXS could allow for more information to be gathered around the sizes and shapes of the crystalline fibril domains within the film and fibre samples.

The focus of this chapter is to characterise the crystallinity and orientation of both nano and microfibrillated cellulose films and fibres using WAXS as the characterisation tool. Comparisons of films and fibres along with fibres that were then subjected to stretching in an attempt to increase the mechanical strength were conducted.

6.2 Materials and Methods

6.2.1 Preparation of Alginate and Cellulose Fibres and Films

Pre-treatment of the potato pulp was performed with 0.5 M sodium hydroxide and sodium chlorite 1.0% v/v for MFC and for NFC 0.8% v/v sodium hypochlorite and 0.2 M sodium acetate was used for pre-treatment. The pre-treated pulp was then circulated in a microfluidizer for 18 minutes until a thick gel was formed. MFC and NFC fibres were produced from these thick gels via wet-spinning at room temperature. Before spinning the formulations, fibres were homogenised in water at 15000 rpm and degassed using a vacuum pump. These solutions were then extruded through a conical needle at a spinning rate of 5 mL/min, spun into a calcium chloride bath (5% w/v) and then collected in a wind-up drum. The fibres

were then removed from the drum and left in the calcium chloride bath overnight. Afterwards, the samples were then transferred to a water bath for 24 hours to remove any excess calcium chloride from the fibres. The final step was to place the fibres in an acetone bath for two hours and then dry them on a metal plate. The apparatus used is shown in Figure 6.2.

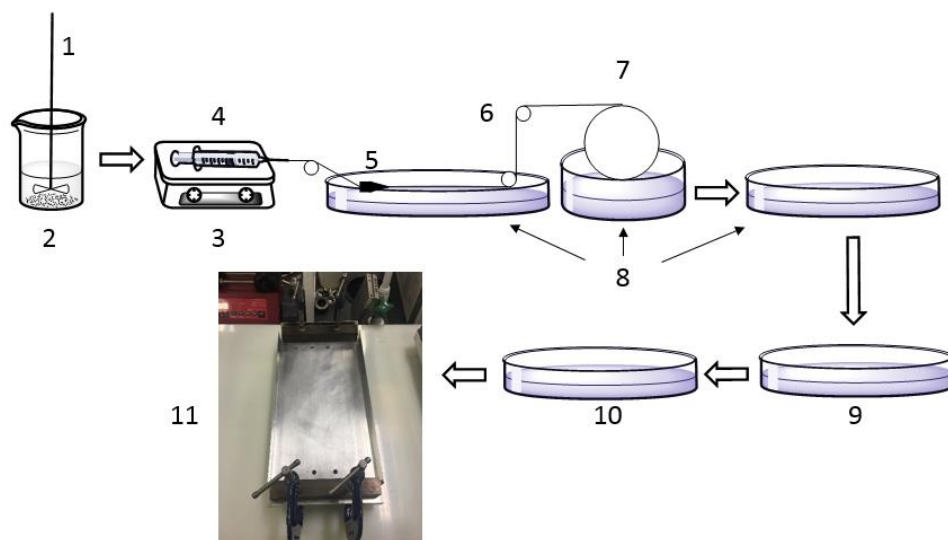


Figure 6.2: Schematic diagram of the fibre production process: 1- Ultra Turrax; 2- mixing beaker; 3- syringe pump; 4- syringe; 5- conical needle; 6- roller; 7- wind-up drum; 8- coagulation bath; 9- rinsing bath; 10- solvent exchange bath; 11- drying rack.

Film samples were simply produced by casting the solutions in glass Petri dishes and allowing them to dry. Images of mounted fibre and film samples are shown in Figure 6.3.

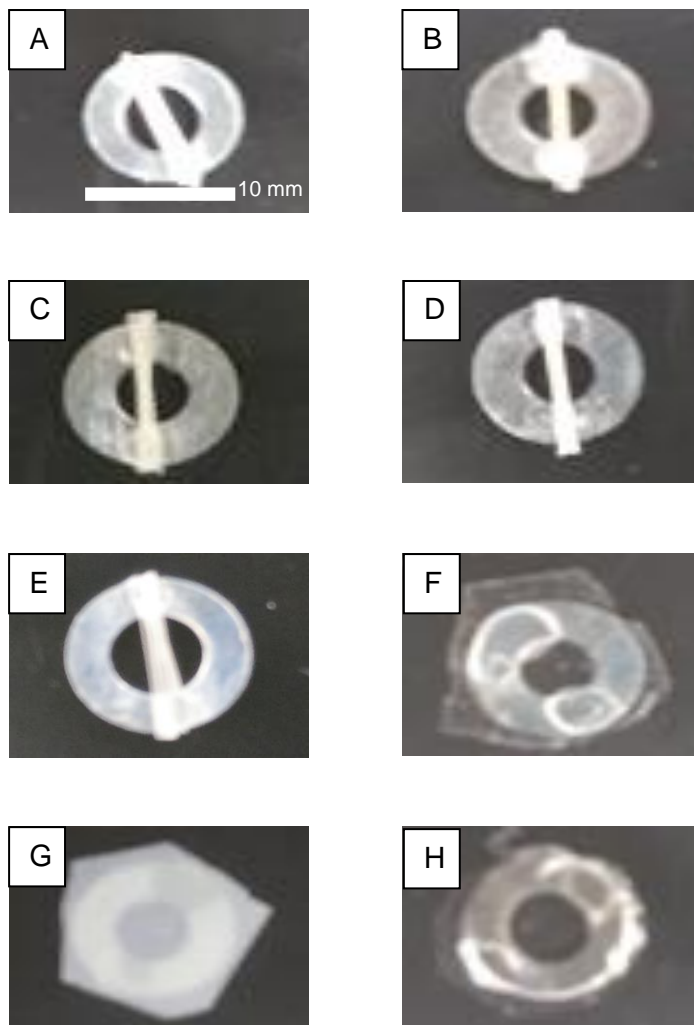


Figure 6.3: Mounted Fibre and film cellulose samples. A) Pure alginate fibres B) Post stretched alginate fibres C) Microfibrillated cellulose fibres D) Post stretched microfibrillated cellulose fibres E) Nanofibrillated cellulose fibres F) Pure alginate film G) Microfibrillated cellulose Film H) Nanofibrillated cellulose film. Samples mounted in 10 mm diameter washers

6.2.1.1 Capillary X-Ray Powder Diffraction

Powdered sodium alginate was characterised using capillary powder diffraction to determine whether any peaks occur which could interfere with those of cellulose. Samples were analysed using a Bruker D8 Advance II capillary diffractometer as described in section 3.2.2.3. A small amount of sample (10-50 mg) was packed into a 0.7 mm borosilicate capillary and scanned in the range of 5-80° two theta with a step size of 0.017° with a 4 s/step count time.

6.2.1.2 Wide Angle X-ray Scattering

The crystallinity index (CrI) and orientation index (f_c) of the cast films and spun fibres were calculated from WAXS data obtained from a Xenocs Xeuss 2.0 SAXS/WAXS laboratory beamline (Xenocs, Grenoble) as described in section 3.2.2.2. 2D patterns were collected on a Pilatus 1M area detector (DECTRIS, Belgium) positioned 171.6 mm from the sample, which was calibrated using silver behenate and silicon standards. Film samples were exposed for 10 hours total, due to the thinness of the material requiring a longer exposure for an increased signal to the detector, while fibre samples were exposed for 2 hours total. Data was normalised for transmitted intensity, and radial integration was performed for 360° of the collected images using Foxtrot data reduction software (Version 3.4.9, Xenocs, Grenoble), and presented as a 1D diffraction pattern for further calculations.

Crystallinity index (CrI) was calculated for all samples using two methods, firstly Segal's method¹⁹⁸ according to Eqn 6.1:

$$CrI = \left(\frac{I_{(200)} - I_a}{I_{(200)}} \right) \times 100 \quad \text{Eqn 6.1}$$

where $I_{(200)}$ and I_a are the intensity of the 200 reflection peak and the amorphous peak respectively.

CrI was also calculated using Bruker EVA software (Version 18.0.0.0, Bruker, USA) via a deconvolution method to separate the crystalline contributions from the amorphous contributions using Eqn 6.2 and Eqn 6.3:

$$\% \text{ Amorphous} = \left(\frac{\text{Global Area} - \text{Reduced Area}}{\text{Global Area}} \right) \times 100 \quad \text{Eqn 6.2}$$

$$\% \text{ Crystallinity} = 100 - \% \text{ Amorphous} \quad \text{Eqn 6.3}$$

The degree of nanofibre orientation (f_c) was evaluated using the orientation index of the cellulose crystals using Eqn 6.4, utilising azimuthal breadth analysis.^{22,199,200,201}

$$f_c = \frac{(180^\circ - \beta_c)}{180^\circ} \quad \text{Eqn 6.4}$$

where β_c is the full width at half maximum of the 200 reflections in the diffractograms.

6.3 Results and Discussion

6.3.1 Raw materials

Sodium alginate is used as a polymeric carrier that links to the cellulose via ionic crosslinking, thus giving the cellulose strength to be continuously spun. The sodium alginate powder used was derived from marine algae and was characterised using capillary XRPD. This reference pattern enabled the identification of peaks that might interfere with the patterns obtained from the cellulose materials (see Figure 6.4).

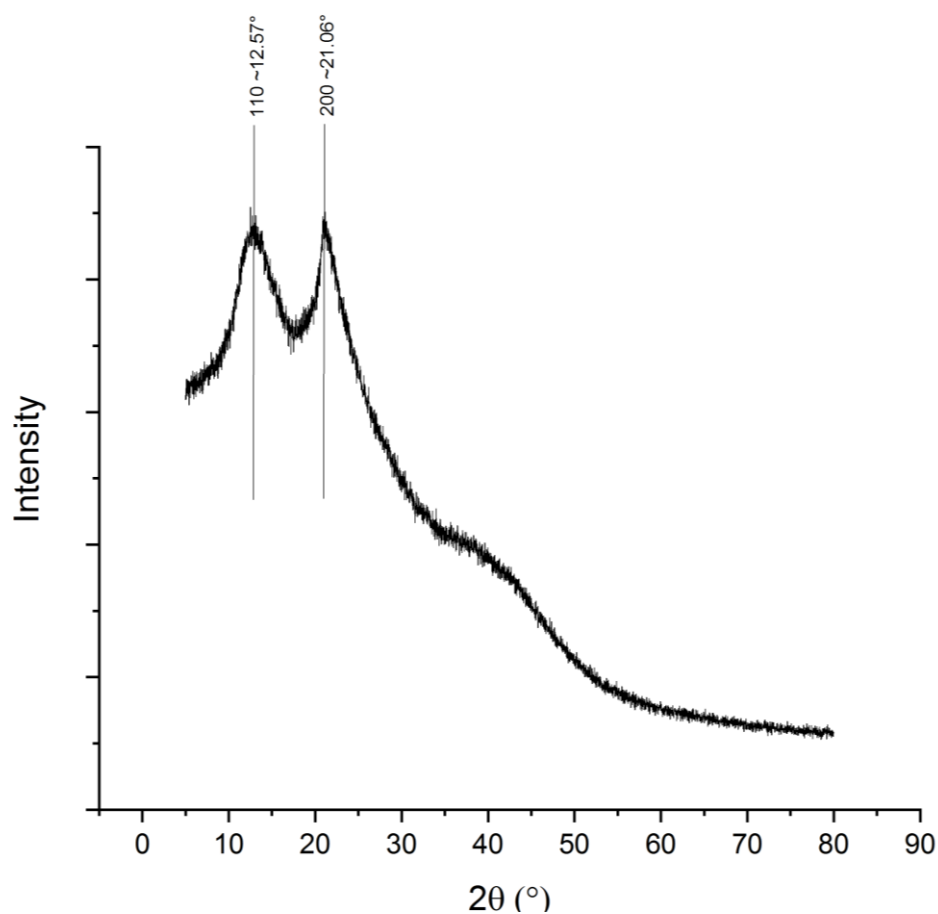


Figure 6.4: Capillary XRPD data of sodium alginate powder derived from brown algae, in the range of 5-80° two theta

The sodium alginate raw material showed a characteristic semi-crystalline profile,²⁰² with two broad peaks at 12.57° and 21.06° two theta and an amorphous hump occurring at approximately 35-45° two theta.

6.4 WAXS Analysis of Cellulose Fibre and Film Samples

6.4.1 Pure Alginate Fibres in the Absence of Cellulose

As alginate was used as a polymer carrier for the cellulose, a sample of alginate, in the absence of cellulose, was spun into a fibre and analysed to understand the crystallinity and orientation which may come as a result of the alginate in the cellulose samples.

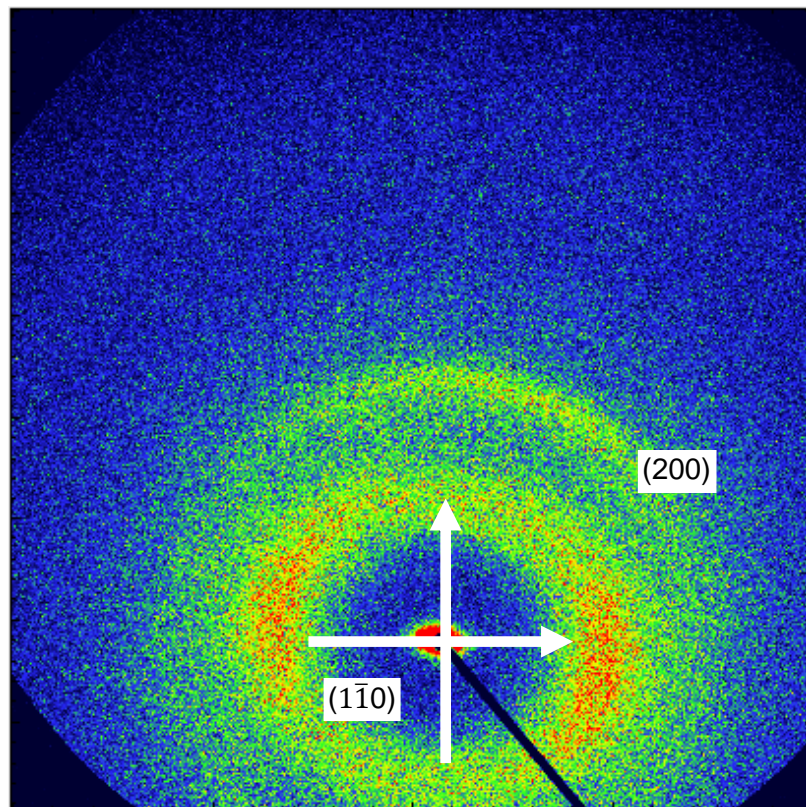


Figure 6.5: 2D detector image of pure alginate fibre in the absence of cellulose. Arrows depict the direction of integration. Arrow in the horizontal direction shows integration perpendicular to the alignment of the fibres. Arrow in the vertical direction shows integration parallel to the alignment of the fibres. Samples mounted as described in section 6.2.1.2 and data integration as described in section 6.2.1.2.

From the detector image, two scattering rings have been observed. Both rings have a distinct orientation as indicated by more intense scattering in the vertical direction (see Figure 6.5) for the outer ring and the horizontal direction for the inner ring. An azimuthal integration over the whole two theta range produced a 1D plot (see Figure 6.6) showing peaks for both rings, with the amorphous portion

of alginate spread across the pattern most clearly seen at approximately 30-45° two theta.²⁰³

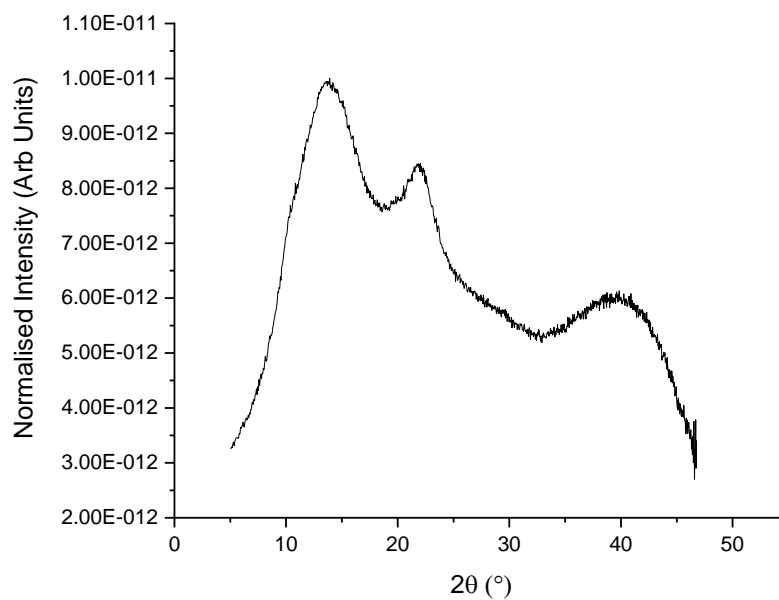


Figure 6.6: 1D WAXS data of pure alginate fibres from integrated 2D image

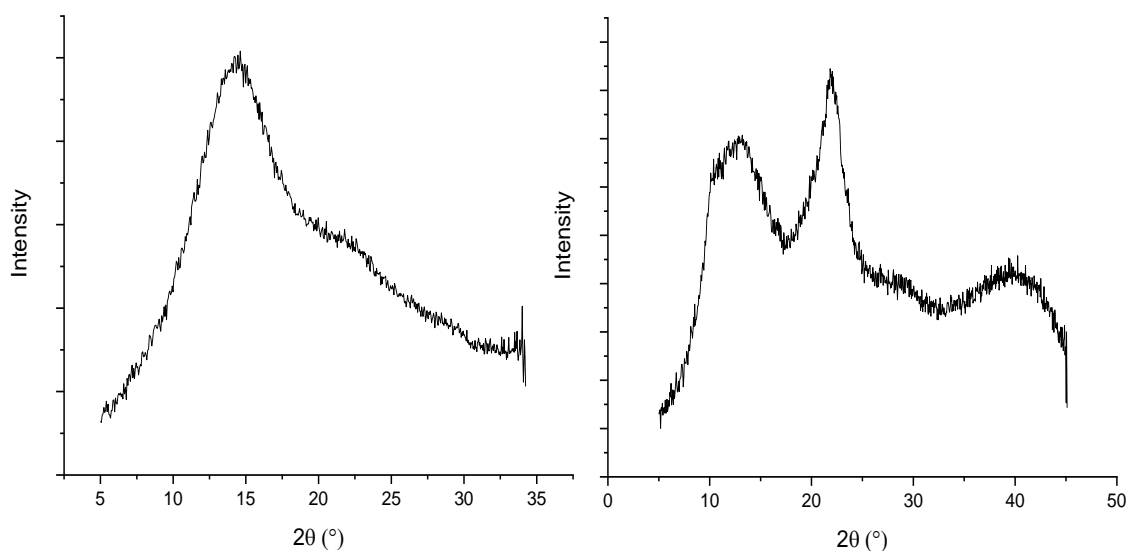


Figure 6.7: Integration of WAXS data for pure alginate fibres, perpendicular (left) and parallel (right) to the direction of the mounted fibre

The detector image also shows an orientation effect of the crystallisation of the first scattering ring, with a much higher intensity seen in the horizontal direction. Azimuthal integrations were performed at 0° (perpendicular to the fibres mounted position) and 90° (parallel to the fibres mounted position) and shown in Figure 6.6 to determine the orientation of the scattering.

6.4.2 Stretched Alginate Fibres

The alginate fibres, in the absence of cellulose, were then stretched to see what effect this would have on the orientation and crystallisation of the alginate sample.

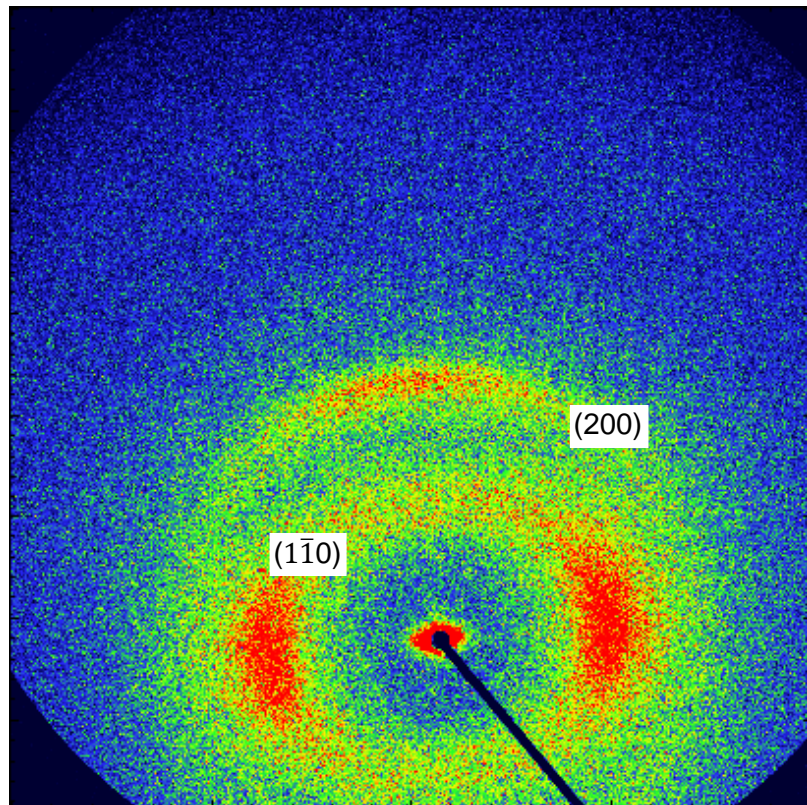


Figure 6.8: 2D detector image of pure alginate fibres, which had been subjected to stretching after spinning

The detector image for the stretched sample is very similar to that of the unstretched sample (see Figure 6.8). However, it appears to be more crystalline due to the more intense scattering seen from both rings. An azimuthal integration over the whole two theta range produced a 1D plot (see Figure 6.9) showing peaks for both rings, with an amorphous halo present at approximately 35-45° two theta.

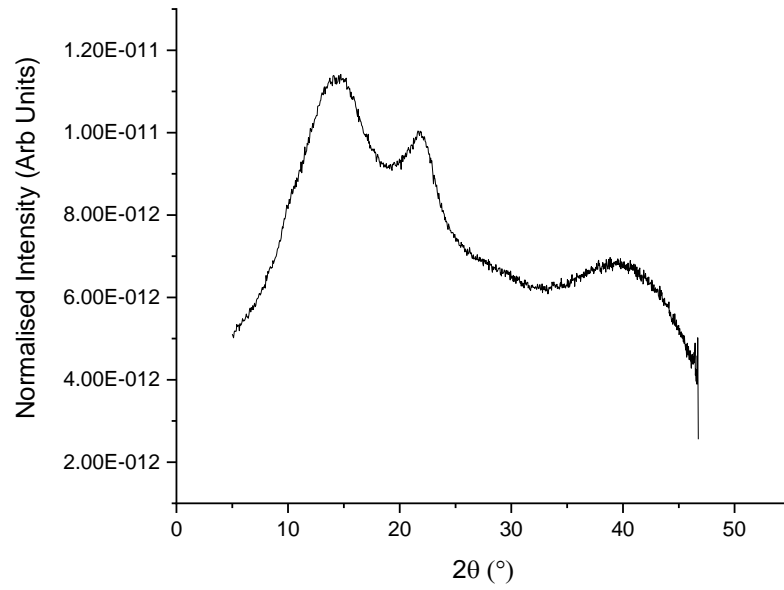


Figure 6.9: 1D WAXS data from integrated 2D image of pure alginate fibres which have been subject to stretching after spinning

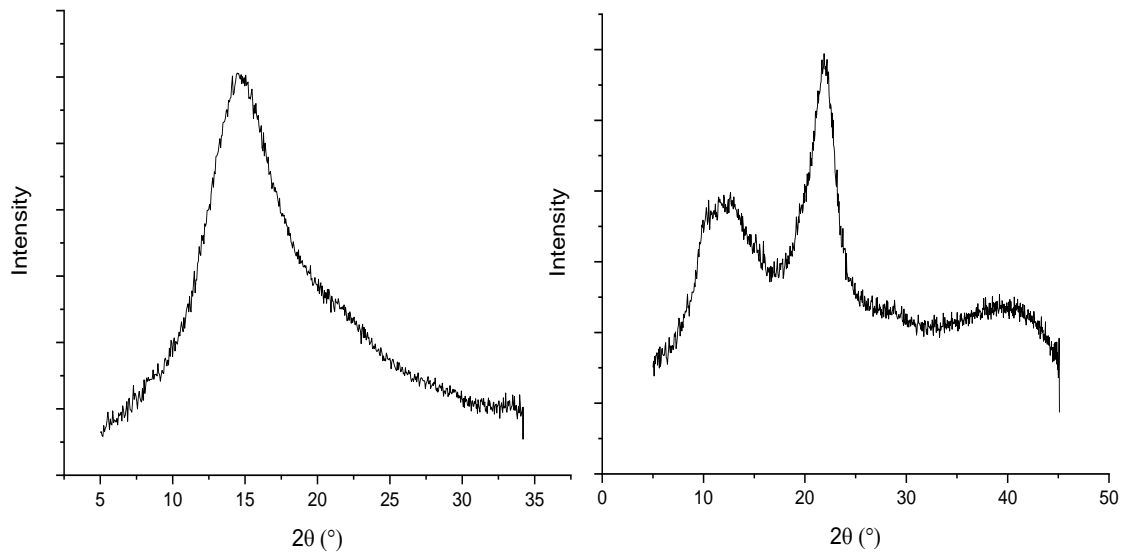


Figure 6.10: Integration of WAXS data for pure alginate fibres which have been stretched after spinning, perpendicular (left) and parallel (right) to the direction of the mounted fibre

The detector image also shows an orientation effect of the crystallisation of the first scattering ring, with a much higher intensity seen in the horizontal direction consistent with the initial alginate sample but more intense. Azimuthal integrations were performed at 0° (perpendicular to the fibres mounted position) and 90° (parallel to the fibres mounted position) and shown in Figure 6.10 to determine the orientation of the scattering.

6.4.3 Microfibrillated Cellulose Fibres

Fibres consisting of microfibrillated cellulose contained several characteristic diffraction rings which are expected from cellulose-containing material as shown in Figure 6.11.

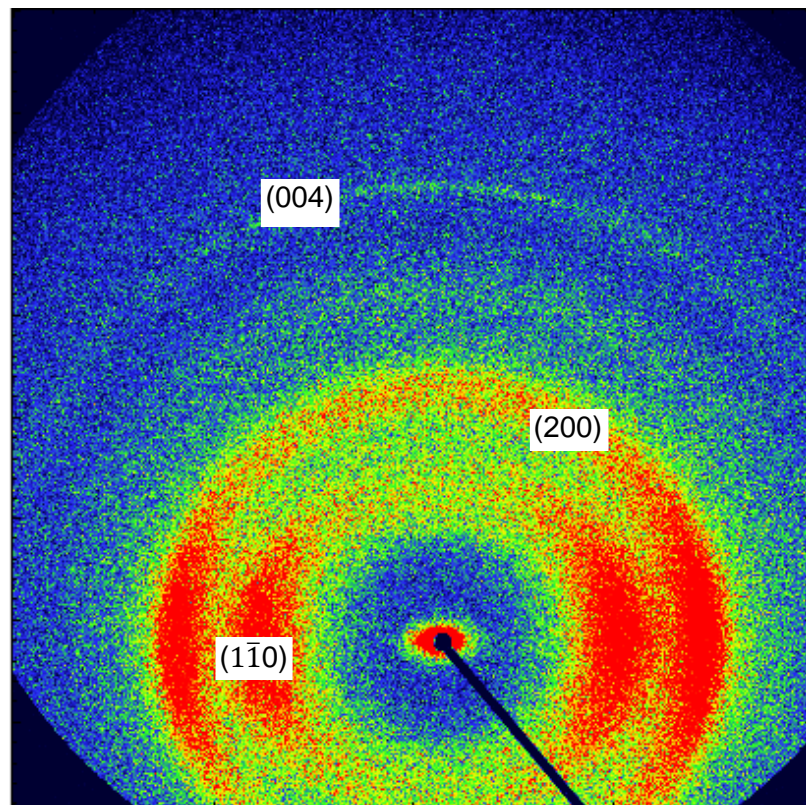


Figure 6.11: 2D detector image of microfibrillated cellulose fibres labelled with reflections of the most intense peaks associated with cellulose

As seen in the detector image, the presence of four diffraction rings indicates a relatively crystalline sample. An azimuthal integration over the whole two theta range produced a 1D plot (see Figure 6.12) showing distinct peaks for the three labelled rings.

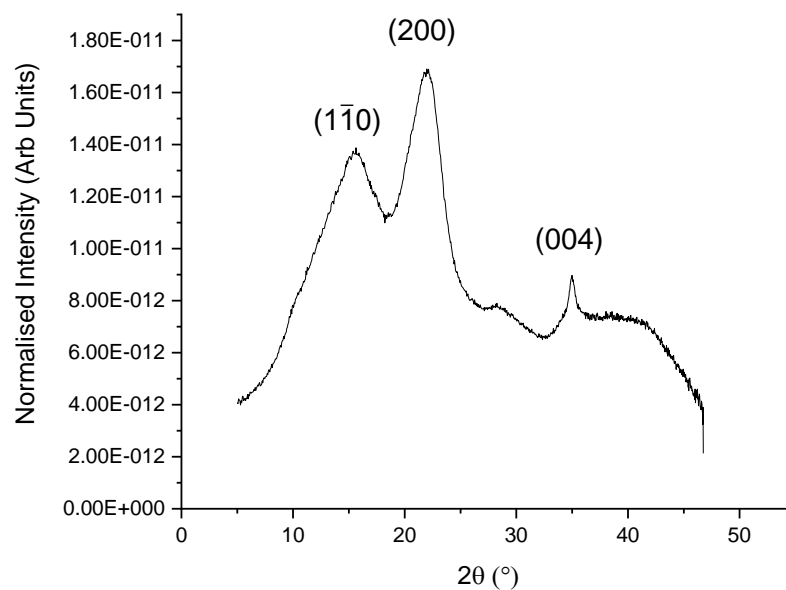


Figure 6.12: 1D WAXS data from integrated 2D image of microfibrillated cellulose fibres labelled with reflections of the most intense peaks associated with cellulose

The detector image also shows an orientation effect of the crystallisation, with a much higher intensity seen in the horizontal direction for the $1\bar{1}0$ and 200 reflections. Although crystalline and amorphous material can be seen in all directions within the fibre, the stronger intensity of the diffraction rings shows a greater crystalline contribution in one direction. Azimuthal integrations were performed at 0° (perpendicular to the fibres mounted position) and 90° (parallel to

the fibres mounted position) and shown in Figure 6.13 to determine which reflections are orientated and in which direction.

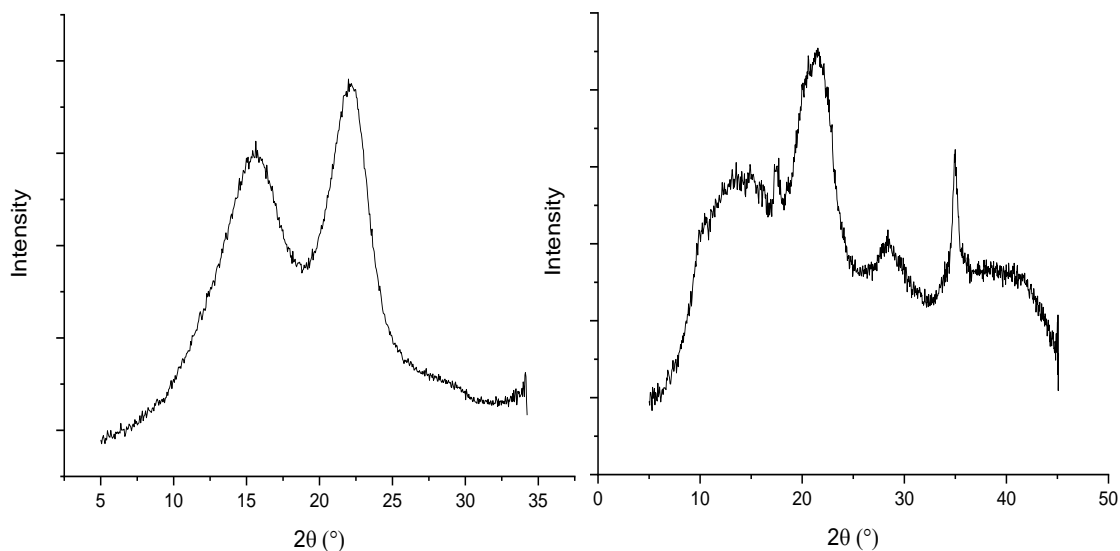


Figure 6.13: Integration of WAXS data for microfibrillated cellulose fibres perpendicular (left) and parallel (right) to the direction of the mounted fibre.

It was seen that both the $1\bar{1}0$ and 200 reflections were observed in the perpendicular integration, while in the parallel integration a much smaller contribution was seen from the $1\bar{1}0$ reflection in this orientation. More reflections can be seen contributing to the overall crystallinity of the sample in the parallel direction. Due to detector limitations, these rings can be seen in the parallel direction as the detector has a greater surface area parallel to the fibre orientation, thus allowing for these rings to be captured only in this direction with this experimental setup.

6.4.4 Stretched Microfibrillated Cellulose fibres

Fibres from the same batch as section 6.4.3 were taken and stretched with the object of analysing the effect the stretching would have on the crystallinity, and more importantly the orientation of the cellulose.

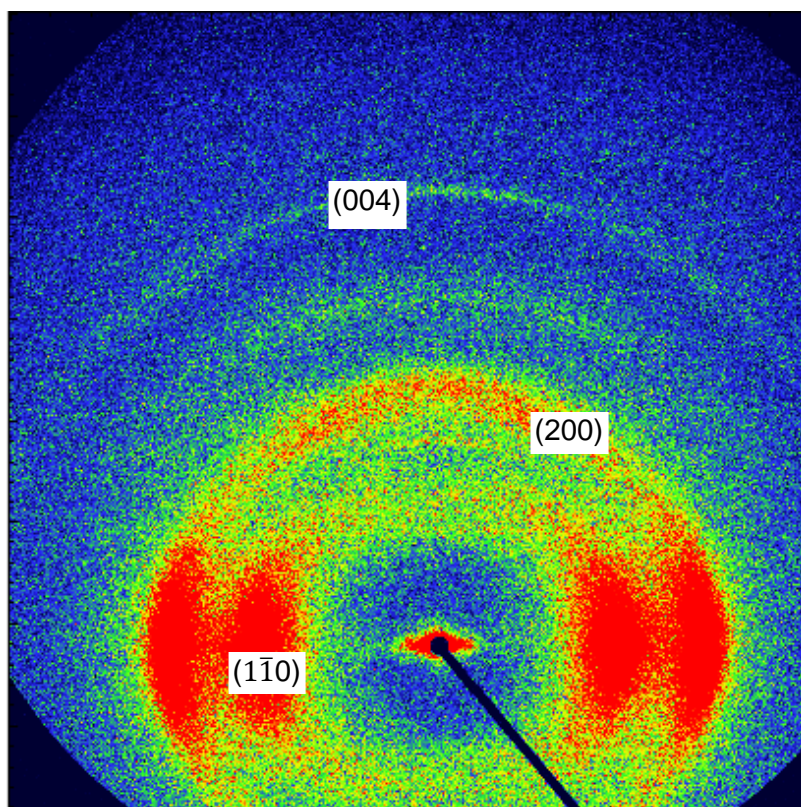


Figure 6.14: 2D detector image of microfibrillated cellulose fibres which have been subject to stretching after spinning

The raw detector image shows a scattering profile similar to the MFC fibres which have not been stretched. However, the intensity of scattering when compared to the unstretched MFC sample appears to be greater perpendicular to the fibre. When compared to the images collected from unstretched samples (see Figure 6.11) there is a clear increase in the intensity. An azimuthal integration over the

whole two theta range produced a 1D scattering plot demonstrating the contributions of the $1\bar{1}0$, 200 and 004 reflections associated with cellulose (see Figure 6.15).

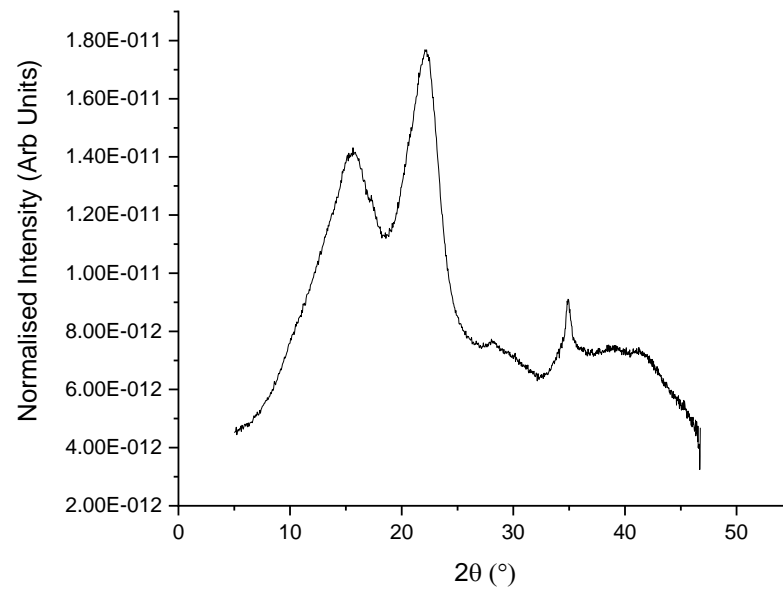


Figure 6.15: 1D WAXS data of microfibrillated cellulose fibres which have been subject to stretching after spinning from integrated 2D image

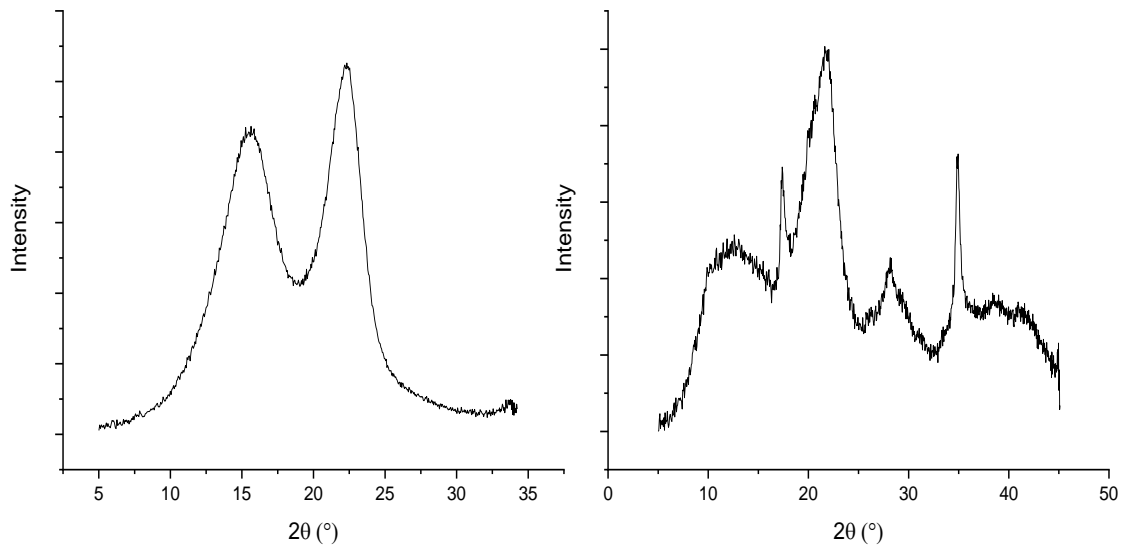


Figure 6.16: Integration of WAXS data for microfibrillated cellulose fibres which have been subject to stretching after spinning, perpendicular (left) and parallel (right) to the direction of the mounted fibre

As before with the non-stretched MFC fibres, both the $1\bar{1}0$ and 200 reflections contribute to the perpendicular direction (see Figure 6.16). While in the parallel direction more contributions are seen from the 110, $1\bar{1}0$, 200 and 004 reflections associated with cellulose, from the raw detector image it is clear that there is a distinct orientation effect in the perpendicular direction of the $1\bar{1}0$ and 200 reflections. The increase in orientation is associated with an alignment of the cellulose nanocrystals within the fibre as a result of the stretching process. The alignment of the cellulose nanocrystals will allow for a greater extent of hydrogen bonding due to the greater density of cellulose nanocrystals within a smaller area. This increase in orientation and hydrogen bonding is likely to be accompanied by an increase in the mechanical properties of the fibres.

6.4.5 Nanofibrillated Cellulose Fibres

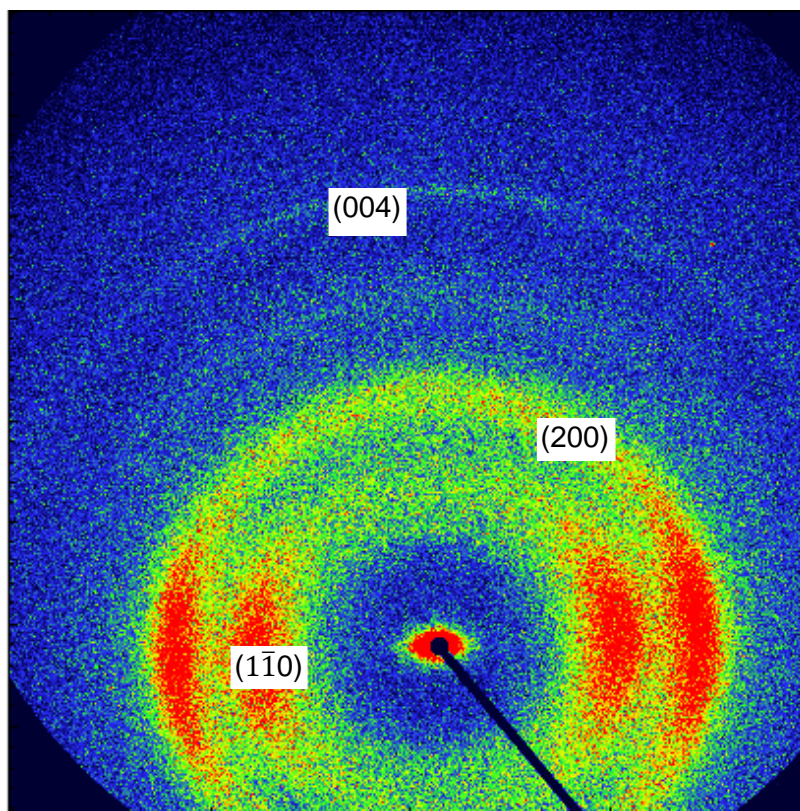


Figure 6.17: 2D detector image of nanofibrillated cellulose fibres

Scattering observed in the raw detector image shows intensity associated with the $1\bar{1}0$, 200 and 004 reflections. There is significant orientation observed in the $1\bar{1}0$ and 200 reflections in the perpendicular direction. From a simple visual inspection of the MFC (Figure 6.11) and NFC (Figure 6.17) detector images, there appears to be little difference in the scattering intensity and therefore overall crystallinity of the samples. An azimuthal integration over the whole two theta range was performed to produce a 1D scattering plot. From the plot (Figure 6.18) we can see definite contributions from the $1\bar{1}0$, 200 and 004 reflections associated with cellulose.

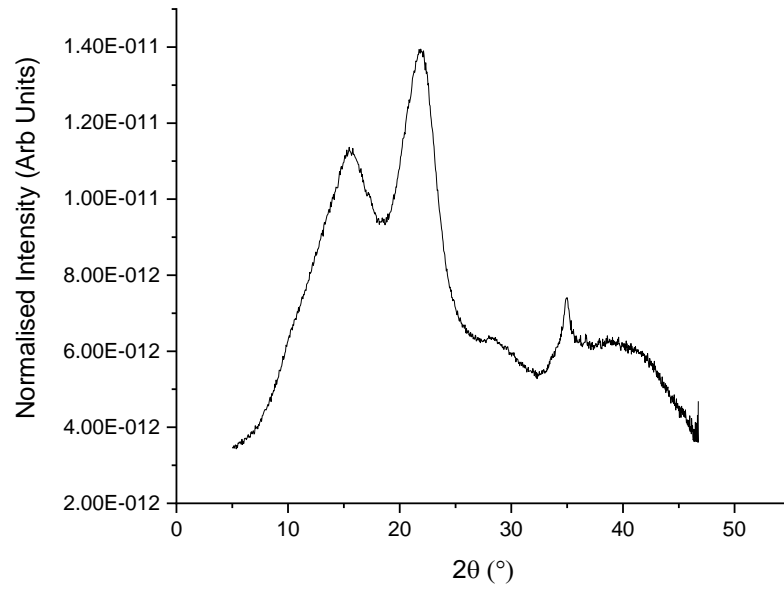


Figure 6.18: 1D azimuthal integration plot of nanofibrillated cellulose fibres from integrated 2D image

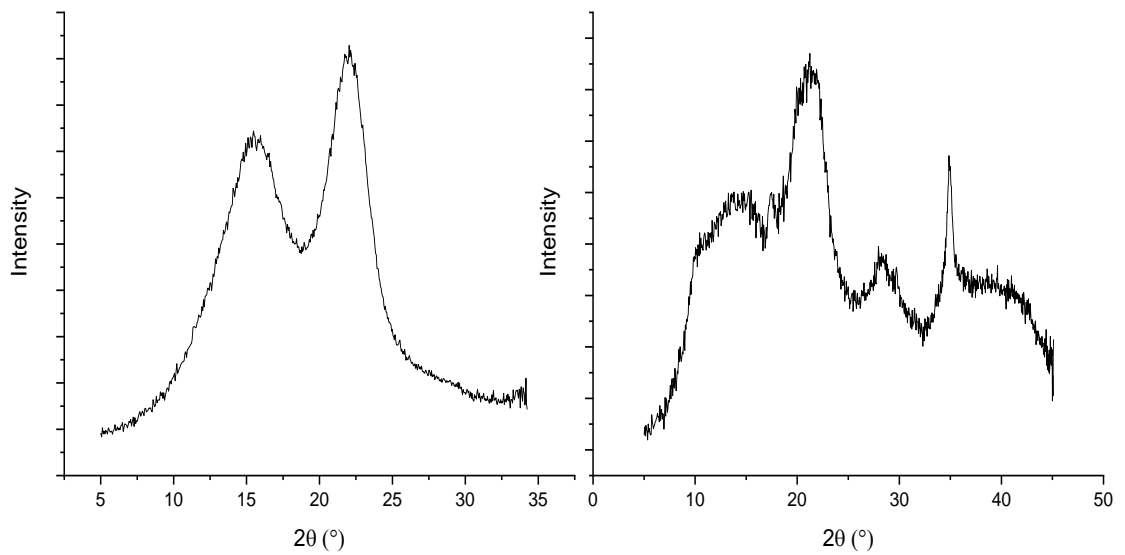


Figure 6.19: Integration of WAXS data for nanofibrillated cellulose fibres perpendicular (left) and parallel (right) to the direction of the mounted fibre

Consistent with all of the previous samples, the perpendicular azimuthal integration shows contributions from only the $1\bar{1}0$ and 200 reflections, whereas the parallel direction has more reflection contributions (see Figure 6.19).

6.5 Alginate and Cellulose Film Samples

6.5.1 Alginate Film Sample in the Absence of Cellulose

Film samples of alginate, MFC and NFC were also prepared to use as a comparison to fibre samples to monitor the effect of the spinning process on the crystallisation and orientation.

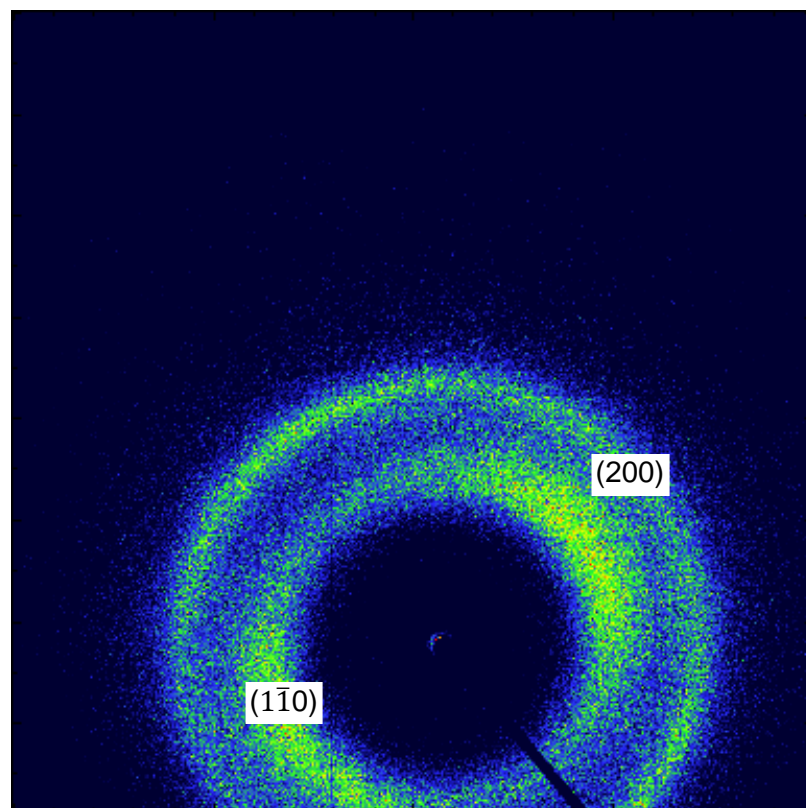


Figure 6.20: 2D detector image of alginate film containing no cellulose

In comparison to the fibre alginate sample, the film sample shows a more diffuse scattering in both diffraction rings and appears to be much less crystalline (see Figure 6.20).

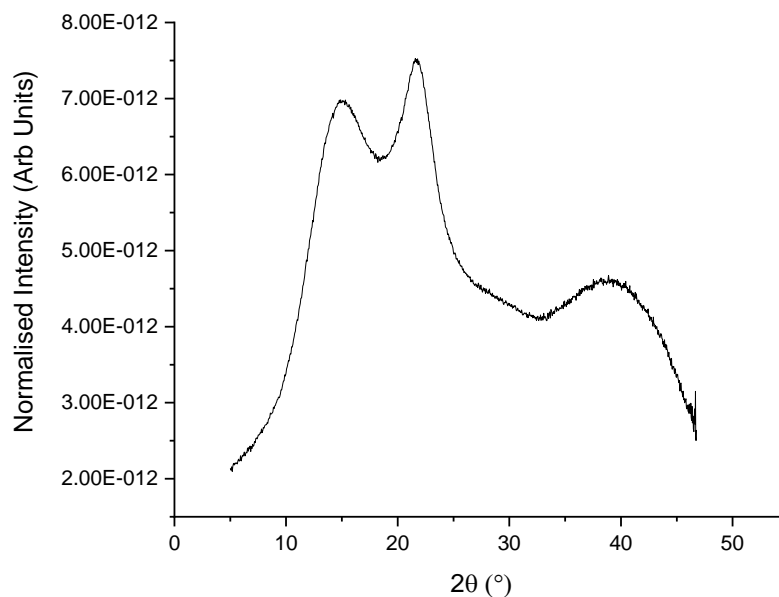


Figure 6.21: 1D azimuthal integration plot of alginate film from integrated 2D image

Consistent with the film sample and the raw material is the profile of the azimuthal integration data. Two peaks are observed at approximately 13° and 22°, with an amorphous hump between 35-45° (see Figure 6.21).

6.5.2 Nanofibrillated Cellulose Film

The detector image of NFC as a film is quite different to the NFC fibre, a much more crystalline pattern has been obtained with no orientation in any of the scattering rings (see Figure 6.22).

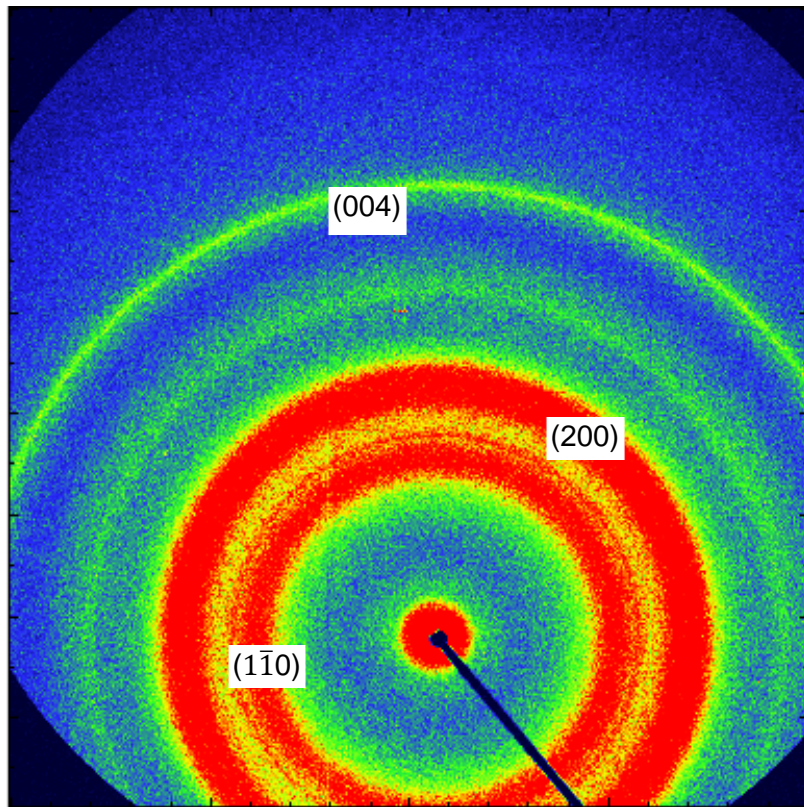


Figure 6.22: 2D detector image of nanofibrillated cellulose film

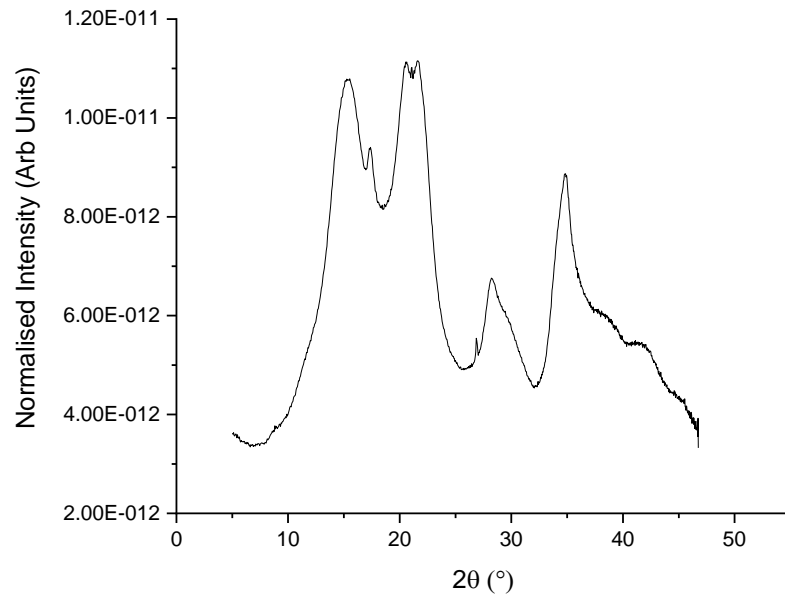


Figure 6.23: 1D plot of nanofibrillated cellulose film from integrated 2D image

An azimuthal integration over the whole two theta range produced a 1D plot (see Figure 6.23) containing more peaks than the equivalent 1D plot from the NFC fibre sample. As the sample could not be mounted in a specific direction to the beam, integrations could not be performed in parallel and perpendicular directions.

6.5.3 Microfibrillated Cellulose Film

As shown in section 6.5.2 the NFC film appears to be more crystalline than the fibre based on the detector images. The same pattern is seen with the MFC film as shown in Figure 6.24.

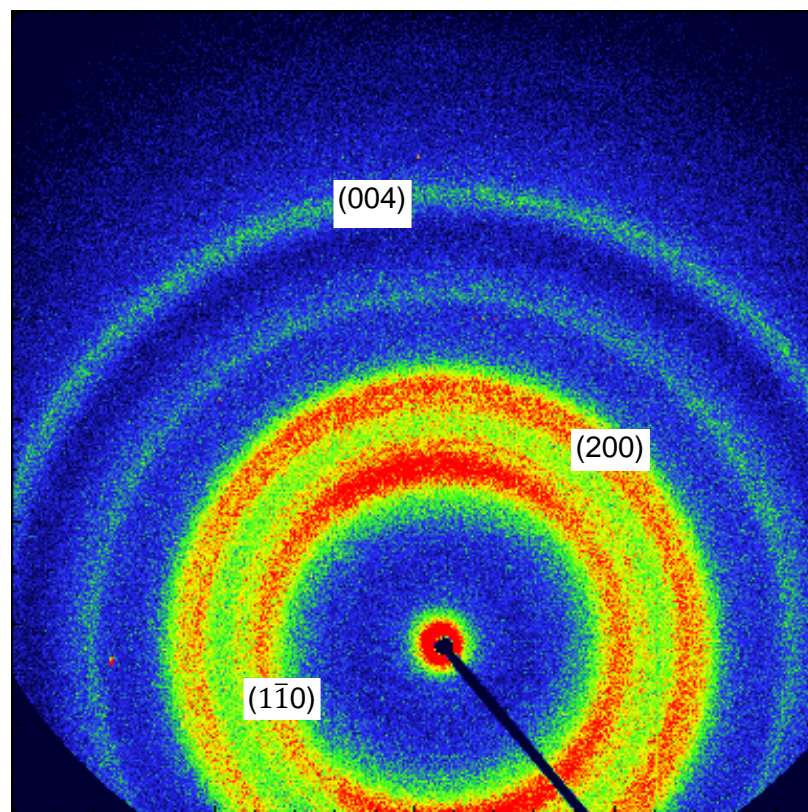


Figure 6.24: 2D detector image of microfibrillated cellulose film

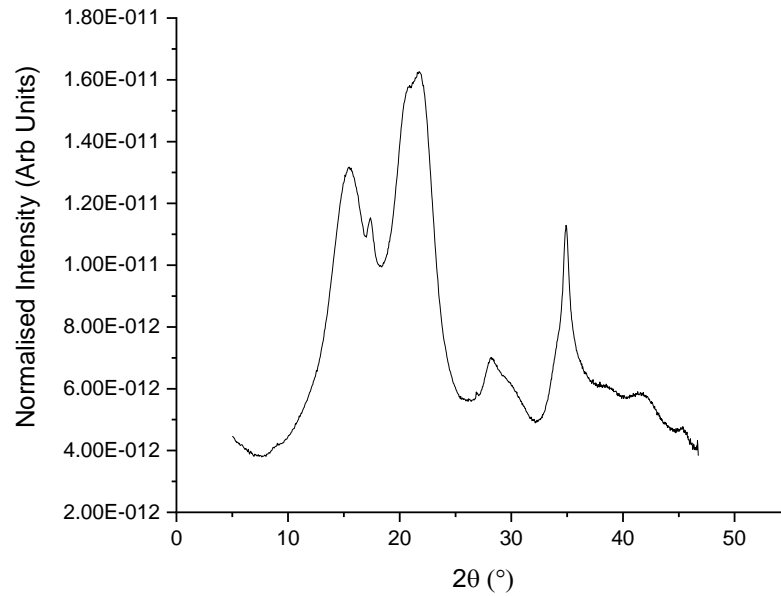


Figure 6.25: 1D plot of microfibrillated cellulose film from integrated 2D image

An azimuthal integration over the whole two theta range produced a 1D plot containing more peaks than the equivalent 1D plot from the MFC fibre sample. As the sample could not be mounted in a specific direction to the beam, integrations could not be performed in parallel and perpendicular directions (see Figure 6.25).

6.6 Orientation Index and Percent Crystallinity Analysis

The orientation index of cellulose is generally performed using the 200 peak due to this peak being the most intense of the crystalline peaks associated with cellulose as this peak shows the greatest difference between samples. The orientation index of all samples was calculated using Eqn 6.4 based on an azimuthal integration of the 200 reflection as shown in Figure 6.26.

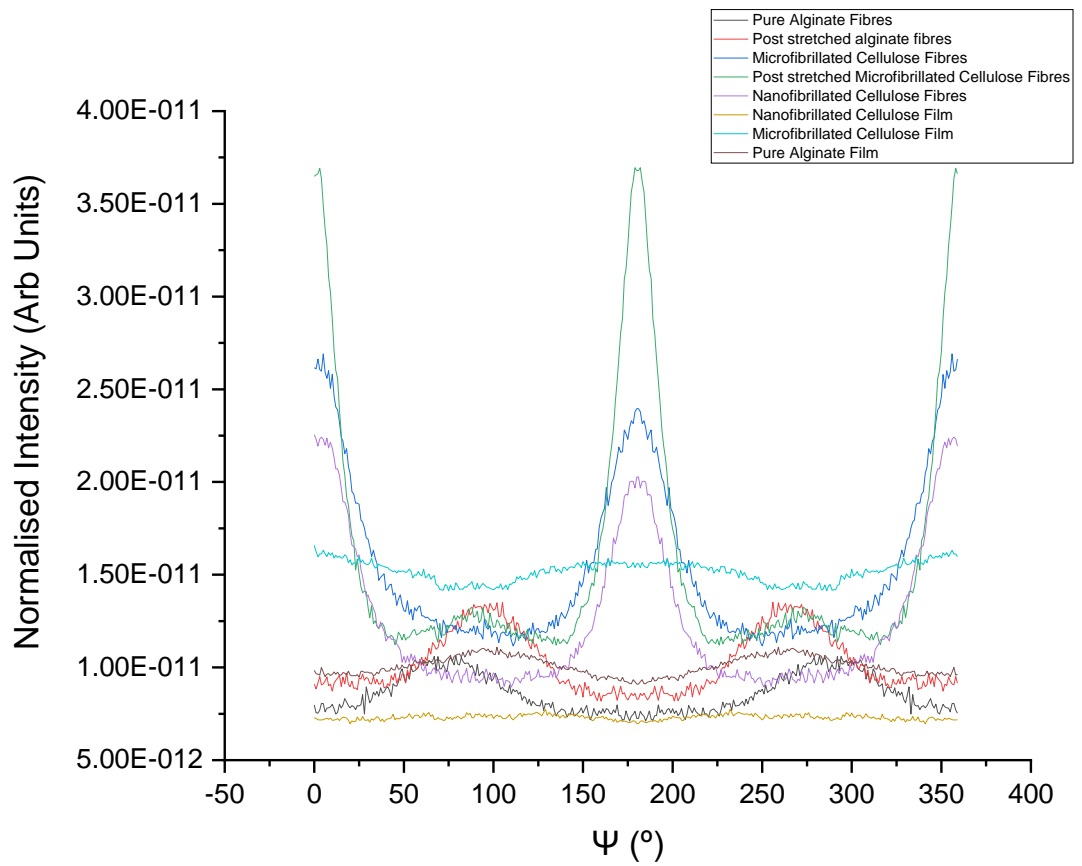


Figure 6.26: Azimuthal profile of all fibre and film samples based on the 200 reflection

The orientation index was also calculated based on the $1\bar{1}0$ reflection (see Figure 6.27). The higher intensity of the ring associated with the $1\bar{1}0$ reflection, when compared to the 200 reflection, indicated that stretching of some samples had preferentially aligned the nanocrystals in the $1\bar{1}0$ reflection.

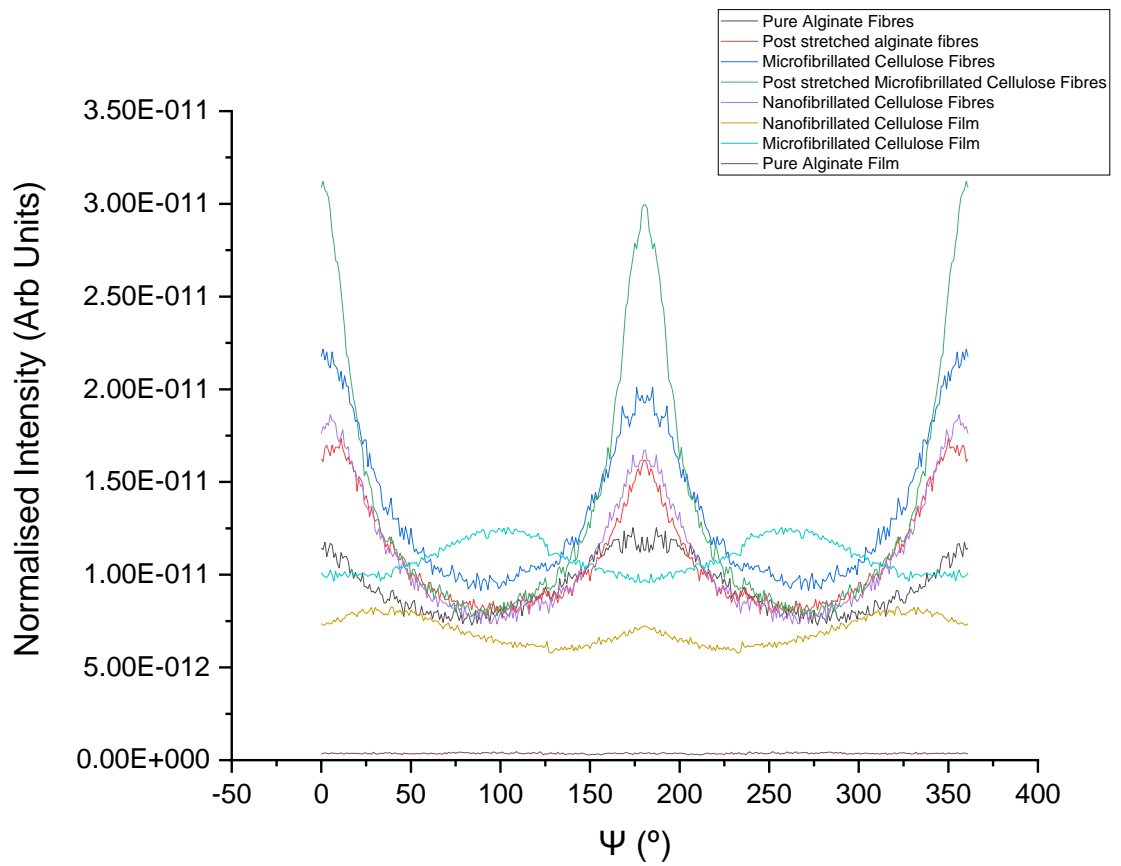


Figure 6.27: Azimuthal profile of all fibre and film samples based on the $1\bar{1}0$ reflection

The orientation index was calculated, using Eqn 6.4, for both the 200 and $1\bar{1}0$ reflections and is shown in Table 6.1. The closer the obtained number is to 1.0 indicates a greater degree of orientation.

Table 6.1: Orientation index values for all fibre and film samples calculated from azimuthal integrations of the 200 and $1\bar{1}0$ reflections

Sample	Orientation Index (200)	Orientation Index ($1\bar{1}0$)
Pure Alginate Fibres	0.665	0.617
Post stretched Alginate Fibres	0.667	0.781
MFC Fibres	0.762	0.721
Post stretched MFC Fibres	0.859	0.811
NFC Fibres	0.797	0.745
NFC Film	0.389	0.657
MFC Film	0.890	0.803
Alginate Film	0.554	0.981

The orientation index values indicate that stretching the fibres can influence the degree of orientation of the cellulose nanocrystals as seen in cellulose from other sources.²³ This observation is highlighted by the values obtained for the MFC fibre and MFC post-stretched fibre when the crystal orientation increased from 0.762 to 0.859. By comparison, when the alginate fibre was stretched, there was no significant increase in orientation observed as shown in Table 6.1. Thus, these results suggest that stretching affects the cellulose nanocrystals but does not seem to impact the alginate structure.

The crystallinity of all samples was initially calculated using Segal's method which is historically the most common method of calculating crystallinity for cellulose

samples. It was noticed that the values obtained using this method didn't line up with expectations of crystallinity from the detector images obtained. As such another method was explored, this method is commonly known as the deconvolution method and was carried out, in this instance, by using the Bruker EVA software. This method looks at a ratio of the overall intensity of the profile as a function of the amorphous background. Results obtained with this method appeared to be in line with what raw detector images would suggest.

Table 6.2: Percent crystallinity values for all fibre and film samples calculated using Segals method and the deconvolution method

Sample	Segals method (% crystallinity)	Deconvolution method (% crystallinity)	Difference (%)
Pure alginate fibres	9.23	27.6	18.37
Post stretched alginate fibres	7.06	28.3	21.24
MFC fibre	31.15	39.3	8.15
MFC post stretched fibre	35.88	43.0	7.12
NFC fibre	31.50	39.0	7.50
NFC film	36.48	62.7	11.54
MFC film	19.21	58.5	39.29
Alginate film	15.46	27.0	26.22

The crystallinity results obtained reinforced what was observed from the detector images. Film samples had a greater crystallinity than the equivalent fibre samples and stretching the fibre samples resulted in an increased crystallinity. This result

is most probably linked to the manufacturing process of the fibres as the extrusion of the fibres through a die may have helped to increase the orientation of the crystals in the fibres. Similarly, the extrusion of the cellulose could have broken down existing crystalline material. Understanding the orientation of the cellulose nanocrystals allows us to gain the most benefit from the mechanical properties.

6.7 Summary

Formulations of microfibrillated and nanofibrillated cellulose fibres and films that use sodium alginate as a carrier polymer were successfully characterised for both orientation index and crystallisation using WAXS.

Fibres of nano or microfibrillated cellulose did not differ greatly in overall crystallinity or orientation. However, it was observed that the stretching of fibres after spinning resulted in a greater orientation than samples that had not been stretched. This result is likely due to the nanocrystals within the cellulose being aligned during the stretching process. This analysis reveals that stretching is a relatively straightforward process of increasing certain physical characteristics of cellulose fibres that may be desirable when using these fibres in other materials.

Crystallinity results were calculated using both Segal's method and the deconvolution method described earlier. The results presented here suggest the presence of alginate within the formulation rendered Segal's method invalid. As Segal's method is intended for pure cellulose samples¹⁹⁸ and uses the dip in the diffractogram between the $1\bar{1}0$ and 200 reflections that correspond to amorphous intensity, this method relies on no interference at this point. However, as alginate contains a crystalline peak within this region of the diffractogram, the crystallinity results from Segal's method did not agree with what was observed in the raw detector images.

While the crystallinity of the films was shown to be greater than the fibre samples, the fibre samples had a greater orientation. Understanding these characteristics is important as orientation impacts the strength of the material more than crystallinity.

Although other cellulose materials produced with cellulose from different raw materials, such as wood fibres, have been published with more desirable mechanical properties such as a higher Young's modulus than the samples analysed in this work. There is still promise for the materials presented here due to their eco-friendly origin. The potato pulp used to make these fibres was obtained as a waste product of another process and as such using the pulp to make fibres reduces existing waste and provides a cheaper starting material for cellulose materials.

Further improvements could potentially be made to the mechanical properties with small adjustments to the formulation process. Controlling the strength of these materials could be investigated by adjusting the drying rates for the film samples and the spinning rates for the fibre samples. Combining both micro and nanofibrillated materials may also result in an increased crystallinity or orientation of the samples. As stretching has already been shown to increase orientation within the fibres, different methods of stretching, such as adjusting the stretching force, could be looked at as a means of further improving the mechanical properties of these fibres. The ability of WAXS to analyse both crystallinity and orientation of cellulose fibres and films was shown in this work, and understanding how to control the properties of cellulose from environmentally friendly sources such as the potato pulp used here could lead to a greater uptake in its use.

Chapter 7: Conclusions and Future Work

The work presented within this thesis looks at the practical use of X-ray techniques for the analysis of a range of pharmaceutically relevant materials.

ASDs are sometimes used by pharmaceutical companies to overcome issues with poor aqueous solubility of the crystalline form.²⁰⁴ Dissolution testing is the gold standard technique for measuring drug release and solubilisation from dosage products. The dissolution of compounds exhibiting poor aqueous solubility is enhanced when the compound is formulated in its amorphous state.^{53,46} However, crystallisation of an amorphous compound can occur when the amorphous form is introduced to water, and thus, the measured solubility of the amorphous form remains low. The combination of drug loading percent and manufacturing temperature can be used to produce an ASD which will allow the compound to remain in its amorphous state during dissolution.²⁰⁵ By using an amorphous form of a crystalline drug we increase the solubility allowing a higher concentration of the drug in the gastrointestinal fluid.⁵³

In chapter 4, we showed that WAXS can be used to obtain real-time information on the crystallisation tendencies of paracetamol containing ASDs. THz Raman was used to confirm crystallisation had occurred. While THz Raman can be used to collect real-time data on crystallisation, WAXS can offer an easier interpretation of different crystalline forms when compared with THz Raman. The WAXS data enabled us to identify the concentration of paracetamol in an Affinisol™ polymer at which the amorphous form was stable and crystallisation did not occur. The information collected using such experiments could inform manufacturing parameters and drug loading levels where a stable amorphous solid dispersion can be achieved. The results obtained during this work have demonstrated the use of a lab-based instrument setup for the determination of crystallisation from within an ASD, while also giving insight into possible mechanisms of the

crystallisation as shown in Figure 4.17. The presence of crystals on the surface of the extrudate was observed for all samples which had undergone crystallisation, along with the gel like nature of the ASD sample at the end of the experiment suggests that upon gelling of the polymer the molecular mobility of the API is increased allowing for diffusion to the surface where crystallisation was facilitated.

Further work in this area would look to improve upon the existing experimental setup. For example, the use of a flow cell sample holder would allow for the continual refreshment of media to ensure the API is at sink conditions. Where the amount of dissolution media would dissolve a minimum of 3 times the amount of drug that is in the dosage form, this is a better representation of a more biologically relevant environment.²⁰⁶ Furthermore, coupling a UV spectroscopy detector to the X-ray analysis could simultaneously give information on the solid state (from WAXS) of the compound while being able to monitor the drug release (solution concentration from UV spectroscopy) yielding structural data in parallel to that from a standard dissolution test.

Additionally, time resolved experiments utilising the extra flux of a synchrotron beamline could provide greater insight into structural changes within the API and potentially the mechanism of crystallisation. Although limited uses of simultaneous SAXS/WAXS exist in the field of ASD research, in the polymer research space there are numerous examples of its use.^{207,208} The combination of lengthscales accessible through the techniques has allowed for monitoring of crystallisation while also probing structural changes occurring leading up to and after crystallisation. This combination of techniques could allow for greater insight into the structural changes occurring within ASDs during dissolution, and more knowledge of these processes could help inform the processing conditions used

that would result in the greatest stability of the formulation. The use of time resolved computed tomography (CT) would allow for the characterisation of phase separation occurring within the ASD formulation during dissolution, providing information on drug clusters in terms of shape and/or size could help inform any bespoke SAXS models for probing deeper into the structural changes.^{209, 210} Combining SAXS and pair distribution function (PDF) analysis has been used as a means of monitoring the formation of nanoclusters in inorganic systems.²¹¹ The combined approach used for small organic molecules could enable the identification of prenucleation sites in ASDs, providing a better understanding of the mechanisms of the crystallisation processes occurring

In chapter 5, SAXS was used as a characterisation tool to monitor the varying amorphous content of powdered samples of GSK2838232M prepared via ball milling of a bulk crystalline starting material. Other analysis tools were used to assess the suitability and accuracy of using SAXS for this analysis. These techniques included DSC, TGA, XRD, FTIR and SEM. Intensity differences in the SAXS profiles of the various materials can be linked to the different degrees of homogeneity within the samples and can therefore be used to assess how much amorphous and crystalline material is present in each sample.

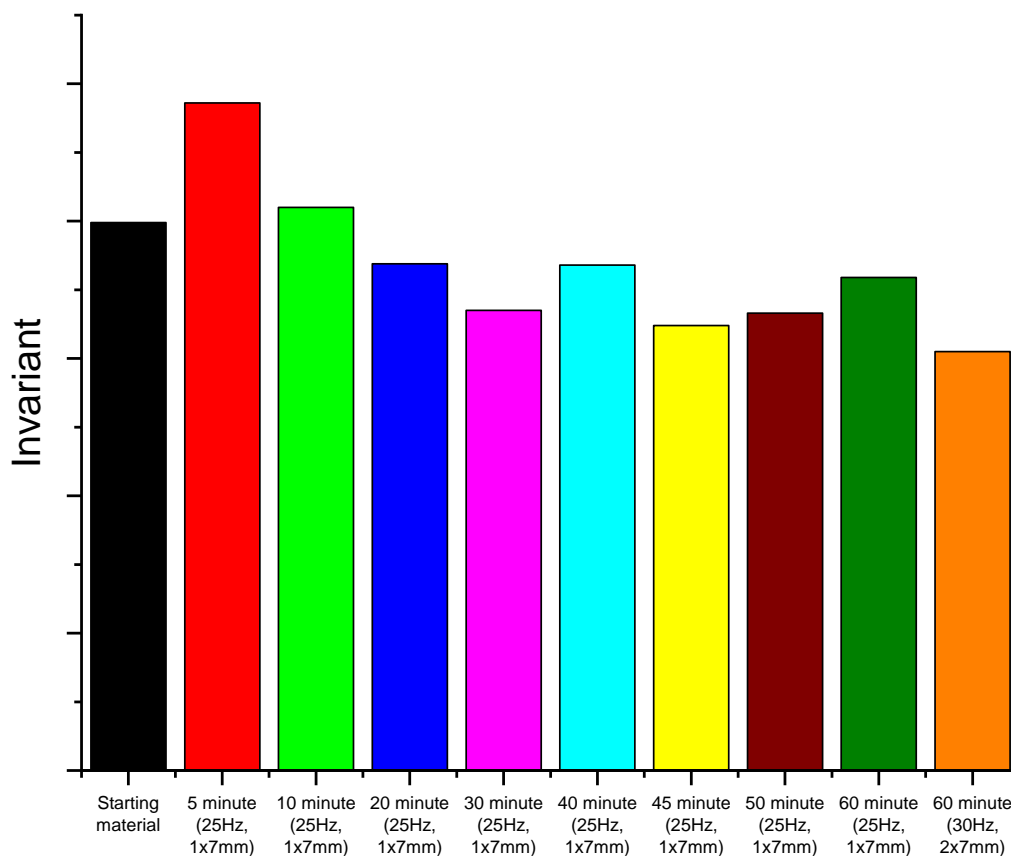


Figure 7.1: SAXS Porod invariant analysis of GSK2838232M and subsequent milled samples

Porod invariant analysis (Figure 7.1) was used as a means of analysing density fluctuations due to the emergence of amorphous material. The calculated Porod invariant was found to differ based on the length of time milling the material. Specifically, the invariant decreased as milling time increased, suggesting a decrease in heterogeneity as the sample becomes more amorphous. Porod invariant analysis allowed for a quantifiable number to be extracted from the SAXS scattering patterns, however, at this stage no more information is readily available using this method as opposed to a simpler qualitative method of examining the scattering profiles directly to observe intensity differences. The use of the Porod invariant analysis may be more suited to materials which produce a stronger

scattering profile, the similarity in intensity of GSK2838232M at varying crystallinity proves difficult to differentiate between. For use with small organic molecules the Porod invariant has shown to be useful to distinguish between differing manufacturing methods, where the amorphous form can differ significantly.^{212,213}

To progress the work from this chapter, the use of a complimentary technique could be explored. Further work could also pair SAXS data with pair distribution function (PDF) analysis, as structural information available from PDF could help inform the data analysis of the SAXS model as with only SAXS information available it is difficult to choose appropriate models to use in the data analysis. PDF is currently finding use in the analysis of amorphous pharmaceuticals to determine stability and can also be used to differentiate between amorphous forms produced via various manufacturing techniques.^{214,215} Of more interest when looking at PDF as a complimentary technique to SAXS as a tool for amorphous structure characterisation is the work looking at the local structure of amorphous materials, predominantly used in the inorganic materials sector^{216,217} the ability to extract information around the spacings within the molecule can be directly placed into the SAXS model to inform on the structure. The use of combined SAXS and PDF has been shown in the characterisation of amorphous nanoparticles, while SAXS can inform on the internal structures of such systems PDF enables the local atomic structure to be studied.²¹⁸

X-ray scattering techniques not only hold relevance when analysing pharmaceutically relevant systems like those described above. They are also routinely used for the analysis of colloidal systems such as cellulose used for both drug delivery applications,^{211,212,213} but gaining more interest for their use as strengthening materials that are sustainable in nature.^{22,27}

In chapter 6, cellulose fibres and films prepared from potato pulp waste were characterised by 2D WAXS to analyse the degree of crystallinity and the orientation of the nanocellulose crystals. Potato pulp is a waste by-product collected during the production of starch. Cellulose obtained from potato pulp resulted in a more porous structure compared with other sources. The cellulose characterised in these studies had a lower crystallinity index than cellulose from other biomass raw materials.²²² Although this can result in a weaker reinforcing power of the material, the cellulose has been sourced from a waste product as an alternative to other biomass used to produce cellulose such as wood and food sources which are required for other applications. In this thesis, crystallinity calculations were performed using a deconvolution method and the Segal's method. It was found that the Segal's method was unsuitable for the samples analysed in this study due to the presence of a sodium alginate peak overlapping with the characteristic amorphous region for cellulose in the diffractograms. As the deconvolution method accounts for the amorphous background present, this method was used to determine crystallinity values that visually corresponded to what was observed in the detector images.

2D WAXS characterisation of cellulose fibres and films gave a greater understanding of the crystallinity and orientation of the nanocrystals within the cellulose structure. Our results showed that the crystallinity of the potato-starch cellulose samples did not differ greatly if samples were prepared by micro- or nano- fibrillation. By contrast, it was observed that films had a greater crystallinity than fibres of the same material. While the films exhibited more crystallinity, the fibres had a greater orientation index. Although the cellulose obtained from waste potato-pulp did not produce cellulose with the highest crystallinity and orientation when compared with cellulose from other sources,^{185,223} the use of this by-product

still demonstrates the possibilities a material which would otherwise go to waste. Using cellulose obtained from waste potato-pulp can be considered a greener alternative to some other raw materials currently used. The increased orientation of the CNC observed when the material had been stretched highlights an easy and cheap way to improve the properties of the material.

Additionally, SAXS could also be used to characterise crystallinity and orientation changes arising from altering the cellulose formulation process, such as adjusting drying rates for films and spin rates for fibres. As the changes within these systems are static and non-dynamic, the flux offered at a synchrotron is not required, although a longer exposure time will be required, laboratory-based systems can be used.

In this thesis, the use of various X-ray based analytical techniques has allowed the characterisation of a wide range of materials both environmentally and pharmaceutically relevant. Here, we show that these techniques can give real time characterisation of the structure of ASDs via WAXS and that this technique could be implemented to help streamline the manufacturing process. WAXS can also provide crystallinity and orientation information to showcase the potential of greener raw materials for cellulose production.

References

1. Aitipamula S, Vangala VR. X-Ray Crystallography and its Role in Understanding the Physicochemical Properties of Pharmaceutical Cocrystals. *Journal of the Indian Institute of Science*. 2017; 97:227-43.
2. Alqahtani MS, Kazi M, Alsenaidy MA, Ahmad MZ. Advances in Oral Drug Delivery. *Front Pharmacol*. 2021;12:1-21.
3. Couillaud BM, Espeau P, Mignet N, Corvis Y. State of the Art of Pharmaceutical Solid Forms: from Crystal Property Issues to Nanocrystals Formulation. *ChemMedChem*. 2019;14(1):8–23.
4. Kabeya K, Satoh H, Hori S, Sawada Y. Experimental study on patient preferences regarding the shape and size of medical tablets and capsules using three-dimensionally printed plastic model formulations. *Patient Preference Adherence*. 2021;15:863–70.
5. Shariff Z, Kirby D, Missaghi S, Rajabi-Siahboomi A, Maidment I. Patient-centric medicine design: Key characteristics of oral solid dosage forms that improve adherence and acceptance in older people. *Pharmaceutics*. 2020;12(10):1–15.
6. Newman A, Wenslow R. Solid form changes during drug development: good, bad, and ugly case studies. *AAPS Open*. 2016;2(1):1-11.
7. Qi SY, Tian Y, Zou WB, Hu CQ. Characterization of solid-state drug polymorphs and real-time evaluation of crystallization process consistency by near-infrared spectroscopy. *Frontiers in Chemistry*. 2018;6:1-7.
8. Pikal MJ, Rigsbee D. The Stability of Insulin in Crystalline and Amorphous Solids: Observation of Greater Stability for the Amorphous Form.

- Pharmaceutical Research*. 1997;14:1379–87.
9. Sun Y, Zhu L, Wu T, Cai T, Gunn EM, Yu L. Stability of Amorphous Pharmaceutical Solids: Crystal Growth Mechanisms and Effect of Polymer Additives. *AAPS J*. 2012;14(3):380-88.
 10. Boyd BJ, Bergström CAS, Vinarov Z, Kuentz M, Brouwers J, Augustijns P, et al. Successful oral delivery of poorly water-soluble drugs both depends on the intraluminal behavior of drugs and of appropriate advanced drug delivery systems. *Eur J Pharm Sci*. 2019;137:1-27.
 11. Williams HD, Trevaskis NL, Charman SA, Shanker RM, Charman WN, Pouton CW, et al. Strategies to address low drug solubility in discovery and development. *Pharmacological Reviews*. 2013;65(1):315-499.
 12. Amidon GL, Lennernäs H, Shah VP, Crison JR. A Theoretical Basis for a Biopharmaceutic Drug Classification: The Correlation of in Vitro Drug Product Dissolution and in Vivo Bioavailability. *Pharm Res An Off J Am Assoc Pharm Sci*. 1995;12(3):413–20.
 13. Rautio J, Kumpulainen H, Heimbach T, Oliyai R, Oh D, Järvinen T, et al. Prodrugs: Design and clinical applications. *Nature Reviews Drug Discovery*. 2008;7:255-70.
 14. Dhore PW, Dave VS, Saoji SD, Bobde YS, Mack C, Raut NA. Enhancement of the aqueous solubility and permeability of a poorly water soluble drug ritonavir via lyophilized milk-based solid dispersions. *Pharm Dev Technol*. 2017;22(1):90-102.
 15. Hecq J, Deleers M, Fanara D, Vranckx H, Amighi K. Preparation and characterization of nanocrystals for solubility and dissolution rate enhancement of nifedipine. *Int J Pharm*. 2005;299(1-2):167-77.

16. Serajuddin ATM. Salt formation to improve drug solubility. *Advanced Drug Delivery Reviews*. 2007;59(7):603-16.
17. Schittny A, Huwyler J, Puchkov M. Mechanisms of increased bioavailability through amorphous solid dispersions: a review. *Drug Deliv*. 2020;27(1):110-27.
18. Khadka P, Ro J, Kim H, Kim I, Kim JT, Kim H, et al. Pharmaceutical particle technologies: An approach to improve drug solubility, dissolution and bioavailability. *Asian Journal of Pharmaceutical Sciences*. 2014;9(6):304-16.
19. Qiu Y, Chen Y, Zhang G, Liu L, Porter W. 2008, *Developing Solid Oral Dosage Forms*, Academic Press, USA.
20. Mcnamara JT, Morgan JLW, Zimmer J. A Molecular Description of Cellulose Biosynthesis. *Annu Rev Biochem*. 2015;84:895–921.
21. Meyer K, Misch L. Positions des atomes dans le nouveau modele spatial de la cellulose. *Helv Chim*. 1937;20:232–44.
22. Lundahl MJ, Cunha AG, Rojo E, Papageorgiou AC, Rautkari L, Arboleda JC, et al. Strength and Water Interactions of Cellulose i Filaments Wet-Spun from Cellulose Nanofibril Hydrogels. *Sci Rep*. 2016;6:1-13.
23. Kim K, Kim PJ, Chowdhury RA, Kantharaj R, Candadai A, Marconnet A, et al. Structural orientation effect of cellulose nanocrystals (CNC) films on electrochemical kinetics and stability in lithium-ion batteries. *Chem Eng J*. 2021;417:1-8.
24. Rongpipi S, Ye D, Gomez ED, Gomez EW, Bartley LE. Progress and Opportunities in the Characterization of Cellulose – An Important Regulator of Cell Wall Growth and Mechanics. *Front Plant Sci*. 2019;9:1–28.

25. Mao Y, Liu K, Zhan C, Geng L, Chu B, Hsiao BS. Characterization of Nanocellulose Using Small-Angle Neutron, X-ray, and Dynamic Light Scattering Techniques. *J Phys Chem B*. 2017;121(6):1340-51.
26. Ma Y, Rosson L, Wang X, Byrne N. Upcycling of waste textiles into regenerated cellulose fibres: impact of pretreatments. *J Text Inst*. 2020;111(1):1-9.
27. Lee KY, Tammelin T, Schulfter K, Kiiskinen H, Samela J, Bismarck A. High performance cellulose nanocomposites: Comparing the reinforcing ability of bacterial cellulose and nanofibrillated cellulose. *ACS Appl Mater Interfaces*. 2012; 4(8):4078-86.
28. Jakob M, Raj A, Gindl-altmutter W, Bliem P, Konnerth J, Müller U, et al. Progress in Materials Science The strength and stiffness of oriented wood and cellulose-fibre materials : A review. *Prog Mater Sci*. 2022;125:1-31.
29. Florence, Alexander T; Attwood D, 2015, 6th edn, *Physicochemical Principles of Pharmacy*, Pharmaceutical Press, United Kingdom
30. Childs SL, Chyall LJ, Dunlap JT, Smolenskaya VN, Stahly BC, Stahly GP. Crystal engineering approach to forming cocrystals of amine hydrochlorides with organic acids. Molecular complexes of fluoxetine hydrochloride with benzoic, succinic, and fumaric acids. *J Am Chem Soc*. 2004;126(41):13335–42.
31. Skyner RE, McDonagh JL, Groom CR, Van Mourik T, Mitchell JBO. A review of methods for the calculation of solution free energies and the modelling of systems in solution. *Phys Chem Chem Phys*. 2015;17(9):6174–91.
32. Lüder K, Lindfors L, Westergren J, Nordholm S, Kjellander R. In silico prediction of drug solubility. 3. Free energy of solvation in pure amorphous

- matter. *J Phys Chem B*. 2007;111(25):7303–11.
33. Haisa M, Kashino S, Kawai R, Maeda H. The Monoclinic Form of p-Hydroxyacetanilide. *Acta Crystallogr Sect B Struct Crystallogr Cryst Chem*. 1976;32:1283-85.
 34. Drebuschak TN, Boldyreva E V. Variable temperature (100-360 K) single-crystal X-ray diffraction study of the orthorhombic polymorph of paracetamol (p-hydroxyacetanilide). *Zeitschrift fur Krist*. 2004;219:506-12.
 35. Reiss CA, Van Mechelen JB, Goubitz K, Peschar R. Reassessment of paracetamol orthorhombic Form III and determination of a novel low-temperature monoclinic Form III-m from powder diffraction data. *Acta Crystallogr Sect C Struct Chem*. 2018;74(3):392-99.
 36. Bauer J, Spanton S, Henry R, Quick J, Dziki W, Porter W, et al. Ritonavir: An extraordinary example of conformational polymorphism. *Pharm Res*. 2001;18(6):859-66.
 37. Seethalekshmi S, Row TNG. Conformational polymorphism in a non-steroidal anti-inflammatory drug, mefenamic acid. *Cryst Growth Des*. 2012;12(8):4283-89.
 38. Masuda T, Yoshihashi Y, Yonemochi E, Fujii K, Uekusa H, Terada K. Cocrystallization and amorphization induced by drug-excipient interaction improves the physical properties of acyclovir. *Int J Pharm*. 2012;422(1-2):160-69.
 39. Shayanfar A, Asadpour-Zeynali K, Jouyban A. Solubility and dissolution rate of a carbamazepine-cinnamic acid cocrystal. *J Mol Liq*. 2013;187:171-76.
 40. Ramle NA, Rahim SA, Anuar N, El-Hadad O. Solubility of carbamazepine cocrystals in ethanolic solution. *AIP Conference Proceedings*.

2017;1879:040001.

41. Jung MS, Kim JS, Kim MS, Alhalaweh A, Cho W, Hwang SJ, et al. Bioavailability of indomethacin-saccharin cocrystals. *J Pharm Pharmacol*. 2010;62(11):1560-68.
42. Vranic E. Characterization of amorphous solids. *Bosnian Journal of Basic Medical Science*. 2004;4(3):35–9.
43. Nunes C, Mahendrasingam A, Suryanarayanan R. Quantification of Crystallinity in Substantially Amorphous Materials by Synchrotron X-ray Powder Diffractometry. *Pharm Res*. 2005;22:1942-53.
44. Peng Y, Dussan DD, Narain R. 2020. *Thermal, mechanical, and electrical properties*, Amsterdam:Elsevier. p.179-201.
45. Safranski DL. 2017. *Introduction to Shape-Memory Polymers. Shape-Memory Polymer Device Design*. USA:Elsevier. 2017. p.1–22.
46. Hancock BC, Parks M. What is the true solubility advantage for amorphous pharmaceuticals? *Pharm Res*. 2000;17(4):397–404.
47. Stukelj J, Svanback S, Agopov M, Lobmann K, Strachan CJ, Rades T, et al. Direct Measurement of Amorphous Solubility. *Anal. Chem*. 2019;91(11):7411–17.
48. Liu B, Theil F, Lehmkemper K, Gessner D, Li Y, Lishaut H Van. Crystallization Risk Assessment of Amorphous Solid Dispersions by Physical Shelf-Life Modeling : A Practical Approach. *Mol Pharmaceutics*. 2021;18(6):2428-37.
49. Rumondor ACF, Wikström H, Van Eerdenbrugh B, Taylor LS. Understanding the Tendency of Amorphous Solid Dispersions to Undergo Amorphous–

- Amorphous Phase Separation in the Presence of Absorbed Moisture. *AAPS PharmSciTech*. 2011;12(4):1209–19.
50. Konno H, Taylor LS. Ability of Different Polymers to Inhibit the Crystallization of Amorphous Felodipine in the Presence of Moisture. *Pharm Res*. 2008;25(4):969-78.
51. Walica T, Kotek M, Gierczycki A, Lemanowicz M, Miela A. Application of Polymers as a Tool in Crystallization — A Review. *Polymers*. 2021;13(16):1–22.
52. Zografi G, Newman A. Interrelationships Between Structure and the Properties of Amorphous Solids of Pharmaceutical Interest. *J Pharm Sci*. 2017;106(1):5–27.
53. Hancock BC, Zografi G. Characteristics and Significance of the Amorphous State in Pharmaceutical Systems. *J Pharm Sci*. 1997;86(1):1–12.
54. Mishra D, Dhote VK, Mishra PK. Amorphous solid dispersion technique for improved drug delivery: Basics to clinical applications. *Drug Deliv Transl Res*. 2015;5(6):552-65.
55. Murdande SB, Pikal MJ, Shanker RM, Bogner RH, Murdande SB, Pikal MJ, et al. Aqueous solubility of crystalline and amorphous drugs : Challenges in measurement. *Pharm Dev Technol*. 2011;16(3):187-200.
56. Surikutchi BT, Bansal AK. Drug-excipient behavior in polymeric amorphous solid dispersions Drug-excipient behavior in polymeric amorphous solid dispersions. *Journal of Excipients and Food Chemicals*. 2018;4(3):70-94.
57. Baghel S, Cathcart H, O'Reilly NJ. Polymeric Amorphous Solid Dispersions: A Review of Amorphization, Crystallization, Stabilization, Solid-State Characterization, and Aqueous Solubilization of Biopharmaceutical

- Classification System Class II Drugs. *Journal of Pharmaceutical Sciences*. 2016;105:2527–44.
58. Sahoo A, Suryanarayanan R, Siegel RA. Stabilization of Amorphous Drugs by Polymers: The Role of Overlap Concentration (C^*). *Mol Pharmaceutics*. 2020;17(11):4401-06.
59. Tian B, Tang X, Taylor LS. Investigating the Correlation between Miscibility and Physical Stability of Amorphous Solid Dispersions Using Fluorescence-Based Techniques. *Mol Pharmaceutics*. 2016;13(11):3988–4000.
60. Gray VA. Power of the Dissolution Test in Distinguishing a Change in Dosage Form Critical Quality Attributes. *AAPS PharmSciTech*. 2018;19(8):3328–32.
61. Noyes A, Whitney W. The Rate of Solution of Solid Substances in Their Own Solution. *J Am Chem Soc*. 1897;19(12):930–4.
62. Dokoumetzidis A, Macheras P. A century of dissolution research : From Noyes and Whitney to the Biopharmaceutics Classification System. *Int J Pharm*. 2006;321(1-2):1–11.
63. Siepmann J, Peppas NA. Higuchi equation : Derivation, applications, use and misuse. *Int J Pharm*. 2011;418(1):6–12.
64. Van Drooge DJ, Hinrichs WLJ, Frijlink HW. Anomalous dissolution behaviour of tablets prepared from sugar glass-based solid dispersions. *J Control Release*. 2004;97(3):441-52.
65. Savolainen M, Kogermann K, Heinz A, Aaltonen J, Peltonen L, Strachan C, et al. Better understanding of dissolution behaviour of amorphous drugs by in situ solid-state analysis using Raman spectroscopy. *Eur J Pharm Biopharm*. 2009;71(1):71–9.

66. Ping L, Giovanna S. Combined Effects of Supersaturation Rates and Doses on the Kinetic Solubility Profiles of Amorphous Solid Dispersions Based on Water Insoluble Poly(2-hydroxyethyl methacrylate) Hydrogels. *Mol Pharmaceutics*. 2018;15:2017–26.
67. Brouwers J, Brewster ME, Augustijns P. Supersaturating Drug Delivery Systems : The Answer to Solubility-Limited Oral Bioavailability ? *J Pharm Sci*. 2009;98(8):2549–72.
68. Ozaki S, Minamisono T, Yamashita T, Kato T, Kushida I. Supersaturation – Nucleation Behavior of Poorly Soluble Drugs and its Impact on the Oral Absorption of Drugs in Thermodynamically High-Energy Forms. *J Pharm Sci*. 2012;101(1):214–22.
69. Poletto M, Pistor V, Zattera AJ. 2013, *Structural Characteristics and Thermal Properties of Native Cellulose*. InTech. p. 45–68.
70. Blanco A, Monte C, Campano C, Balea A, Merayo N, Negro C. 2018. *Degree of Polymerization*. In: *Handbook of Nanomaterials for Industrial Use*. USA:Elsevier p. 74–126.
71. Rajinipriya M, Nagalakshmaiah M, Robert M, Elkoun S. Importance of Agricultural and Industrial Waste in the Field of Nanocellulose and Recent Industrial Developments of Wood Based Nanocellulose: A Review. *Sustain Chem Eng*. 2018;6(3):2807–28.
72. Oishi Y, Nakaya M, Matsui E, Hotta A. Composites : Part A Structural and mechanical properties of cellulose composites made of isolated cellulose nanofibers and poly (vinyl alcohol). *Compos PART A*. 2015;73:72–9.
73. Plackett D, Siro I. Microfibrillated cellulose and new nanocomposite materials : a review. *Cellulose*. 2010;17:459–94.

74. Vartiainen J, Lucenius J, Hippi U, Serimaa R, Laine J. A Fast Method to Produce Strong NFC Films as a Platform for Barrier and Functional Materials. *Appl Mater Interfaces*. 2013;5:4640–7.
75. Boldon L, Laliberte F, Liu L. Review of the fundamental theories behind small angle X-ray scattering, molecular dynamics simulations, and relevant integrated application. *Nano Rev*. 2015;6(1):1-22.
76. Lin B, Döbeli M, Mudie S, Hawley A, Hodgson P, Kong L, et al. An in-situ small angle x ray scattering analysis of nanopore formation during thermally induced chemical dealloying of brass thin foils. *Scientific Reports*. 2018;8:1–10.
77. Welborn SS, Detsi E. Small-angle X-ray scattering of nanoporous materials. *Nanoscale Horiz*. 2020;5:12–24.
78. Garcia P, Prymak O, Grasmik V, Pappert K, Wlysses W, Otubo L, et al. An in situ SAXS investigation of the formation of silver nanoparticles and bimetallic silver gold nanoparticles in controlled wet chemical reduction synthesis. *Nanoscale Adv*. 2020;2:225–38.
79. Pauw BR, Kästner C, Thünemann AF. Nanoparticle size distribution quantification: Results of a small-angle X-ray scattering inter-laboratory comparison. *J Appl Crystallogr*. 2017;50(5):1280–88.
80. Jeng US, Su CH, Su CJ, Liao KF, Chuang WT, Lai YH, et al. A small/wide-angle X-ray scattering instrument for structural characterization of air-liquid interfaces, thin films and bulk specimens. *J Appl Crystallogr*. 2010;43(1):110–21.
81. Shtykova E V., Feigin LA, Volkov V V., Malakhova YN, Streltsov DR, Buzin AI, et al. Small-angle x-ray scattering study of polymer structure: Carbosilane

- dendrimers in hexane solution. *Crystallogr Reports*. 2016;61(5):815–25.
82. Narayanan T, Konovalov O. Synchrotron Scattering Methods for Nanomaterials and Soft Matter Research. *Materials*. 2020;13:1–52.
83. Pouget J, Levelut A, Sadoc J. André Guinier : Local order in condensed matter André Guinier : ordre local en matière condensée. *Comptes Rendus Phys*. 2019;20(7–8):725–45.
84. Garcia-Diez R, Gollwitzer C, Krumrey M, Varga Z. Size Determination of a Liposomal Drug by Small-Angle X-ray Scattering Using Continuous Contrast Variation. *Langmuir*. 2016;32(3):772–8.
85. Prosa TJ, Bauer BJ, Amis EJ, Tomalia DA, Scherrenberg R. A SAXS study of the internal structure of dendritic polymer systems. *J Polym Sci Part B Polym Phys*. 1997;35(17):2913–24.
86. Putnam CD, Hammel M, Hura GL, Tainer JA. X-ray solution scattering (SAXS) combined with crystallography and computation: Defining accurate macromolecular structures, conformations and assemblies in solution. *Quarterly Reviews of Biophysics*. 2007;40:191–285.
87. Jacques DA, Trehwella J. Small-angle scattering for structural biology - Expanding the frontier while avoiding the pitfalls. *Protein Science*. 2010;19:642–57.
88. Mertens HDT, Svergun DI. Structural characterization of proteins and complexes using small-angle X-ray solution scattering. *J Struct Biol*. 2010;172(1):128–41.
89. Svergun DI, Koch MHJ. Small-angle scattering studies of biological macromolecules in solution. *Reports Prog Phys*. 2003;66(10):1735–82.

90. Zienkiewicz-Strzałka M, Skibińska M, Pikus S. Small-angle X-ray scattering (SAXS) studies of the structure of mesoporous silicas. *Nucl Instruments Methods Phys Res Sect B Beam Interact with Mater Atoms*. 2017;411:72-77.
91. Bonneté F, Ferté N, Astier JP, Veessler S. Protein crystallization : Contribution of small angle X-ray scattering (SAXS). *Journal de Physique IV*. 2004;118(1):3-13.
92. Lo Y, Pillon MC, Stanley RE. Combining X-Ray Crystallography with Small Angle X-Ray Scattering to Model Unstructured Regions of Nsa1 from *S. Cerevisiae*. *J. Vis. Exp*. 2018;131:1–10.
93. Laggner P, Paudel A. Density fluctuations in amorphous pharmaceutical solids. Can SAXS help to predict stability? *Colloids Surfaces B Biointerfaces*. 2018;168:76–82.
94. Zhu Q, Taylor LS, Harris MT. Evaluation of the microstructure of semicrystalline solid dispersions. *Mol Pharmaceutics*. 2010;7(4):1291–300.
95. Zhu Q, Harris MT, Taylor LS. Time-resolved SAXS/WAXS study of the phase behavior and microstructural evolution of drug/PEG solid dispersions. *Mol Pharmaceutics*. 2011;8(3):932–9.
96. Gill P, Moghadam TT, Ranjbar B. Differential Scanning Calorimetry Techniques : Applications in Biology and Nanoscience. *J Biomol Tech*. 2010;21:167–93.
97. Saklatvala R, Royall PG, Craig DQM. The detection of amorphous material in a nominally crystalline drug using modulated temperature DSC — a case study. *Int J Pharm*. 1999;192:55–62.
98. Martinez LM, Videa M, Pardo SC. Long-Term Stability of New Co-Amorphous Drug Binary Systems : Study of Glass Transitions as a Function of

- Composition and Shelf Time. *Molecules*. 2016;21(12):1-10.
99. Strachan CJ, Taday PF, Newnham DA, Gordon KC, Zeitler JA, Pepper M, et al. Using Terahertz Pulsed Spectroscopy to Quantify Pharmaceutical Polymorphism and Crystallinity. *J Pharm Sci*. 2005;94(4):837–46.
100. Taraskin SN, Simdyankin SI, Elliott SR, Neilson JR, Lo T. Universal Features of Terahertz Absorption in Disordered Materials. *Phys Rev Lett*. 2006;97(5):1–4.
101. Zeitler JA, Taday PF, Pepper M, Rades T. Relaxation and Crystallization of Amorphous Carbamazepine Studied by Terahertz Pulsed Spectroscopy. *J Pharm Sci*. 2007;96(10):2703–9.
102. Bhairy SR, Habade BM, Gupta SK, Ghodke VR, Girkar YK, Kuchekar S. Pellets and pelletization as multiparticulate drug delivery systems (MPDDS): A conventional and novel approach. *Int J Institutional Pharm Life Sci*. 2015;5(4):79-126.
103. Agrawal AM, Dudhedia MS, Zimny E. Hot Melt Extrusion: Development of an Amorphous Solid Dispersion for an Insoluble Drug from Mini-scale to Clinical Scale. *AAPS PharmSciTech*. 2016;17(1):133-47.
104. Trasi NS, Boerrigter SXM, Byrn SR. Investigation of the Milling-Induced Thermal Behavior of Crystalline and Amorphous Griseofulvin. *Pharm Res*. 2010;27:1377–89.
105. Kalepu S, Nekkanti V. Insoluble drug delivery strategies: Review of recent advances and business prospects. *Acta Pharmaceutica Sinica B*. 2015;5(5):442-53.
106. Gupta S, Kesarla R, Omri A. Formulation Strategies to Improve the Bioavailability of Poorly Absorbed Drugs with Special Emphasis on Self-

- Emulsifying Systems. *ISRN Pharm.* 2013;2013:1-16.
107. Alves VM, Hwang D, Muratov E, Sokolsky-Papkov M, Varlamova E, Vinod N, et al. Cheminformatics-driven discovery of polymeric micelle formulations for poorly soluble drugs. *Sci Adv.* 2019;5:1-12.
108. Stegemann S, Leveiller F, Franchi D, de Jong H, Lindén H. When poor solubility becomes an issue: From early stage to proof of concept. *Eur J Pharm Sci.* 2007;31(5):249–61.
109. Lipinski CA. Drug-like properties and the causes of poor solubility and poor permeability. *J Pharmacol Toxicol Methods.* 2000;44(1):235–49.
110. Liu R, Li X, Lam K. Combinatorial Chemistry in Drug Discovery. *Curr Opin Chem Biol.* 2017;38:117–26.
111. He Y, Ho C. Amorphous Solid Dispersions: Utilization and Challenges in Drug Discovery and Development. *Journal of Pharmaceutical Sciences.* 2015;104(10):3237-58.
112. Li N, Taylor LS. Tailoring supersaturation from amorphous solid dispersions. *J Control Release.* 2018;279:114-25.
113. Frank KJ, Westedt U, Rosenblatt KM, Hölig P, Rosenberg J, Mägerlein M, et al. The amorphous solid dispersion of the poorly soluble ABT-102 forms nano/microparticulate structures in aqueous medium: Impact on solubility. *Int J Nanomedicine.* 2012;7:5757-68.
114. Gupta P, Chawla G, Bansal AK. Physical stability and solubility advantage from amorphous celecoxib: the role of thermodynamic quantities and molecular mobility. *Mol Pharmaceutics.* 2004;1(6):406-13.
115. Andronis V, Zografi G. Crystal nucleation and growth of indomethacin

- polymorphs from the amorphous state. *J Non Cryst Solids*. 2000;271(3):236-48.
116. Démuth B, Nagy ZK, Balogh A, Vigh T, Marosi G, Verreck G, et al. Downstream processing of polymer-based amorphous solid dispersions to generate tablet formulations. *International Journal of Pharmaceutics*. 2015;486(1-2):268-86..
117. Novakovic D, Isomäki A, Pleunis B, Fraser-Miller SJ, Peltonen L, Laaksonen T, et al. Understanding Dissolution and Crystallization with Imaging: A Surface Point of View. *Mol Pharmaceutics*. 2018;15(11):5361–73.
118. Alhalaweh A, Alzghoul A, Mahlin D, Bergström CAS. Physical stability of drugs after storage above and below the glass transition temperature: Relationship to glass-forming ability. *Int J Pharm*. 2015;495(1):312–7.
119. Murdande SB, Pikal MJ, Shanker RM, Bogner RH. Solubility advantage of amorphous pharmaceuticals: I. a thermodynamic analysis. *J Pharm Sci*. 2010;99(3):1254-64.
120. Murdande SB, Pikal MJ, Shanker RM, Bogner RH. Solubility advantage of amorphous pharmaceuticals, part 3: Is maximum solubility advantage experimentally attainable and sustainable? *J Pharm Sci*. 2011;100(10):4349-56.
121. Alonzo DE, Zhang GGZ, Zhou D, Gao Y, Taylor LS. Understanding the behavior of amorphous pharmaceutical systems during dissolution. *Pharm Res*. 2010;27(4):608-18.
122. Alonzo DE, Gao Y, Zhou D, Mo H, Zhang GGZ, Taylor LS. Dissolution and precipitation behavior of amorphous solid dispersions. *J Pharm Sci*. 2011;100(8):3316-31.

123. Edueng K, Mahlin D, Larsson P, Bergström CAS. Mechanism-based selection of stabilization strategy for amorphous formulations: Insights into crystallization pathways. *J Control Release*. 2017;256:193-202.
124. Frank DS, Matzger AJ. Probing the Interplay between Amorphous Solid Dispersion Stability and Polymer Functionality. *Mol Pharmaceutics*. 2018;15(7):2714-20.
125. Bordos E, Islam MT, Florence AJ, Halbert GW, Robertson J. Use of Terahertz-Raman Spectroscopy to Determine Solubility of the Crystalline Active Pharmaceutical Ingredient in Polymeric Matrices during Hot Melt Extrusion. *Mol Pharmaceutics*. 2019;16(10):4361-71.
126. Kalantzi L, Reppas C, Dressman JB, Amidon GL, Junginger HE, Midha KK, et al. Biowaiver monographs for immediate release solid oral dosage forms: Acetaminophen (Paracetamol). *J Pharm Sci*. 2006;95(1):4–14.
127. Etman MA, Naggat VF. Thermodynamics of paracetamol solubility in sugar-water cosolvent systems. *Int J Pharm*. 1990;58(3):177–84.
128. Bashpa P, Bijudas K, Tom AM, Archana PK, Murshida KP, Noufala Banu K, et al. Polymorphism of paracetamol: A comparative study on commercial paracetamol samples. *Int J Chem Stud*. 2014;1(6):25–9.
129. Wang I, Lee M, Seo D, Lee H, Choi Y, Kim W, et al. Polymorph Transformation in Paracetamol Monitored by In-line NIR Spectroscopy During a Cooling Crystallization Process Polymorph Transformation in Paracetamol Monitored by In-line NIR Spectroscopy During a Cooling Crystallization Process. *AAPS PharmSciTech*. 2011;12(2):1–8.
130. Ehtezazi T, Algellay M, Islam Y, Roberts M, Dempster NM, Sarker SD. The Application of 3D Printing in the Formulation of Multilayered Fast Dissolving

Oral Films The Application of 3D Printing in the Formulation of Multilayered Fast Dissolving Oral Films. *J Pharm Sci.* 2017;107(4):1076-85.

131. Nanubolu JB, Burley JC. Investigating the recrystallization behavior of amorphous paracetamol by variable temperature Raman studies and surface raman mapping. *Mol Pharmaceutics.* 2012;9(6):1544–58.
132. Babu NJ, Nangia A. Solubility advantage of amorphous drugs and pharmaceutical cocrystals. *Crystal Growth and Design.* 2011;11(7):2662-79.
133. Paus R, Ji Y, Vahle L, Sadowski G. Predicting the Solubility Advantage of Amorphous Pharmaceuticals: A Novel Thermodynamic Approach. *Mol Pharmaceutics.* 2015;12(8):2823–33.
134. Grzybowska K, Chmiel K, Knapik-Kowalczyk J, Grzybowski A, Jurkiewicz K, Paluch M. Molecular factors governing the liquid and glassy states recrystallization of celecoxib in binary mixtures with excipients of different molecular weights. *Mol Pharmaceutics.* 2017;14(4):1154–68.
135. Knapik J, Wojnarowska Z, Grzybowska K, Hawelek L, Sawicki W, Włodarski K, et al. Physical stability of the amorphous anticholesterol agent (Ezetimibe): The role of molecular mobility. *Mol Pharmaceutics.* 2014;11(11):4280–90.
136. Kothari K, Ragoonanan V, Suryanarayanan R. Influence of molecular mobility on the physical stability of amorphous pharmaceuticals in the supercooled and glassy states. *Mol Pharmaceutics.* 2014;11(9):3048–55.
137. Knapik-kowalczyk J, Chmiel K, Pacuła J, Bialek K, Tajber L, Paluch M. Enhancement of the physical stability of amorphous sildenafil in a binary mixture, with either a plasticizing or antiplasticizing compound. *Pharmaceutics.* 2020;12(5):23–8.
138. Steckel H, Markefka P, TeWierik H, Kammelar R. Effect of milling and sieving

- on functionality of dry powder inhalation products. *International Journal of Pharmaceutics*. 2006;309:51–9.
139. Lau M, Young PM, Traini D. A review of co-milling techniques for the production of high dose dry powder inhaler formulation. *Drug Development and Industrial Pharmacy*. 2017;43:1229–38.
 140. Amharar Y, Curtin V, Gallagher KH, O’Siochru E, O’Connell P, Healy AM. Mitigating unwanted amorphisation: A screening method for the selection of suitable excipients. *Eur J Pharm Sci*. 2016;81:181–8.
 141. Priemel PA, Grohganz H, Rades T. Unintended and in situ amorphisation of pharmaceuticals. *Advanced Drug Delivery Reviews*. 2016;100:126–32.
 142. Stofella NCF, Veiga A, Oliveira LJ, Montin EF, Andreazza IF, Filho MASC, et al. Solid-State characterization of different crystalline forms of sitagliptin. *Materials*. 2019;12(15):1-16.
 143. Vippagunta SR, Brittain HG, Grant DJW. Crystalline solids. *Adv Drug Deliv Rev*. 2001;48(1):3–26.
 144. Rattanawongwiboon T, Soontaranon S, Hemvichian K, Lertsarawut P, Laksee S, Picha R. Study on particle size and size distribution of gold nanoparticles by TEM and SAXS. *Radiat Phys Chem*. 2022;191:1-5.
 145. Korasick DA, Tanner JJ. Determination of protein oligomeric structure from small-angle X-ray scattering. *Protein Science*. 2018;27(4):814–24.
 146. Skou S, Gillilan RE, Ando N. Synchrotron-based small-angle X-ray scattering of proteins in solution. *Nat Protoc*. 2014;9(7):1727–39.
 147. Portale G, Cavallo D, Alfonso C, Hermida- D, Drongelen M Van, Balzano L, et al. research papers Polymer crystallization studies under processing- relevant

- conditions at the SAXS / WAXS DUBBLE beamline at the ESRF 1 research papers. *J. Appl. Cryst.* 2013;46:1681–9.
148. Goderis B, Reynaers H, Koch MHJ, Mathot VBF. Use of SAXS and Linear Correlation Functions for the Determination of the Crystallinity and Morphology of Semi- Crystalline Polymers . Application to Linear Polyethylene. *Journal of Polymer Science Part B.* 1999;37(14):1715–38.
149. Thakral S, Kim K. Small-angle scattering for characterization of pharmaceutical materials. *Trends Anal Chem.* 2021;134:1-9.
150. Florence AJ, Shankland N, Shankland K, David WIF, Pidcock E, Xu X, et al. Solving molecular crystal structures from laboratory X-ray powder diffraction data with DASH: The state of the art and challenges. *J Appl Crystallogr.* 2005;38(2):249–59.
151. Hulme AT, Fernandas P, Florence A, Johnston A, Shankland K. Powder study of 3-azabicyclo[3.3.1]nonane-2,4-dione form 2. *Acta Crystallogr Sect E Struct Reports Online.* 2006;62(7):3046-48.
152. Arlin JB, Bhardwaj RM, Johnston A, Miller GJ, Bardin J, Macdougall F, et al. Structure and stability of two polymorphs of creatine and its monohydrate. *CrystEngComm.* 2014;16(35):8197–204.
153. Perl J, Shin J, Schümann J, Faddegon B, Paganetti H. TOPAS: An innovative proton Monte Carlo platform for research and clinical applications. *Med Phys.* 2012;39(11):6818–37.
154. Corsepius NC, DeVore TC, Reisner BA, Warnaar DL. Using variable temperature powder X-ray diffraction to determine the thermal expansion coefficient of solid MgO. *J Chem Educ.* 2007;84(5):818–21.
155. van der Lee A, Dumitrescu DG. Thermal expansion properties of organic

- crystals: a CSD study. *Chem Sci.* 2021;12(24):8537–47.
156. Kong Y, Hay JN. The measurement of the crystallinity of polymers by DSC. *Polymer.* 2002;43(14):3873–8.
157. Chun N, Lee M, Song G, Chang K, Kim C, Choi GJ. Combined anti-solvent and cooling method of manufacturing indomethacin – saccharin (IMC – SAC) co-crystal powders. *J Cryst Growth.* 2014;408:112–18.
158. Pazesh S, Gråsjö J, Berggren J, Alderborn G. Comminution-amorphisation relationships during ball milling of lactose at different milling conditions. *Int J Pharm.* 2017;528(1-2):215-27.
159. Ashrafizadeh H, Ashrafizaadeh M. Influence of processing parameters on grinding mechanism in planetary mill by employing discrete element method. *Adv Powder Technol.* 2012;23(6):708–16.
160. Yazdani A, Ho WH. A method to quantify crystallinity in amorphous metal alloys : A differential scanning calorimetry study. *PLOS ONE.* 2020.15(6):1–31.
161. Doumeng M, Makhlouf L, Berthet F, Marsan O, Delb K, Denape J, et al. A comparative study of the crystallinity of polyetheretherketone by using density, DSC, XRD, and Raman spectroscopy techniques. 2021;93:1-10.
162. Smith G, Hussain A, Irfan N, Ermolina I. Quantification of residual crystallinity in ball milled commercially sourced lactose monohydrate by thermo-analytical techniques and terahertz spectroscopy. *Eur J Pharm Biopharm.* 2015;92:180–91.
163. Yuan L, H JA, S RW, S RJ. Thermal analysis of amorphous lactose and α - lactose monohydrate. *Dairy Science & Technology.* 2009;89:43–67.

164. Jo O. Amorphization of a crystalline active pharmaceutical ingredient and thermoanalytical measurements on this glassy form. *Journal of Thermal Analysis and Calorimetry*. 2010;102:243–47.
165. Liu X, Feng X, Williams RO, Zhang F. Characterization of amorphous solid dispersions. *J Pharm Investig*. 2018;48(1):19–41.
166. Kaushal AM, Chakraborti AK, Bansal AK. FTIR studies on differential intermolecular association in crystalline and amorphous states of structurally related non-steroidal anti-inflammatory drugs. *Mol Pharmaceutics*. 2008;5(6):937–45.
167. Pinto JT, Radivojev S, Zellnitz S, Roblegg E, Paudel A. How does secondary processing affect the physicochemical properties of inhalable salbutamol sulphate particles? A temporal investigation. *Int J Pharm*. 2017;528(1–2):416–28.
168. Taylor P, Fundamentals XI, Leverkusen BAG, Germany W. Part B : Physics Phase separation in urethane elastomers as judged by low-angle Phase Separation in Urethane Elastomers as Judged by low- Angle X-Ray Scattering . I . Fundamentals. (June 2014):37–41.
169. Liu J, Pancera S, Boyko V, Shukla A, Narayanan T, Huber K. Evaluation of the Particle Growth of Amorphous Calcium Carbonate in Water by Means of the Porod Invariant from SAXS. *Langmuir*. 2010;26(10):17405–12.
170. W R. Small-Angle Scattering of Two-Phase Systems: Determination and Significance of Systematic Deviations from Porod's Law. *J Appl Crystallogr*. 1971;4:70–73.
171. Tsukimura K, Miyoshi Y, Takagi T, Suzuki M. Amorphous nanoparticles in clays, soils and marine sediments analyzed with a small angle X - ray

- scattering (SAXS) method. *Sci Rep.* 2021;11:1–11.
172. Paudel D, Atta-fynn R, Drabold DA, Elliott SR, Biswas P. Small-angle X-ray scattering in amorphous silicon: A computational study. *Physical Review.* 2018;97:1–13.
173. David L. Density Fluctuations in amorphous systems : SAXS and PALS results. *Journal of Non-Crystalline Solids.* 1998;237:383–7.
174. Bengtsen T, Holm VL, Kjølbye LR, Midtgaard SR, Johansen NT, Bottaro S, et al. Structure and dynamics of a lipid nanodisc by integrating NMR, SAXS and SANS experiments with molecular dynamics simulations. *eLife.* 2020;9:1–22.
175. Schwamberger A, De Roo B, Jacob D, Dillemans L, Bruegemann L, Seo JW, et al. Combining SAXS and DLS for simultaneous measurements and time-resolved monitoring of nanoparticle synthesis. *Nucl Instruments Methods Phys Res Sect B Beam Interact with Mater Atoms.* 2015;343:116–22.
176. Bucciarelli S, Midtgaard SR, Pedersen MN, Skou S, Arleth L, Vestergaard B. Size-exclusion chromatography small-angle X-ray scattering of water soluble proteins on a laboratory instrument. *J Appl Crystallogr.* 2018;51(6):1623–32.
177. Jensen GV, Pedersen JN, Otzen DE, Pedersen JS. Multi-Step Unfolding and Rearrangement of α -Lactalbumin by SDS Revealed by Stopped-Flow SAXS. *Front Mol Biosci.* 2020;7:1–12.
178. Billinge SJL. The rise of the X-ray atomic pair distribution function method: A series of fortunate events. *Philos Trans R Soc A.* 2019;377:1-17.
179. Lin D, Liu Z, Shen R, Chen S, Yang X. Bacterial cellulose in food industry: Current research and future prospects. *Int J Biol Macromol.* 2020;158:1007-19.

180. Dias OAT, Konar S, Leão AL, Yang W, Tjong J, Sain M. Current State of Applications of Nanocellulose in Flexible Energy and Electronic Devices. *Frontiers in Chemistry*. 2020;8:1-15.
181. Li T, Chen C, Brozena AH, Zhu JY, Xu L, Driemeier C, et al. Developing fibrillated cellulose as a sustainable technological material. *Nature*. 2021;590(7844):47–56.
182. Shaghaleh H, Xu X, Wang S. Current progress in production of biopolymeric materials based on cellulose, cellulose nanofibers, and cellulose derivatives. *RSC Adv*. 2018;8(2):825–42.
183. Wang X, Li H, Cao Y, Tang Q. Cellulose extraction from wood chip in an ionic liquid 1-allyl-3-methylimidazolium chloride (AmimCl). *Bioresour Technol*. 2011;102(17):7959-65.
184. Kamel R, El-Wakil NA, Dufresne A, Elkasabgy NA. Nanocellulose: From an agricultural waste to a valuable pharmaceutical ingredient. *Int J Biol Macromol*. 2020;163:1579-90.
185. Cheng L, Hu X, Gu Z, Hong Y, Li Z, Li C. Characterization of physicochemical properties of cellulose from potato pulp and their effects on enzymatic hydrolysis by cellulase. *Int J Biol Macromol*. 2019;131:564-571.
186. Khawas P, Deka SC. Isolation and characterization of cellulose nanofibers from culinary banana peel using high-intensity ultrasonication combined with chemical treatment. *Carbohydr Polym*. 2016;137:608-16.
187. Kalita E, Nath BK, Deb P, Agan F, Islam MR, Saikia K. High quality fluorescent cellulose nanofibers from endemic rice husk: Isolation and characterization. *Carbohydr Polym*. 2015;122:308-13.
188. Haigler CH, Betancur L, Stiff MR, Tuttle JR. Cotton fiber: A powerful single-

- cell model for cell wall and cellulose research. *Frontiers in Plant Science*. 2012;3:1-7.
189. Kumar V, Bollstrom R, Yang A, Chen Q, Chen G, Salminen P, et al. Comparison of nano- and microfibrillated cellulose films. *Cellulose*. 2014;21:3443–56.
190. Mekonnen T, Dubé MA. Renewable polymers: Processing and chemical modifications. *Processes*. 2019;7(7):3–5.
191. Jakubek ZJ, Chen M, Couillard M, Leng T, Liu L, Zou S, et al. Characterization challenges for a cellulose nanocrystal reference material: dispersion and particle size distributions. *J Nanoparticle Res*. 2018;20(4):1-11.
192. Li J, Zhang S, Gao B, Yang A, Wang Z, Xia Y, et al. Characteristics and deoxy-liquefaction of cellulose extracted from cotton stalk. *Fuel*. 2016;166:196–202.
193. Dufresne A. Nanocellulose: A new ageless bionanomaterial. *Mater Today*. 2013;16(6):220–7.
194. Iwamoto S, Kai W, Isogai A, Iwata T. Elastic modulus of single cellulose microfibrils from tunicate measured by atomic force microscopy. *Biomacromolecules*. 2009;10(9):2571-76.
195. Lahiji RR, Xu X, Reifenberger R, Raman A, Rudie A, Moon RJ. Atomic force microscopy characterization of cellulose nanocrystals. *Langmuir*. 2010;26(6):4480-88.
196. Lundahl MJ, Klar V, Wang L, Ago M, Rojas OJ. Spinning of cellulose nanofibrils into filaments: A review. *Industrial and Engineering Chemistry Research*. 2017;56(1):8-19.

197. Taheri H, Hietala M, Oksman K. One-step twin-screw extrusion process of cellulose fibers and hydroxyethyl cellulose to produce fibrillated cellulose biocomposite. *Cellulose*. 2020;27(14):8105-19.
198. Segal L, Creely JJ, Martin AE, Conrad CM. An Empirical Method for Estimating the Degree of Crystallinity of Native Cellulose Using the X-Ray Diffractometer. *Text Res J*. 1959;29(10):786-94.
199. Iwamoto S, Isogai A, Iwata T. Structure and mechanical properties of wet-spun fibers made from natural cellulose nanofibers. *Biomacromolecules*. 2011;12(3):831-36.
200. Tanaka T, Fujita M, Takeuchi A, Suzuki Y, Uesugi K, Ito K, et al. Formation of highly ordered structure in poly[(R)-3-hydroxybutyrate-co-(R)-3-hydroxyvalerate] high-strength fibers. *Macromolecules*. 2006;39(8):2940-46.
201. Kafy A, Kim HC, Zhai L, Kim JW, Hai L Van, Kang TJ, et al. Cellulose long fibers fabricated from cellulose nanofibers and its strong and tough characteristics. *Sci Rep*. 2017;7:1-8.
202. Helmiyata, Aprilliza M. Characterization and properties of sodium alginate from brown algae used as an ecofriendly superabsorbent. *J Phys Conf Ser*. 2017;188(1):1-5.
203. Park S, Baker JO, Himmel ME, Parilla PA, Johnson DK. Cellulose crystallinity index: Measurement techniques and their impact on interpreting cellulase performance. *Biotechnol Biofuels*. 2010;3:1-10.
204. Bhujbal S V., Mitra B, Jain U, Gong Y, Agrawal A, Karki S, et al. Pharmaceutical amorphous solid dispersion: A review of manufacturing strategies. *Acta Pharm Sin B*. 2021;11(8):2505–36.
205. Kallakunta VR, Sarabu S, Bandari S, Batra A, Bi V, Durig T, et al. Stable

- amorphous solid dispersions of fenofibrate using hot melt extrusion technology: Effect of formulation and process parameters for a low glass transition temperature drug. *J Drug Deliv Sci Technol*. 2020;58(3):139–48.
206. Liu P, De Wulf O, Laru J, Heikkilä T, Van Veen B, Kiesvaara J, et al. Dissolution studies of poorly soluble drug nanosuspensions in non-sink conditions. *AAPS PharmSciTech*. 2013;14(2):748–56.
207. Akpalu Y, Kielhorn L, Hsiao BS, Stein RS, Russell TP, Egmond J Van, et al. Structure Development during Crystallization of Homogeneous Copolymers of Ethene and 1-Octene : Time-Resolved Synchrotron X-ray and SALS Measurements. *Macromolecules*. 1999;32:765–70.
208. Mahendrasingam A, Blundell DJ, Wright AK, Urban V, Narayanan T, Fuller W. Time resolved WAXS/SAXS observations of crystallisation in oriented melts of ultra high molecular weight polyethylene. *Polymer*. 2004;45(16):5641–52.
209. Alhijaj M, Yassin S, Reading M, Zeitler JA, Belton P, Qi S. Characterization of Heterogeneity and Spatial Distribution of Phases in Complex Solid Dispersions by Thermal Analysis by Structural Characterization and X-ray Micro Computed Tomography. *Pharm Res*. 2017;34(5):971-89.
210. Shi Q, Chen H, Wang Y, Wang R, Xu J, Zhang C. Amorphous Solid Dispersions : Role of the Polymer and Its Importance in Physical Stability and In Vitro Performance. *Pharmaceutics*. 2022;14(8):1-25.
211. Anker AS, Christiansen TL, Weber M, Schmiele M, Brok E, Kjær ETS, et al. Cluster Compounds Very Important Paper Structural Changes during the Growth of Atomically Precise Metal Oxido Nanoclusters from Combined Pair Distribution Function and Small-Angle X-ray Scattering Analysis. *Angew*

Chemie - Int Ed. 2021;60:20407–16.

212. Schneider K, Schone A, Jun TS, Korsunsky AM. Investigation of changes in crystalline and amorphous structure during deformation of nano-reinforced semi-crystalline polymers by space-resolved synchrotron saxs and waxes. *Procedia Eng.* 2009;1(1):159–62.
213. Tencé-Girault S, Lebreton S, Bunau O, Dang P, Bargain F. Simultaneous SAXS-WAXS experiments on semi-crystalline polymers: Example of PA11 and its brill transition. *Crystals.* 2019;9(5):1-17.
214. Benmore CJ, Benmore SR, Edwards AD, Shrader CD, Bhat MH, Cherry BR, et al. A High Energy X-ray Diffraction Study of Amorphous Indomethacin. *J Pharm Sci.* 2022;111(3):818–24.
215. Bezzon VDN, Ferreira FF, Smith P, Benmore CJ, Byrn SR, de Araujo GLB. Amorphous dispersions of flubendazole in hydroxypropyl methylcellulose: Formulation stability assisted by pair distribution function analysis. *Int J Pharm.* 2021;600:1-8.
216. Fischer HE, Barnes AC, Salmon PS. Neutron and x-ray diffraction studies of liquids and glasses. *Reports Prog Phys.* 2006;69(1):233–99.
217. Benmore CJ. A Review of High-Energy X-Ray Diffraction from Glasses and Liquids. *Mater Sci.* 2012;2012:1–19.
218. Bolze J, Gateshki M. Highly versatile laboratory X-ray scattering instrument enabling (nano-) material structure analysis on multiple length scales by covering a scattering vector range of almost five decades Highly versatile laboratory X-ray scattering instrument enabling. *Rev Sci Instrum.* 2019;90(12):1-14.
219. Raghav N, Sharma MR, Kennedy JF. Nanocellulose : A mini-review on types

- and use in drug delivery systems. *Carbohydr Polym Technol Appl*. 2021;2:1-10.
220. Chen T, He X, Jiang T, Liu W, Li Y, Liu P, et al. Synthesis and drug delivery properties of Ibuprofen-Cellulose nanofibril system. *Int J Biol Macromol*. 2021;182:931–7.
221. Yan G, Feng Y, Wang H, Sun Y, Tang X. Cellulose Fibrils Extracted from Bamboo Chips as a Reinforcing Material for Prolonged Drug Release. *Chem Sel*. 2020;5:9957–65.
222. Cheng L, Hu X, Gu Z, Hong Y, Li Z, Li C. Characterization of physicochemical properties of cellulose from potato pulp and their effects on enzymatic hydrolysis by cellulase. *Int J Biol Macromol*. 2019;131:564–71.
223. Ahvenainen P, Kontro I, Svedström K. Comparison of sample crystallinity determination methods by X-ray diffraction for challenging cellulose I materials. *Cellulose*. 2016;23(2):1073–86.